

Quarterly Technical Report

Solid State Research

1989:4

---

**Lincoln Laboratory**

MASSACHUSETTS INSTITUTE OF TECHNOLOGY

*LEXINGTON, MASSACHUSETTS*



---

Prepared under Air Force Contract F19628-90-C-0002.

Approved for public release; distribution is unlimited.

ADA225803

This report is based on studies performed at Lincoln Laboratory, a center for research operated by Massachusetts Institute of Technology, with the support of the Department of the Air Force under Contract F19628-90-C-0002.

This report may be reproduced to satisfy needs of U.S. Government agencies.

The ESD Public Affairs Office has reviewed this report, and it is releasable to the National Technical Information Service, where it will be available to the general public, including foreign nationals.

This technical report has been reviewed and is approved for publication.

FOR THE COMMANDER

*Hugh L. Southall*

Hugh L. Southall, Lt. Col., USAF  
Chief, ESD Lincoln Laboratory Project Office

Non-Lincoln Recipients

**PLEASE DO NOT RETURN**

Permission is given to destroy this document  
when it is no longer needed.



**MASSACHUSETTS INSTITUTE OF TECHNOLOGY  
LINCOLN LABORATORY**

**SOLID STATE RESEARCH**

**QUARTERLY TECHNICAL REPORT**

**1 AUGUST — 31 OCTOBER 1989**

**ISSUED 19 JUNE 1990**

**Approved for public release; distribution is unlimited.**

**LEXINGTON**

**MASSACHUSETTS**

## **ABSTRACT**

This report covers in detail the research work of the Solid State Division at Lincoln Laboratory for the period 1 August through 31 October 1989. The topics covered are Electrooptical Devices, Quantum Electronics, Materials Research, Submicrometer Technology, Microelectronics, and Analog Device Technology. Funding is provided primarily by the Air Force, with additional support provided by the Army, DARPA, Navy, SDIO, NASA, and DOE.



## TABLE OF CONTENTS

Abstract	iii
List of Illustrations	vii
List of Tables	xii
Introduction	xiii
Reports on Solid State Research	xvii
Organization	xxv
<b>1. ELECTROOPTICAL DEVICES</b>	<b>1</b>
1.1 Effects of P <sup>+</sup> Implants and Annealing on Zn <sup>+</sup> -Implanted InP:Fe	1
1.2 GaInAsP/InP Buried-Heterostructure Surface-Emitting Diode Laser with Monolithic Integrated Bifocal Microlens	6
<b>2. QUANTUM ELECTRONICS</b>	<b>13</b>
2.1 Starting Dynamics of a Passively Mode-Locked Ti:Al <sub>2</sub> O <sub>3</sub> Laser	13
2.2 Frequency-Chirped Nd:YAG Laser	16
2.3 Sum-Frequency Generation of Sodium-Resonance Radiation	18
2.4 Pump Source Requirements for End-Pumped Lasers	21
2.5 Limits Imposed by Spatial Hole Burning on the Single-Mode Operation of Microchip Lasers	23
2.6 Thermal Waveguiding in Microchip Lasers	26
2.7 Mirror Misalignment Tolerances in Microchip Lasers	29
<b>3. MATERIALS RESEARCH</b>	<b>33</b>
3.1 PtSi Schottky-Barrier Focal Plane Arrays for Multispectral Imaging in Ultraviolet, Visible and Infrared Spectral Bands	33
3.2 Efficient GaInAsSb/AlGaAsSb Diode Lasers Emitting at 2.29 $\mu\text{m}$	38
3.3 Room-Temperature Continuous Operation of GaAs/AlGaAs Lasers Grown on Si by OMVPE	42
3.4 Chemical Vapor Deposition of Boron Nitride for Coating Fused Silica Crucibles	46
<b>4. SUBMICROMETER TECHNOLOGY</b>	<b>51</b>
4.1 New Photomask Technology for 193-nm Lithography	51
4.2 Silylation Processes for 193-nm Lithography	55

## TABLE OF CONTENTS (Continued)

5.	MICROELECTRONICS	61
5.1	Improved Process for Thinned, Back-Illuminated CCD Imaging Devices	61
5.2	Proton Irradiation of CCD Imaging Devices	67
5.3	CCD Neural Net Processor	68
6.	ANALOG DEVICE TECHNOLOGY	73
6.1	Microwave Dielectric Properties of Evaporated Silicon Monoxide at 4.2 K	73
6.2	Analysis of the Effect of Counterdoping in the Gaps of a Single-Gate-Level CCD Process	74

## LIST OF ILLUSTRATIONS

Figure No.		Page
1-1	Hole concentration vs depth for 200-keV, $5 \times 10^{13}\text{-cm}^{-2}$ Zn <sup>+</sup> implanted into InP:Fe at 25°C with and without 100-keV, $5 \times 10^{13}\text{-cm}^{-2}$ P <sup>+</sup> implanted at 25°C and for two annealing treatments.	2
1-2	Hole concentration vs depth for 200-keV, $5 \times 10^{14}\text{-cm}^{-2}$ Zn <sup>+</sup> implanted into InP:Fe at 25°C with and without 100-keV, $5 \times 10^{14}\text{-cm}^{-2}$ P <sup>+</sup> implanted at 25°C and for two annealing treatments.	5
1-3	Longitudinal cross-sectional view of diode laser with monolithic integrated bifocal microlens. The microlens has two portions with different curvatures and coatings to separately optimize the optical feedback and beam collimation. The GaInAsP/InP gain region is a mass-transported buried heterostructure.	7
1-4	(a) Optical micrographs of two bifocal microlenses. (b), (c) Images formed by collimating lens and spherical mirror portions, respectively.	8
1-5	Stylus surface profiling of a bifocal microlens (solid trace) and a calculated exact spherical profile (dotted curve).	9
1-6	Micrographs of an integrated lens-laser structure (before metallization) obtained by (a) reflected visible light and (b) transmitted infrared. The underlying microlenses and the concentrated spots of light they produce are clearly seen in the infrared micrograph.	10
1-7	(a) Light output vs current characteristic and (b) far-field pattern of a monolithic lens-laser.	11
2-1	Schematic of the passively mode-locked Ti:Al <sub>2</sub> O <sub>3</sub> laser. The main laser cavity is astigmatically compensated and contains only the gain medium and a birefringent tuning plate. The coupled cavity begins at output coupler $M_o$ and terminates at the mirror butt-coupled to the optical fiber. To study the self-starting dynamics, the coupled cavity is opened with a chopper while the output power and second-harmonic signal are monitored. BS, beam splitter; GRIN, graded index; SHG, second-harmonic generator.	14
2-2	Signals from Ti:Al <sub>2</sub> O <sub>3</sub> laser showing start-up of passive mode locking. Output power monitored with (a) a slow photodiode and (b) a fast photodiode, and (c) the second-harmonic signal monitored with a slow photodiode.	14



## LIST OF ILLUSTRATIONS (Continued)

Figure No.		Page
2-3	Second-harmonic signal and pulse duration as a function of the change in length of the external cavity. Lack of a second-harmonic signal indicates continuous operation; generation of a second-harmonic signal while scanning in either the forward or backward direction indicates self-starting mode-locked operation; bistability indicates sustained mode-locked operation.	15
2-4	Schematic of the frequency-chirped Nd:YAG laser. The Nd:YAG laser consists of a Nd:YAG rod with a high-reflectivity mirror coated on one end, a Brewster-cut LiNbO <sub>3</sub> crystal acting as an electrooptic phase modulator, and an end mirror ( $R = 7.5$ cm) with 10-percent transmission. The voltage applied across the LiNbO <sub>3</sub> is produced by a function generator and a 25-W RF amplifier. The laser output is heterodyned against the single-frequency output of a microchip laser.	17
2-5	(a) Output of the function generator. This RF signal is amplified by 50 dB and applied to the electrooptic phase modulator. The laser output frequency should be linearly related to the applied voltage. (b) Heterodyne signal between the frequency-chirped laser and the stable laser. (c) Computer-calculated heterodyne signal for an initial frequency difference of 4 MHz, frequency chirp of 140 MHz, and chirp time of 120 ns. The calculated and measured waveforms are in good agreement; the discrepancies arise from pickup.	17
2-6	Nd:YAG laser system for long-pulse-length, sum-frequency generation of sodium-resonance radiation.	20
2-7	Schematic of the fundamental mode with radius $\omega_0$ and the pump beam with waist $\omega_{p0}$ and far-field diffraction angle $\theta_p$ in the gain medium.	21
2-8	Schematic of a pump source consisting of seven individual sources, each of which is collimated by a lens.	22
2-9	Inversion ratio $\zeta(1,2)$ as a function of cavity length $\ell$ for a longitudinally pumped laser cavity completely filled with Nd:YAG (see inset), operating at $1.32 \mu\text{m}$ .	25
2-10	Waist size $\omega_0$ of the TEM <sub>00</sub> mode of a microchip laser as a function of incident pump power $P$ . The circles represent experimental data. The solid curve corresponds to $\omega_0^2 = 5986P^{1/2} \mu\text{m}^2$ , with $P$ in watts.	27

## LIST OF ILLUSTRATIONS (Continued)

Figure No.		Page
2-11	Waist size $\omega_0$ of the TEM <sub>00</sub> mode of a microchip laser as a function of the radius of the pump spot, $r_{\text{inc}}$ . The circles represent experimental data. The solid curve corresponds to $\omega_0^2 = 241 (75^2 + r_{\text{inc}}^2)^{1/2} \mu\text{m}^2$ , with $r_{\text{inc}}$ in micrometers.	27
2-12	Far-field patterns of the microchip laser as a thermal gradient is applied across the microchip wafer. The pump power was 300 mW focused to a 17- $\mu\text{m}$ radius at the pump surface of the microchip laser. The magnitude of the thermally induced optical wedge is (a) $\psi = 3.3 \times 10^{-5}$ rad, (b) $\psi = 3.6 \times 10^{-5}$ rad, (c) $\psi = 4.2 \times 10^{-5}$ rad, and (d) $\psi = 9.2 \times 10^{-5}$ rad. Large white areas correspond to saturation of the CID camera.	30
3-1	Schematic diagram showing a single pixel of a $160 \times 244$ -element PtSi focal plane array operated in the front-illumination mode.	34
3-2	Quantum efficiency as a function of wavelength for a front-illuminated PtSi Schottky-barrier detector.	35
3-3	Fowler plot for the data of Figure 3-2 between 3.5 and 6.2 $\mu\text{m}$ .	36
3-4	(a) Infrared and (b) visible images of a coffee mug obtained with a front-illuminated $160 \times 244$ -element PtSi Schottky-barrier focal plane array.	37
3-5	Energy gap vs lattice constant for GaInAsSb and AlGaAsSb quaternary alloys.	38
3-6	Schematic cross section of broad-stripe GaInAsSb/AlGaAsSb double-heterostructure diode laser.	40
3-7	Light output vs current characteristic of GaInAsSb/AlGaAsSb diode laser for pulsed operation at room temperature.	41
3-8	Emission spectrum of GaInAsSb/AlGaAsSb diode laser for pulsed operation at room temperature.	42
3-9	Differential quantum efficiency vs cavity length for broad-stripe AlGaAs/GaAs-on-Si diode lasers with thermally cycled GaAs defect-filtering layer.	44
3-10	Light output vs current for room-temperature CW operation of ridge-waveguide AlGaAs/GaAs-on-Si diode laser with thermally cycled GaAs defect-filtering layer.	45

## LIST OF ILLUSTRATIONS (Continued)

Figure No.		Page
4-1	Photomicrograph of features from 0.7 to 1.4 $\mu\text{m}$ of a pattern fabricated with electron-beam lithography in Al on fused silica, and used in 193-nm contact printing. Areas from left to right are freestanding lines, via holes in positive polarity, via holes in negative polarity, a corner turn, and gratings with equal lines and spaces.	51
4-2	Process sequence in fabrication of photomask for 193-nm contact printing. Stages shown are (a) sample preparation, (b) resist spinning, (c) exposure and development, (d) evaporation and lift-off, and (e) aluminum etching.	52
4-3	Process sequence in fabrication of photomask for 193-nm projection printing. Stages shown are (a) sample preparation, (b) resist spinning, (c) exposure and development, (d) aluminum etching, and (e) resist removal.	53
4-4	Schematic of negative- and positive-tone silylation processes, showing (a) exposure, (b) silylation, and (c) etching steps.	55
4-5	Interferometric traces from dissolution of a 1- $\mu\text{m}$ -thick PR1024 resist film in AZ 327 MIF developer. Upper trace is from an unexposed film, while lower trace was exposed to 200 $\text{mJ}/\text{cm}^2$ of 193-nm radiation. The effect of the laser-induced crosslinking is noted as inhibited dissolution for $\sim 250$ s.	57
4-6	Exposure curves showing etch rate in an $\text{O}_2$ RIE plasma as a function of 193-nm exposure dose for SAL 601, FSC, and PR1024 resists. Films were silylated at $100^\circ\text{C}$ for 1 min in 10-Torr DMSDMA, and etched in an $\text{O}_2$ RIE plasma with a bias voltage of $-200$ V for 20 min.	58
4-7	Scanning electron micrograph of 0.4- $\mu\text{m}$ lines and spaces in FSC resist exposed at 60 $\text{mJ}/\text{cm}^2$ of 193-nm radiation. Films were silylated at $100^\circ\text{C}$ for 1 min in 10-Torr DMSDMA, and etched in an $\text{O}_2$ RIE plasma with a bias voltage of $-200$ V for 40 min.	59
5-1	Back-illuminated CCD imager fabrication sequence: (a) wafer mounting to glass substrate, (b) selective etching to thin Si wafer down to epilayer, (c) back-surface processing, and (d) etching Si and $\text{SiO}_2$ to expose bonding pads.	62
5-2	Dependence of sheet resistivity on laser energy density for two different levels of $\text{BF}_2$ implantation.	63
5-3	Doping profiles of the shallow accumulation layer formed by ion-implanted laser-annealed process.	64



## LIST OF ILLUSTRATIONS (Continued)

Figure No.		Page
5-4	Activation of implanted boron and depth of peak carrier concentration vs number of irradiating laser pulses.	65
5-5	Quantum efficiency of front-illuminated and back-illuminated CCDs with and without back passivation.	66
5-6	Block diagram of CCD neural net device.	69
5-7	Architecture of digital connection-weight memory.	70
5-8	Photomicrograph of the neural net device.	71
5-9	Input and output signals of a tapped delay line. The output is nondestructively sensed at tap 25 of a 48-stage delay line.	72
6-1	(a) Cross-sectional view of microstrip resonator with deposited silicon monoxide dielectric. (b) Top view of the microstrip resonator showing patterned niobium microstrip transmission line.	74
6-2	Single-poly-Si CCD structure; only two electrode phases are shown.	76
6-3	Concentration of the BC donor implant.	76
6-4	Timing diagram for three-phase CCD structure. High levels are attractive to electrons (more positive gate voltage).	77
6-5	Calculated potential minimum (taken across depth) of empty wells as a function of lateral position for different gate voltages.	78
6-6	Calculated potential of the BC well as a function of depth in a cross section under an electrode with $\Phi_2 = 12$ V for different charge packets $Q_n$ .	79
6-7	Spatial mobile charge distribution as a function of depth under a gate corresponding to the curves in Figure 6-6.	80
6-8	Calculated potential as a function of depth in a cross section in the gap region for different charge packets.	81
6-9	Spatial mobile charge distribution as a function of depth corresponding to the curves in Figure 6-8.	82
6-10	Channel doping profile to reduce the potential trough: <i>n</i> -type BC and <i>p</i> -type shallow counterdoping.	83

## LIST OF ILLUSTRATIONS (Continued)

Figure No.		Page
6-11	Calculated potential minimum (taken across depth) of empty wells as a function of lateral position for different gate voltages when the gap region has been implanted.	84
6-12	Calculated potential as a function of depth in a cross section in the counterdoped gap region for different charge packets.	85
6-13	Spatial charge distribution corresponding to the curves in Figure 6-12.	86

## LIST OF TABLES

Table No.		Page
1-1	Summary of Peak Hole Concentrations and Profile Shapes for All Implant and Anneal Conditions	4
3-1	Effect of Defect-Filtering Layers on Characteristics of Broad-Stripe AlGaAs/GaAs-on-Si Diode Lasers	44

# INTRODUCTION

## 1. ELECTROOPTICAL DEVICES

Effects of  $P^+$  implants, implantation temperature, and type of post-implant anneal on the hole-concentration depth profiles of semi-insulating InP wafers implanted with  $5 \times 10^{13}$ - and  $5 \times 10^{14}$ -cm<sup>-2</sup>  $Zn^+$  ions have been investigated. The  $P^+$  co-implant combined with capless rapid thermal annealing greatly suppressed Zn dopant indiffusion at low doses, and at high doses this combination produced  $>2\times$  higher peak hole concentrations.

A first attempt has been made to monolithically integrate a microlens with a diode laser. The integrated device showed a narrow beam divergence of  $1.25^\circ$  and is potentially advantageous for fiber coupling, optical interconnects, and laser-array applications.

## 2. QUANTUM ELECTRONICS

Self-starting dynamics of a passively mode-locked  $Ti:Al_2O_3$  laser with a nonlinear coupled cavity have been studied. Mode locking develops from mode beating, with pulse formation occurring in  $\sim 230$   $\mu s$ .

A linear frequency chirp of 1.2 MHz/ns over a range of 140 MHz has been generated from a single-frequency Nd:YAG laser with a retrace time of 20 ns. Preliminary measurements have been made to assess the applicability of this laser system to range-Doppler coherent radar.

The development of a solid state source of long-pulse-length, sodium-resonance radiation has been completed. This radiation is generated by sum-frequency mixing the output of a 1.064- $\mu m$  Nd:YAG laser with the output of a 1.319- $\mu m$  Nd:YAG laser.

Relationships between the properties of the pump beam and the gain medium in end-pumped lasers have been derived. A novel scheme for power scaling of end-pumped lasers using multiple sources is described in terms of these relationships.

A simple formula has been derived which gives the ratio of the maximum single-longitudinal-mode inversion density to the threshold inversion density for a microchip laser. The parameters are easily measured (and often published) spectroscopic properties of the gain medium.

It has been determined that CW microchip lasers operate in a thermally waveguided mode. In Nd:YAG, the diameter of the oscillating mode is typically much larger than the pump diameter, resulting in a low-divergence beam that is insensitive to the quality of the pump beam.

A 700- $\mu m$ -long Nd:YAG microchip laser operating at 1.064  $\mu m$  has been shown to have an angular tolerance in mirror misalignment of approximately  $\psi_{\max} = 10^{-4} P_{\min}$  rad, where  $P_{\min}$  is the minimum pump power (in watts) for which the microchip laser should oscillate in a circularly symmetric  $TEM_{00}$  mode.



### 3. MATERIALS RESEARCH

PtSi Schottky-barrier detectors, which are conventionally used in the back-illumination mode for thermal imaging in the 3- to 5- $\mu\text{m}$  infrared spectral band, have been shown to exhibit excellent photo-response in the near-ultraviolet and visible regions when operated in the front-illumination mode. High-quality imaging has been demonstrated in both the visible and 3- to 5- $\mu\text{m}$  bands for front-illuminated  $160 \times 244$ -element detector arrays integrated with monolithic CCD readout circuitry.

Broad-stripe diode lasers with an emission wavelength of 2.29  $\mu\text{m}$  have been fabricated from lattice-matched GaInAsSb/AlGaAsSb double heterostructures grown on GaSb substrates by molecular beam epitaxy (MBE). For pulsed operation at room temperature, these devices exhibit a threshold current density of 1.7  $\text{kA}/\text{cm}^2$  and two-facet differential quantum efficiency of 30 percent, values comparable to the best reported for diode lasers emitting beyond 2  $\mu\text{m}$ .

Continuous operation at room temperature has been demonstrated for graded-index separate-confinement heterostructure (GRIN-SCH) single-quantum-well (SQW) GaAs/AlGaAs ridge-waveguide diode lasers grown on a Si substrate by organometallic vapor phase epitaxy, without the use of MBE. Incorporating a defect-filtering layer of thermally cycled GaAs to improve the quality of the laser structure has made it possible to achieve CW threshold currents as low as 25 mA and a differential quantum efficiency of 55 percent.

The high-temperature reaction between ammonia and diborane has been utilized for chemical vapor deposition of boron nitride to coat fused silica crucibles for use in the bulk growth of InP crystals from the melt. For nominally undoped crystals grown in such crucibles by the liquid-encapsulated Czochralski method, the purity has been found to be the same as that of control crystals grown in pyrolytic boron nitride crucibles, which are much more expensive.

### 4. SUBMICROMETER TECHNOLOGY

Electron-beam direct-write technology has been used to fabricate photomasks for 193-nm lithography. A variety of shapes and sizes (0.1 to 22  $\mu\text{m}$ ) were patterned in aluminum thin films on high-purity fused-silica substrates.

Silylation methods have been applied to 193-nm lithography. Positive-tone patterning was obtained by combining exposure-induced crosslinking with the appropriate silylation conditions, and resolution of 0.4  $\mu\text{m}$  was demonstrated at a dose of 60  $\text{mJ}/\text{cm}^2$ .

### 5. MICROELECTRONICS

A high-yield, high-throughput process has been developed for producing mechanically rugged, back-illuminated thinned CCD imagers from finished wafers of front-illuminated devices. The back-illuminated devices provide at least  $20\times$  greater quantum efficiency at 400 nm than front-illuminated devices, and show even more advantage at shorter wavelengths.

Both CCD imaging devices and bulk Si wafers have been irradiated with high-energy protons, and the resulting damage characterized. The increased dark current and reduced charge transfer efficiency suffered by the CCDs were reduced by a background charge of several tens of electrons per well, and studies of bulk Si wafers indicated that increasing the substrate resistivity may result in CCDs more resistant to proton damage.

A generic CCD signal processor, which can be used as a one-dimensional correlator, a two-dimensional matched filter, and a two-layer neural net computing module, has been designed based on a vector-matrix-product computing algorithm. When used as a neural net processor, the device will provide 2016 programmable interconnections between a fully connected two-layer net with 144 input nodes and 14 output nodes, perform 2.8 billion arithmetic operations per second, and dissipate less than 2 W at a 10-MHz clock rate.

## 6. ANALOG DEVICE TECHNOLOGY

A microstrip resonator with a superconducting thin-film metallization has been used to measure the dielectric properties of evaporated silicon monoxide at 4.2 K. Results at 1.3 GHz indicate a relative dielectric constant equal to 6.2 and a loss tangent between  $1.3$  and  $1.5 \times 10^{-4}$ .

Electrostatic analysis predicts charge transfer inefficiency in single-gate-level CCDs caused by local potential minima and lack of buried-channel confinement in the interelectrode gap regions. Further analysis shows that a very simple processing step (shallow counterdoping in the gap) will significantly reduce these potential minima and isolate the channel from the surface.

# REPORTS ON SOLID STATE RESEARCH

1 August through 31 October 1989

## PUBLISHED REPORTS

### Journal Articles

#### JA No.

6135	Spectroscopy and Photochemistry of Gases, Adsorbates, and Liquids	M. Rothschild	<i>Laser Microfabrication</i> , edited by D.J. Ehrlich and J.Y. Tsao (Academic, Boston, 1989), pp. 163-230
6175	An In-Situ Study of the UV Photochemistry of Adsorbed $\text{TiCl}_4$ by FTIR Spectroscopy	P.V. Purohit M. Rothschild D.J. Ehrlich	<i>Mechanisms of Reactions of Organometallic Compounds with Surfaces</i> , edited by D.J. Cole-Hamilton and J.O. Williams (Plenum, New York, 1989), pp. 55-62
6215	Sum Frequency Generation of Sodium-Resonance Radiation	T.H. Jeys A.A. Brailove A. Mooradian	Appl. Opt. <b>28</b> , 2588 (1989), DTIC AD-A212723
6223	Zone-Melting Recrystallization with Enhanced Radiative Heating for Preparation of Subboundary-Free Silicon-on-Insulator Thin Films	C.K. Chen J.S. Im	Appl. Phys. Lett. <b>55</b> , 1238 (1989)
6225	End-Pumped Nd:LaF <sub>3</sub> and Nd:LaMgAl <sub>11</sub> O <sub>19</sub> Lasers	T.Y. Fan M.R. Kokta*	IEEE J. Quantum Electron. <b>25</b> , 1845 (1989)
6261	Growth of Textured Diamond Films on Foreign Substrates from Attached Seed Crystals	M.W. Geis	Appl. Phys. Lett. <b>55</b> , 550 (1989)
6262	Superconductive Analog Signal Processing Devices	R.S. Withers R.W. Ralston	Proc. IEEE <b>77</b> , 1247 (1989)

---

\* Author not at Lincoln Laboratory.



**JA No.**

- |      |   |  |   |
|------|---|--|---|
| 6263 | 128 × 128-Element IrSi Schottky-Barrier Focal Plane Arrays for Long-Wavelength Infrared Imaging                               | B-Y. Tsaur<br>M.J. McNutt*<br>R.A. Bredthauer*<br>R.B. Mattson*            | IEEE Electron Device Lett. <b>10</b> , 361 (1989) |
| 6265 | Microchannel Heat Sinks for Two-Dimensional High-Power-Density Diode Laser Arrays   | L.J. Missaggia<br>J.N. Walpole<br>Z.L. Liao<br>R.J. Phillips*              | IEEE J. Quantum Electron. <b>25</b> , 1988 (1989) |
| 6284 | New OMVPE Reactor for Large Area Uniform Deposition of InP and Related Alloys   | S.C. Palmateer<br>S.H. Groves<br>J.W. Caunt<br>D.L. Hovey                  | J. Electron. Mater. <b>18</b> , 645 (1989)        |
| 6298 | Effects of Excimer Laser Irradiation on the Transmission, Index of Refraction, and Density of Ultra-violet Grade Fused Silica | M. Rothschild<br>D.J. Ehrlich<br>D.C. Shaver                               | Appl. Phys. Lett. <b>55</b> , 1276 (1989)         |
| 6308 | Scalable, End-Pumped, Diode-Laser-Pumped Laser  | T.Y. Fan<br>A. Sanchez<br>W.E. DeFeo                                       | Opt. Lett. <b>14</b> , 1057 (1989)                |
| 6310 | Oscillations up to 420 GHz in GaAs/AlAs Resonant Tunneling Diodes   | E.R. Brown<br>T.C.L.G. Sollner<br>C.D. Parker<br>W.D. Goodhue<br>C.L. Chen | Appl. Phys. Lett. <b>55</b> , 1777 (1989)         |
| 6313 | Femtosecond Passively Mode-Locked Ti:Al <sub>2</sub> O <sub>3</sub> Laser with a Nonlinear External Cavity                    | J. Goodberlet*<br>J. Wang*<br>J.G. Fujimoto*<br>P.A. Schulz                | Opt. Lett. <b>14</b> , 1125 (1989)                |

**Meeting Speeches****MS No.**

- |       |  |                        |  |
|-------|--|------------------------|--|
| 7882A | Bulk-Acoustic-Wave Resonators Using Holographic Reflection Gratings in Photorefractive Materials | D.E. Oates<br>J.Y. Pan | <i>Ferroelectrics</i> (Gordon and Breach, New York, 1989), Vol. 92, pp. 253-262, DTIC AD-A212194 |
|-------|--|------------------------|--|

---

\* Author not at Lincoln Laboratory.

**MS No.**

- |      |  |   |   |
|------|--|---|---|
| 8208 | MNOS/CCD Circuits for Neural Network Implementations   | J.P. Sage<br>R.S. Withers<br>K.E. Thompson                    | Proc. 1989 Intl. Symp. on Circuits and Systems, Portland, Oregon, 9-11 May 1989, pp. 1207-1209                              |
| 8223 | Programmable, Four-Channel, 128-Sample, 40-Ms/s Analog-Ternary Correlator                                    | S.C. Munroe<br>D.R. Arsenault<br>K.E. Thompson<br>A.L. Lattes | Proc. 1989 IEEE Custom Integrated Circuits Conf., San Diego, California, 15-18 May 1989, pp. 25.1.1-25.1.4, DTIC AD-A208548 |
| 8260 | Superconducting Stripline Resonators and High-T <sub>c</sub> Materials                                       | D.E. Oates<br>A.C. Anderson<br>B.S. Shih                      | 1989 IEEE MTT-S Digest R-2 (1989), pp. 627-630, DTIC AD-A209965   |
| 8349 | Planarizing a-C:H and SiO <sub>2</sub> Films Prepared by Bias Electron Cyclotron Resonance Plasma Deposition | M.W. Horn<br>S.W. Pang<br>M. Rothschild<br>G.A. Ditmer*       | <i>Proceedings, Sixth International IEEE VLSI Multilevel Interconnection Conference</i> (IEEE, New York, 1989), pp. 65-71   |

\* \* \* \* \*

## UNPUBLISHED REPORTS

### Journal Articles

**JA No.**

- |       |   |   |                               |
|-------|---|---|-------------------------------|
| 6287A | Electrical, Crystallographic, and Optical Properties of ArF Laser Modified Diamond Surfaces | M.W. Geis<br>M. Rothschild<br>R.R. Kunz<br>R.L. Aggarwal<br>K.F. Wall<br>C.D. Parker<br>K.A. McIntosh<br>N.N. Efremow<br>J.J. Zayhowski<br>D.J. Ehrlich<br>J.E. Butler* | Accepted by Appl. Phys. Lett. |
|-------|---|---|-------------------------------|

---

\* Author not at Lincoln Laboratory.

**JA No.**

6305	1-Gb/s Free-Space Optical Interconnection	D.Z. Tsang	Accepted by Appl. Opt.
6312	Controlled-Ambient Photolithography of Polysilane Resists at 193 nm	R.R. Kunz S.P. Sawan* M. Rothschild Y. Tsai* D.J. Ehrlich	Accepted by J. Vac. Sci. Technol. B
6320	Amplification of Femtosecond Pulses in Ti:Al <sub>2</sub> O <sub>3</sub> Using an Injection Seeded Laser	M.J. LaGasse* R.W. Schoenlein* J.G. Fujimoto* P.A. Schulz	Accepted by Opt. Lett.
6323	External-Cavity Coherent Operation of InGaAsP Buried-Heterostructure Laser Array	V. Diadiuk Z.L. Liao J.N. Walpole J.W. Caunt R.C. Williamson	Accepted by Appl. Phys. Lett.
6324	Pump Source Requirements for End-Pumped Lasers	T.Y. Fan A. Sanchez	Accepted by IEEE J. Quantum Electron.
6327	High-Performance Optical Analog Link Using External Modulator	G.E. Betts L.M. Johnson C.H. Cox, III S.D. Lowney	Accepted by IEEE Photon. Technol. Lett.
6330	Analog Fiber-Optic Links: A Theoretical and Experimental Comparison of Direct and External Modulation	C.H. Cox, III G.E. Betts L.M. Johnson	Accepted by IEEE Trans. Microwave Theory Tech. jointly with J. Lightwave Technol.
6350	Reduced-Confinement Antennas for GaAlAs Integrated Optical Waveguides	D.E. Bossi W.D. Goodhue M.C. Finn K. Rauschenbach R.H. Rediker	Accepted by Appl. Phys. Lett.
6360	Lasers	H.J. Zeiger P.L. Kelley	Accepted by <i>Encyclopedia of Physics</i>

---

\* Author not at Lincoln Laboratory.

**JA No.**

6362	Surface-Energy-Induced Mass Transport Phenomenon in Annealing of Etched Compound Semiconductor Structures: Theoretical Modeling and Experimental Confirmation	Z.L. Liao H.J. Zeiger	Accepted by J. Appl. Phys.
6370	High-Performance, Externally Modulated Analog Fiber-Optic Links	C.H. Cox, III G.E. Betts L.M. Johnson	Accepted by Opt. News

**Meeting Speeches\*****MS No.**

8070A	Mass Transport: New Micro-fabrication Technique for New Semiconductor Optoelectronics	Z.L. Liao	Heterostructure Device Seminar, Cambridge, Massachusetts, 18 September 1989
8252C	High-Speed Resonant Tunneling	E.R. Brown	Seminar, Sandia Laboratory, Albuquerque, New Mexico, 20 October 1989
8283	Novel Diode Pumped Lasers	T.Y. Fan	} OSA Annual Meeting, Orlando, Florida, 15-20 October 1989
8445	Optical Interconnections — Status and Prospects	D.Z. Tsang	
8305A	Wideband Infrared Heterodyne Detectors	D.L. Spears	} Electronic Imaging '89 East, Boston, Massachusetts, 2-5 October 1989
8531	Schottky-Barrier Infrared Detectors and Focal Plane Arrays	B-Y. Tsaur	
8305B	Wide Bandwidth IR Heterodyne Detectors	D.L. Spears	} LEOS '89, Orlando, Florida, 17-20 October 1989
8451	Low Noise CCD Imagers	B.E. Burke	
8452	Solid State Lasers	A. Sanchez	

---

\* Titles of meeting speeches are listed for information only. No copies are available for distribution.



**MS No.**

8341A	Doping Profile Optimization in Silicon Permeable Base Transistors for High-Frequency High-Voltage Operation	D.D. Rathman M.A. Hollis R.A. Murphy A.L. McWhorter M.J. McNamara	13th Biennial IEEE/Cornell Conf. on Advanced Concepts in High Speed Semiconductor Devices and Circuits, Cornell University, Ithaca, New York, 7-9 August 1989
8356	Stripline Measurements of Surface Resistance: Relation to HTSC Film Properties and Deposition Methods	D.E. Oates A.C. Anderson	Processing of Films for High $T_c$ Superconducting Electronics, Santa Clara, California, 10-12 October 1989
8400	Modeling of Diode Pumped Solid-State Lasers	T.Y. Fan	Interdisciplinary Laser Science Conf., Stanford, California, 28-31 August 1989
8402B	Homoepitaxial Diamond Films	M.W. Geis	American Vacuum Society, University Park, Pennsylvania, 21 September 1989
8427	Excimer Laser Induced Damage in Fused Silica	M. Rothschild D.J. Ehrlich D.C. Shaver	Microcircuit Engineering 89, Cambridge, England, 26-28 September 1989
8438	Role of Nitrogen Ions in Ion-Beam Reactive Sputtering of NbN	D.J. Lichtenwalner A.C. Anderson D.A. Rudman*	American Vacuum Society Symp., Boston, Massachusetts, 23-27 October 1989

---

\* Author not at Lincoln Laboratory.

# MS No.

8441	Reduced-Confinement GaAlAs Tapered Waveguide Antenna Grown by Molecular Beam Epitaxy	W.D. Goodhue D.E. Bossi M.C. Finn J.W. Bales R.H. Rediker	10th MBE Workshop, North Carolina State University, Raleigh-Durham, North Carolina, 13-15 September 1989
8444	Frequency Domain Analysis of Time-Dependent RHEED Intensity Data	G.W. Turner B.A. Nechay S.J. Eglash	
8455A	Excimer Laser Patterning Technologies for Microfabrication	D.J. Ehrlich	Dry Process Symp., Tokyo, Japan, 30-31 October 1989
8477	Resonant Tunneling: Physics and Modelling	E.R. Brown	7th Intl. Workshop on Future Electron Devices, Nagoya, Japan, 2-4 October 1989
8492	Damage and Profile Control for Dry Etching	S.W. Pang	American Vacuum Society 26th National Symp., Boston, Massachusetts, 23-27 October 1989
8494	High-Frequency Applications of Resonant-Tunneling Devices	T.C.L.G. Sollner E.R. Brown W.D. Goodhue	NATO Advanced Study Institute, Bonas, France, 10-23 September 1989
8514A	Preparation of YBCO Thin Film by Multisource Deposition	M. Bhushan	DARPA Workshop on Super- conductivity, Santa Barbara, California, 12 September 1989
8538	HTSC Microwave Passive Devices	W.G. Lyons	
8516, A,B,C	Ti:Al <sub>2</sub> O <sub>3</sub> Lasers: From Continuous to Femtosecond Operation	P.A. Schulz	Seminar, Worcester Polytechnic Institute, Worcester, Massachu- setts, 25 September 1989; Seminar, Sandia Laboratory, Albuquerque, New Mexico, 2 October 1989; Seminar, Coherent Associates, Boulder, Colorado, 3 October 1989; Seminar, Princeton University, Princeton, New Jersey, 30 October 1989

**MS No.**

8523A	YBCO Film Preparation by Sputtering Techniques	A.C. Anderson W.T. Brogan L.S. Yu-Jahnes R.L. Slattery M. Bhushan	Workshop on Superconductive Electronics, St. Michaels, Maryland, 1-5 October 1989
8563	Analog Signal Correlator Design and Operation	J.B. Green M. Bhushan	
8569	Stripline Resonators for Oscillator Stabilization	D.E. Oates	
8558	Superconductive Microwave Devices and Circuits	R.S. Withers	IEEE Waves and Devices Group Meeting, Phoenix, Arizona, 7 September 1989
8573	Capless Rapid Thermal Annealing of Si- and Zn-Implanted InP	J.D. Woodhouse M.C. Gaidis	Heatpulse Owners Technology Group Meeting, Boston, Massachusetts, 12 September 1989
8584	First, Second, and Third Best Semiconductors	M.W. Geis	Diamond Consortium, University Park, Pennsylvania, 22 September 1989

## ORGANIZATION

### SOLID STATE DIVISION

A. L. McWhorter, *Head*  
I. Melngailis, *Associate Head*  
E. Stern, *Associate Head*  
J. F. Goodwin, *Assistant*  
  
D. J. Ehrlich, *Senior Staff*  
N. L. DeMeo, Jr., *Associate Staff*  
J. W. Caunt, *Assistant Staff*

### SUBMICROMETER TECHNOLOGY

D. C. Shaver, *Leader*  
M. Rothschild, *Assistant Leader*

### QUANTUM ELECTRONICS

A. Mooradian, *Leader*  
P. L. Kelley, *Associate Leader*  
A. Sanchez-Rubio, *Assistant Leader*

Astolfi, D. K.	Hartney, M. A.	Aggarwal, R. L.	Jeys, T. H.
Craig, D. M.	Horn, M. W.	Barch, W. E.	Korn, J. A.
Dennis, C. L.	Kunz, R. R.	Belanger, L. J.	Lacovara, P.
Doran, S. P.	Lyszczarz, T. M.	Cook, C. C.	Le, H. Q.
Efremow, N. N., Jr.	Maki, P. A.	Daneu, V.	Menyuk, N.†
Forte, A. R.	Melngailis, J.†	DeFeo, W. E.	Ochoa, J. R.
Gajar, S. A.*	Pang, S. W.	DiCecca, S.	Schulz, P. A.
Geis, M. W.	Sedlacek, J. H. C.	Dill, C. D., III	Seemungal, W. A.
Goodman, R. B.	Uttaro, R. S.	Fan, T. Y.	Sharfin, W. F.
		Hancock, R. C.	Sullivan, D. J.
		Henion, S. R.	Wall, K. F.
		Hotaling, T. C.	Zayhowski, J. J.

### ELECTRONIC MATERIALS

A. J. Strauss, *Leader*  
B-Y. Tsaur, *Associate Leader*  
H. J. Zeiger, *Senior Staff*

Anderson, C. H., Jr.	Eglash, S. J.	McGilvary, W. L.
Button, M. J.	Fahey, R. E.	Nechay, B. A.
Chen, C. K.	Finn, M. C.	Nitishin, P. M.
Choi, H. K.	Iseler, G. W.	Pantano, J. V.
Clark, H. R., Jr.	Kolesar, D. F.	Tracy, D. M.
Connors, M. K.	Krohn, L., Jr.	Turner, G. W.
Delaney, E. J.	Mastromattei, E. L.	Wang, C. A.
	Mattia, J. P.*	

---

\* Research Assistant

† Part Time

## APPLIED PHYSICS

R. C. Williamson, *Leader*  
 D. L. Spears, *Assistant Leader*  
 R. H. Rediker, *Senior Staff*

Aull, B. F.	Lind, T. A.
Bailey, R. J.	Missaggia, L. J.
Barwick, D. S.*	Mull, D. E.
Betts, G. E.	O'Donnell, F. J.
Bossi, D. E.*	Palmacci, S. T.
Corcoran, C. J.*	Palmateer, S. C.
Cox, C. H., III	Rauschenbach, K.
Diadiuk, V.	Reeder, R. E.
Donnelly, J. P.	Roussell, H. V.
Ferrante, G. A.	Shiple, S. D.*
Groves, S. H.	Tsang, D. Z.
Harman, T. C.	Walpole, J. N.
Hovey, D. L.	Woodhouse, J. D.
Johnson, L. M.	Yee, A. C.
Liau, Z. L.	

## ANALOG DEVICE TECHNOLOGY

R. W. Ralston, *Leader*  
 R. S. Withers, *Associate Leader*  
 R. M. Lerner, *Senior Staff* †

Anderson, A. C.	Lyons, W. G.
Arsenault, D. R.	Macedo, E. M., Jr.
Bhushan, M.	Munroe, S. C.
Boisvert, R. R.	Oates, D. E.
Brogan, W. T.	Sage, J. P.
Denneno, A. P.	Seaver, M. M.
Fitch, G. L.	Shih, B. S.*
Green, J. B.	Slattery, R. L.
Hamm, J. M.	Westerheim, A. C.*
Holtham, J. H.	Whitley, D. B.
Lattes, A. L.	Yu-Jahnes, L-S.*
Lichtenwalner, D. J.*	

## MICROELECTRONICS

R. A. Murphy, *Leader*  
 E. D. Savoye, *Associate Leader*  
 B. B. Kosicki, *Assistant Leader*  
 R. W. Chick, *Senior Staff*

Actis, R.	Durant, G. L.	McGonagle, W. H.
Bales, J. W.*	Felton, B. J.	McIntosh, K. A.
Bergeron, N. J.	Gladden, D. B.‡	Mountain, R. W.
Bozler, C. O.	Goodhue, W. D.	Nichols, K. B.
Brown, E. R.	Gray, R. V.	Parker, C. D.
Burke, B. E.	Gregory, J. A.	Percival, K. A.
Calawa, A. R.	Hollis, M. A.	Pichler, H. H.
Chen, C. L.	Huang, C. M.	Rabe, S.
Chiang, A. M.	Hurley, E. T.	Rathman, D. D.
Chuang, M. L.*	Johnson, B. W.	Reich, R. K.
Clifton, B. J.	Johnson, K. F.	Reinold, J. H., Jr.
Cooper, M. J.	LaFranchise, J. R.	Smith, F. W.*
Crenshaw, D. L.*	Lincoln, G. A., Jr.	Sollner, T. C. L. G.
Daniels, P. J.	Mahoney, L. J.	Vera, A.
Doherty, C. L., Jr.	Manfra, M. J.	Wilde, R. E.
Dolat, V. S.	Mathews, R. H.	Young, D. J.
Donahue, T. C.		

---

\* Research Assistant

† Part Time

‡ Staff Associate



# 1. ELECTROOPTICAL DEVICES

## 1.1 EFFECTS OF P<sup>+</sup> IMPLANTS AND ANNEALING ON Zn<sup>+</sup>-IMPLANTED InP:Fe

Formation of shallow, highly doped *p*-type ion-implanted layers in InP is difficult because most *p*-type implanted dopants (i.e., Be, Mg, Zn and Cd) exhibit severe redistribution upon post-implant annealing. It has recently been reported that a co-implant of phosphorus and beryllium produces a shallow *p*<sup>+</sup> surface layer which exhibits improved electrical activation over single beryllium implants [1]. The phosphorus-rich surface, formed as a result of the co-implant, is believed to increase the concentration of available In sites at the surface, which in turn increases the probability of substitutional doping of Be on In vacancies. The resulting increase in Be activation reduces the amount of interstitial Be that would otherwise diffuse into the bulk. Here we report the effects of P<sup>+</sup> co-implants, implantation temperature, and type of post-implant anneal on the hole concentration depth profiles for high- and low-dose Zn<sup>+</sup> implants in InP:Fe. The purpose of this study was to determine which, if any, combination of implant and anneal conditions produces hole carrier concentration profiles that best approximate the theoretical Lindhard-Scharff-Schiøtt (LSS) [2] implanted profile.

For these experiments, high-resistivity ( $\rho > 10^7 \Omega\text{-cm}$ ), Fe-doped InP crystals were cut into (100)-oriented wafers which were lapped and polished using a 1-percent Br-methanol solution. Samples cut from the wafers were etched in 0.5-percent Br-methanol prior to implantation. Half of the samples were first implanted with 100-keV,  $5 \times 10^{13}$ - or  $5 \times 10^{14}$ -  $\text{cm}^{-2}$  P<sup>+</sup> ions at 25°C. Next, all samples were implanted with 200-keV,  $5 \times 10^{13}$ - or  $5 \times 10^{14}$ -  $\text{cm}^{-2}$  Zn<sup>+</sup> ions at 25 or 180°C. The P<sup>+</sup> and Zn<sup>+</sup> energies were chosen such that the two implanted distributions overlapped. Following implantation, each sample was cleaved in half for different annealing treatments. Conventional annealing was performed in a graphite-strip-heater system at 750°C for 10 min using a phosphosilicate glass (PSG) encapsulant [3]. Rapid thermal annealing (RTA) at 900°C for 10 s was performed in a tungsten-halogen-lamp system using a capless enhanced-overpressure-proximity technique (EOP) [4]. The EOP technique utilizes a Sn-coated InP source wafer, spaced about 0.1 mm from the sample to provide a phosphorus overpressure during RTA. Hole concentration vs depth profiles were obtained by a Hall-effect measurement and step-stripping technique [5]. To facilitate such measurements, AuZnAu contacts were microalloyed at 450°C and cloverleaf mesas were etched into the surface. A solution of 20-percent iodic acid in deionized water was used for layer removal in steps of 200 to 400 Å between electrical measurements. Details of the fabrication procedure and computer program used to reduce the electrical data are described in Reference 5.

Our results for low-dose implants are presented in Figure 1-1, which illustrates the hole carrier concentration vs depth for 200-keV Zn<sup>+</sup> implanted into InP to a dose of  $5 \times 10^{13} \text{ cm}^{-2}$ . These samples were implanted at 25°C with or without an additional 100-keV P<sup>+</sup> co-implant at the same dose. The dashed line represents the theoretical LSS profile for Zn<sup>+</sup> in InP. For the samples annealed at 750°C, a peak hole concentration of about  $2 \times 10^{18} \text{ cm}^{-3}$  was attained. The depth of the distribution, however, shows significant indiffusion of the carriers, independent of P<sup>+</sup> co-implantation. For the samples annealed at 900°C for 10 s, the sample implanted without P has a very broadly peaked hole concentration

of about  $10^{18} \text{ cm}^{-3}$  which extends about  $3000 \text{ \AA}$  into the substrate. The sample co-implanted with  $\text{P}^+$  shows a much improved peak hole concentration of about  $3.5 \times 10^{18} \text{ cm}^{-3}$  and closely approximates the theoretical LSS distribution.

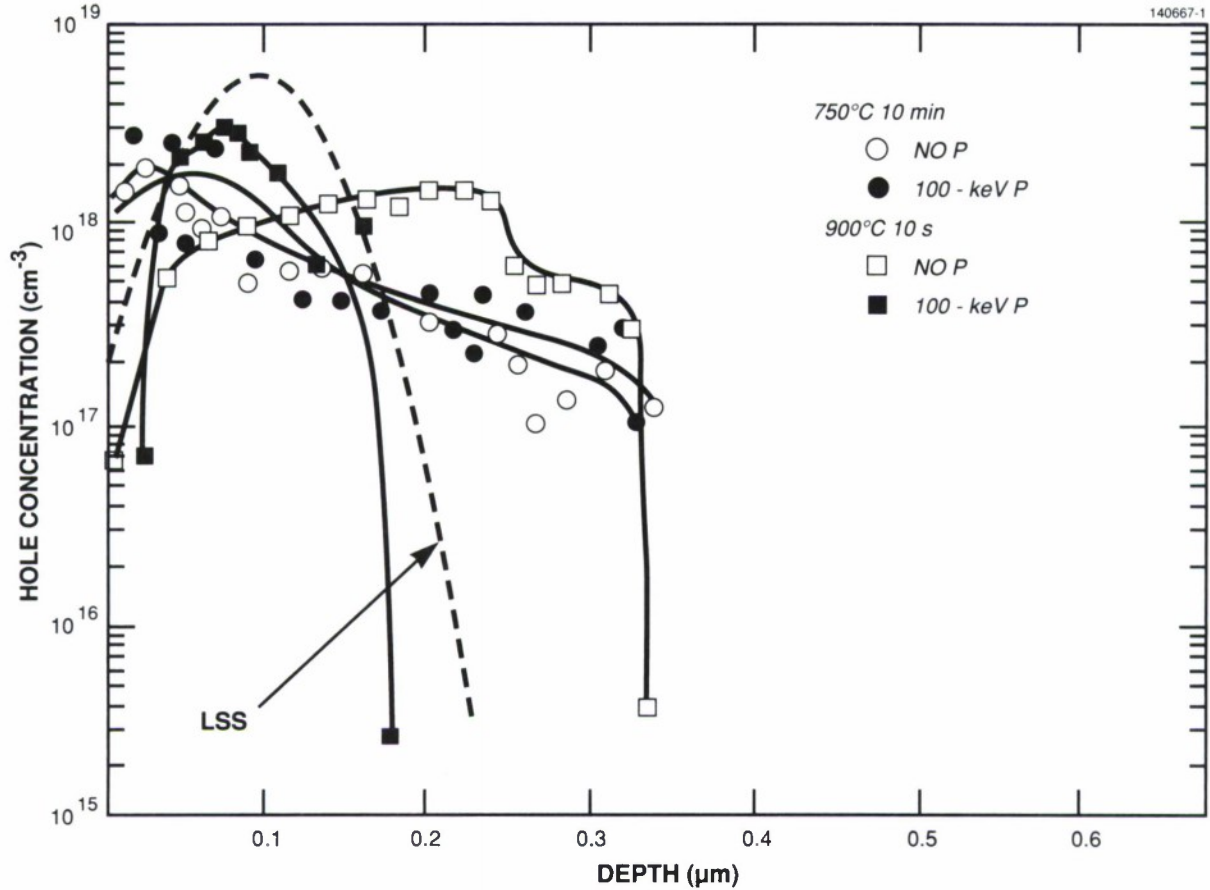


Figure 1-1. Hole concentration vs depth for 200-keV,  $5 \times 10^{13} \text{-cm}^{-2}$   $\text{Zn}^+$  implanted into  $\text{InP:Fe}$  at  $25^\circ\text{C}$  with and without 100-keV,  $5 \times 10^{13} \text{-cm}^{-2}$   $\text{P}^+$  implanted at  $25^\circ\text{C}$  and for two annealing treatments.

It should be noted that the hole concentration in the very-near-surface region ( $\leq 500 \text{ \AA}$ ) in the samples annealed by EOP-RTA is very much reduced compared with that obtained by conventional annealing. This reduction can result from compensation caused by residual implant damage, outdiffusion of Zn atoms through the surface and/or indiffusion of Sn from the EOP source wafer during annealing. Formation of  $n$ -type skin layers in EOP-annealed  $\text{InP}$  substrates, presumably caused by Sn contamination, has been shown to occur when spacings between the source wafer and sample are  $< 0.1 \text{ mm}$  [5]. Increasing the spacing to  $\geq 0.3 \text{ mm}$  was found to eliminate the  $n$ -type layer formation [4]. Surface layer

compensation effects caused by Sn incorporation are more completely characterized and described in Reference 5.

The data of Figure 1-1 indicate that the presence of additional phosphorus does not significantly change the depth profiles for the 750°C 10-min anneals. It is very likely that enough phosphorus is lost through the surface during the relatively long annealing period to lower the concentration of In vacancies, thereby increasing the probability of Zn diffusion. The advantage of using a P<sup>+</sup> co-implant is clearly seen in the case of rapid annealing. The peak hole concentration is about 4 times higher and dopant redistribution is considerably reduced when using a co-implant followed by RTA. Elevated-temperature (180°C) implants were tried in order to reduce possible compensation caused by damage production during heavy ion bombardment. Although not depicted here, the peak carrier concentrations and general distributions in profiles obtained for the 180°C implanted samples were virtually identical to those in Figure 1-1. However, a 25- to 30-percent increase in diffusion toward the bulk was observed, which is not unexpected for elevated-temperature implants [6].

In an effort to achieve higher peak carrier concentrations, high-dose Zn<sup>+</sup> implants were also investigated. Figure 1-2 shows the hole carrier concentration vs depth for 200-keV Zn<sup>+</sup> implanted into InP to a dose of  $5 \times 10^{14} \text{ cm}^{-2}$ . These samples were implanted at 25°C with and without an additional 100-keV,  $5 \times 10^{14} \text{ cm}^{-2}$  P<sup>+</sup> co-implant. Both samples annealed at 750°C show broad carrier distributions with peak hole concentrations of about  $2 \times 10^{18} \text{ cm}^{-3}$ . Phosphorus co-implantation in this case reduced dopant redistribution, indicating that the 10-min anneal time is short enough to prevent substantial phosphorus loss for high-dose P<sup>+</sup> implants. It is interesting to note that although the Zn<sup>+</sup> dose has been increased by an order of magnitude, the peak hole concentration has increased only moderately and extends to a much greater depth compared with that of the lower dose implants. This behavior is typical of that observed for other *p*-type dopants, such as Mg and Cd, for which the peak carrier concentration saturates at about  $2 \times 10^{18} \text{ cm}^{-3}$ , and the diffusion tail extends deeper into the substrate with increasing dose [5]. RTA at 900°C for 10 s results in an increase of the peak hole concentrations to 3 and  $6 \times 10^{18} \text{ cm}^{-3}$  for the single and co-implanted samples, respectively. Both profiles do, however, exhibit enhanced dopant indiffusion. Elevated-temperature (180°C) implants performed at the higher doses exhibited profiles similar to those of Figure 1-2. The profiles were somewhat deeper than for the 25°C implants, and a hole concentration of  $8 \times 10^{18} \text{ cm}^{-3}$  was obtained on a P<sup>+</sup> co-implanted sample annealed at 900°C for 10 s. This represents the most significant increase in hole concentration observed in these experiments and is among the highest carrier concentrations reported for *p*-type implanted InP.

A summary of the peak hole concentrations and profile shapes for all implant and anneal conditions is given in Table 1-1. The results indicate that relatively shallow *p*-type layer formation by Zn<sup>+</sup> implantation is only achieved for low-dose dual implants of Zn<sup>+</sup> and P<sup>+</sup> followed by RTA. It is quite clear that increasing the concentration of available In sites at the surface by P<sup>+</sup> co-implantation improves the likelihood of substitutional Zn doping, which leads to higher peak carrier concentrations and less dopant indiffusion. Annealing for longer times, however, probably causes a severe loss of the implanted phosphorus, thus reducing the expected improvement in hole activation.

In the case of high-dose implants, maximum hole concentrations ( $6$  to  $8 \times 10^{18} \text{ cm}^{-3}$ ) are also only realized with dual implantation combined with RTA. Profiles for all implant and annealing parameters, however, exhibit severe indiffusion. If the presence of deep diffusion tails is not detrimental to a given



**TABLE 1-1**  
**Summary of Peak Hole Concentrations and Profile Shapes**  
**for All Implant and Anneal Conditions**

Dose (cm <sup>-2</sup> )	Implant Temperature (°C)	Anneal (°C)	Phosphorus Co-implant (keV)	Peak Concentration (×10 <sup>18</sup> cm <sup>-3</sup> )	Profile Shape
5 × 10 <sup>13</sup>	25	750 10 min	none	2.5	diffused
			100	2.5	diffused
		900 10 s	none	1.5	diffused
			100	3	LSS
	180	750 10 min	none	2	diffused
			100	2	diffused
		900 10 s	none	2	diffused
			100	3.5	LSS
5 × 10 <sup>14</sup>	25	750 10 min	none	2	diffused
			100	2	diffused
		900 10 s	none	3	diffused
			100	6	diffused
	180	750 10 min	none	2	diffused
			100	3	diffused
		900 10 s	none	2	diffused
			100	8	diffused

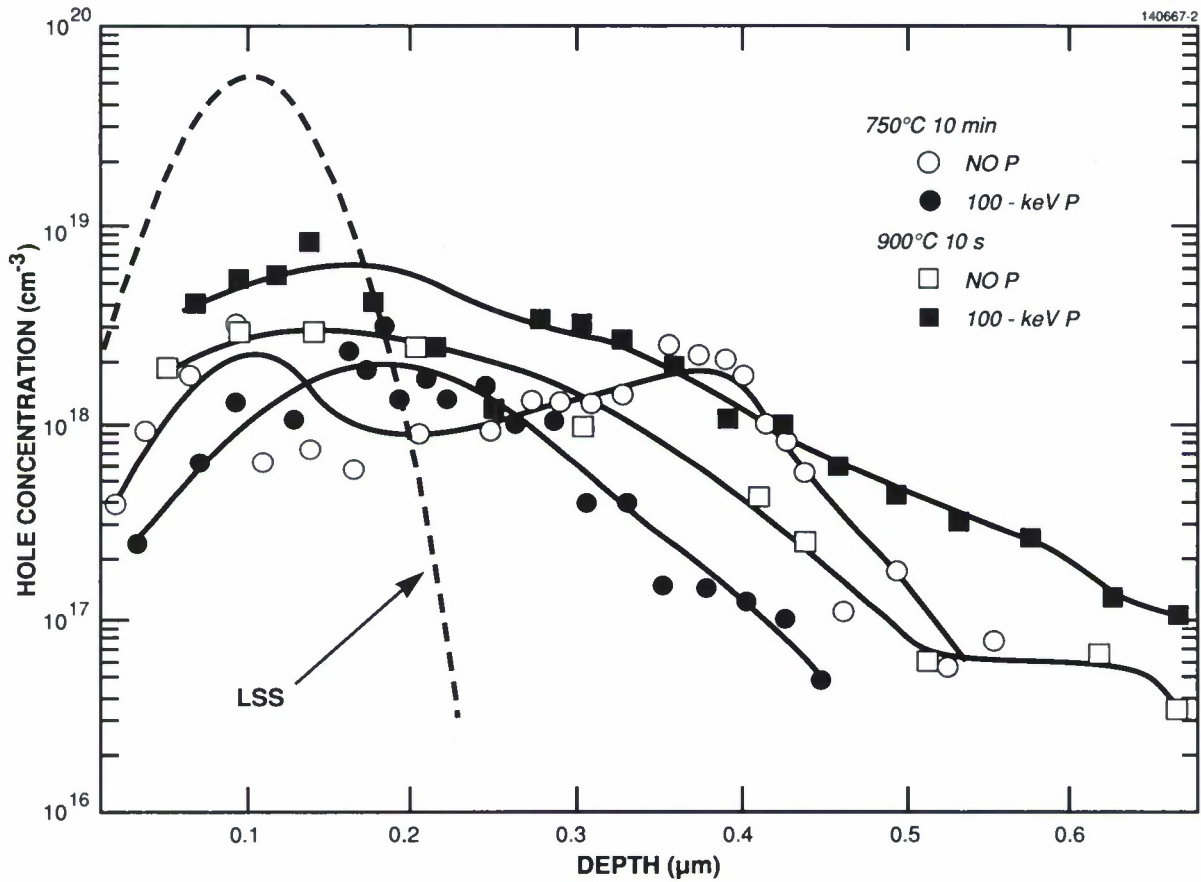


Figure 1-2. Hole concentration vs depth for 200-keV,  $5 \times 10^{14}$ -cm $^{-2}$  Zn $^{+}$  implanted into InP:Fe at 25°C with and without 100-keV,  $5 \times 10^{14}$ -cm $^{-2}$  P $^{+}$  implanted at 25°C and for two annealing treatments.

device fabrication process, then high-dose ion-implanted Zn $^{+}$  and P $^{+}$  may be useful as a predeposition layer for a rapid thermal diffusion (RTD) process. Such an RTD process could be a viable alternative to conventional Zn skin diffusions, because open-ampoule diffusion techniques using In and Zn in flowing PH $_3$ /H $_2$  at 580°C for 20 min yield hole concentrations of only  $2 \times 10^{18}$  cm $^{-3}$  [7].

Although we did not try intermediate doses of Zn $^{+}$  and P $^{+}$  or vary the RTA temperature and times, LSS-type distributions can probably be achieved by optimizing the RTA conditions for each dose. Also, heated phosphorus implants may prove beneficial for the high-dose case because residual *n*-type compensation from damage production should be reduced.

J.D. Woodhouse  
M.C. Gaidis\*

\*Author not presently at Lincoln Laboratory.



## 1.2 GaInAsP/InP BURIED-HETEROSTRUCTURE SURFACE-EMITTING DIODE LASER WITH MONOLITHIC INTEGRATED BIFOCAL MICROLENS

A first attempt has been made to monolithically integrate a microlens with a diode laser. The integrated device showed a narrow beam divergence of  $1.25^\circ$  and is potentially advantageous for fiber coupling, optical interconnects and laser-array applications.

The present device is illustrated in Figure 1-3. It consists of a microlens on one side of the substrate and a buried-heterostructure (BH) waveguide gain region on the other side, which are coupled together by a  $45^\circ$  mirror. The microlens has been made bifocal. The outer portion is a spherical mirror, which is designed to reflect the light back to the BH waveguide and, together with the vertical mirror on the other end of the waveguide, forms the laser resonant cavity. The central portion is a collimating lens, which is designed to fully collimate the light output to a diffraction-limited beam divergence.

The device was fabricated in a Sn-doped,  $n$ -type InP substrate with both sides polished. The measured substrate thickness ( $\sim 400\ \mu\text{m}$ ) became the focal length (or the radius of curvature of the spherical mirror portion) in the microlens design, after some small adjustments had been made to allow for layer etching and growth anticipated in subsequent fabrication. By repeated applications of photolithography and chemical etching, a 10-step cylindrical mesa with an overall diameter of  $200\ \mu\text{m}$  was formed in the InP substrate, with step heights accurately controlled for the desired lens profile [8]. The wafer was then mass-transported at  $870^\circ\text{C}$  to form the microlenses [8].

An optical micrograph of two microlenses is shown in Figure 1-4(a), in which two distinct curvatures can be seen on each microlens. The bifocal nature is more clearly demonstrated by the formation of two distinct images (by reflected light for an object placed near the microscope light source [8]) as shown in Figures 1-4(b) and (c). Note that the image formed by the spherical mirror portion, shown in Figure 1-4(c), is considerably brighter because of the greater light-gathering power of that portion. In fact, the same image can still be seen, but out of focus, in Figure 1-4(b), where the focusing was optimized for the other image. Also note that the two images show a 2:3 ratio in size, which is in good agreement with the present bifocal lens design. (In the present device configuration, that ratio should always be  $(n - 1)/n$ , where  $n = 3.2$  is the refractive index of InP.)

The bifocal microlens has also been investigated by stylus surface profiling as shown in Figure 1-5 (solid trace). The two distinct lens portions can indeed be seen and are in good agreement with calculated profiles, of which the spherical one is shown in Figure 1-5 (dotted curve). We believe the accurate bifocal microlens fabrication has been made possible by the self-controlled lens-forming process [8].

After the microlens fabrication, liquid phase epitaxy (LPE) was used to grow the GaInAsP/InP double heterostructure ( $1.3\text{-}\mu\text{m}$  emission wavelength) on the other side of the wafer. A pattern of thin crosses was then etched on the LPE side. The wafer was subsequently examined under an infrared microscope operated in a transmission mode to precisely determine the position of the thin cross mark with respect to the optical axis of the underlying microlens. The latter was easily located by the concentrated

spot of light produced by the microlens (see Figure 1-6). However, error could be introduced from possible tilt of the microscope stage with respect to the microscope light source. This was detected and corrected by wafer rotation. Using this technique, we believe the position obtained was within  $0.5\ \mu\text{m}$ , an accuracy needed in the placement of the  $45^\circ$  mirror for efficient coupling between the spherical mirror and the BH waveguide.

140667-3

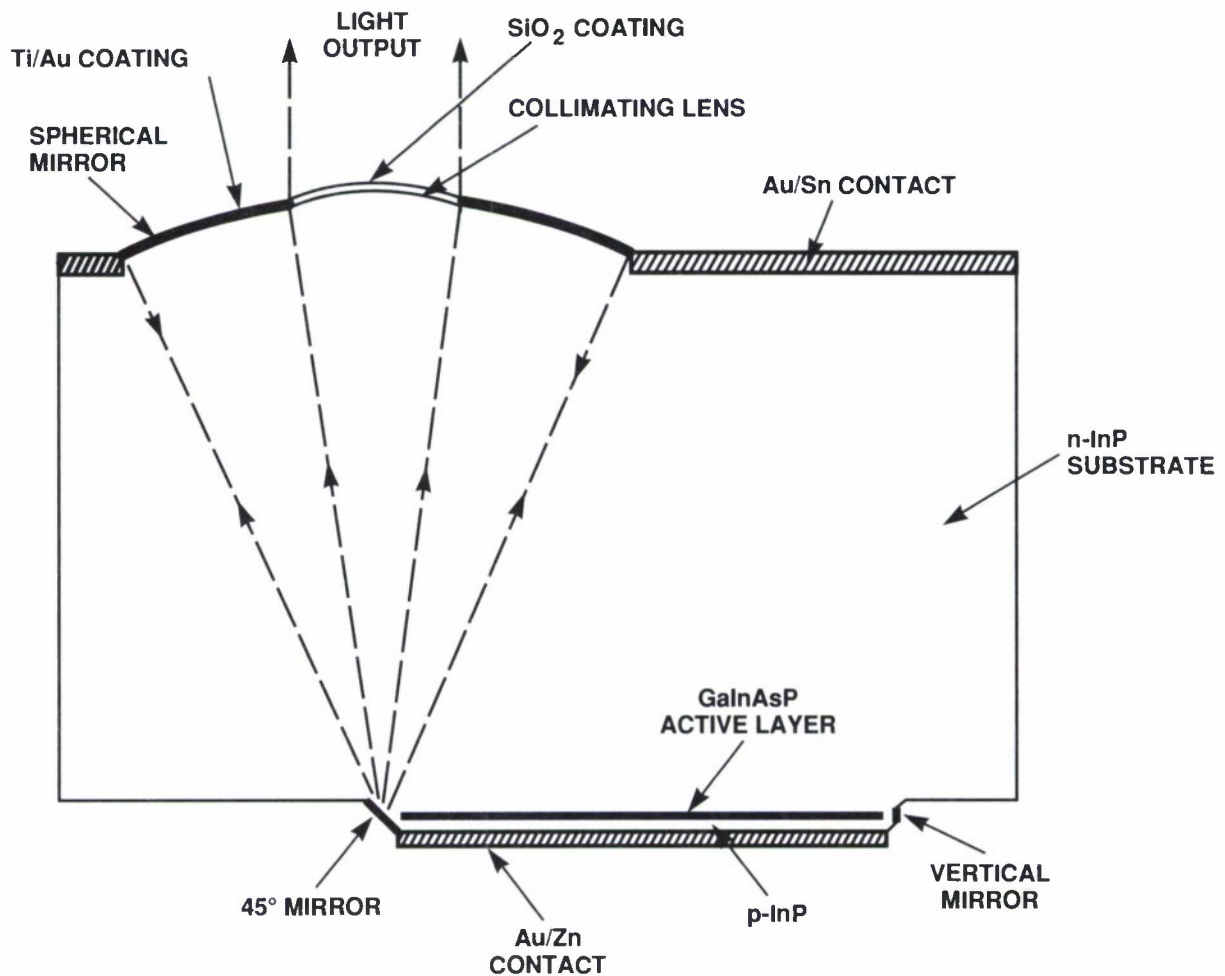
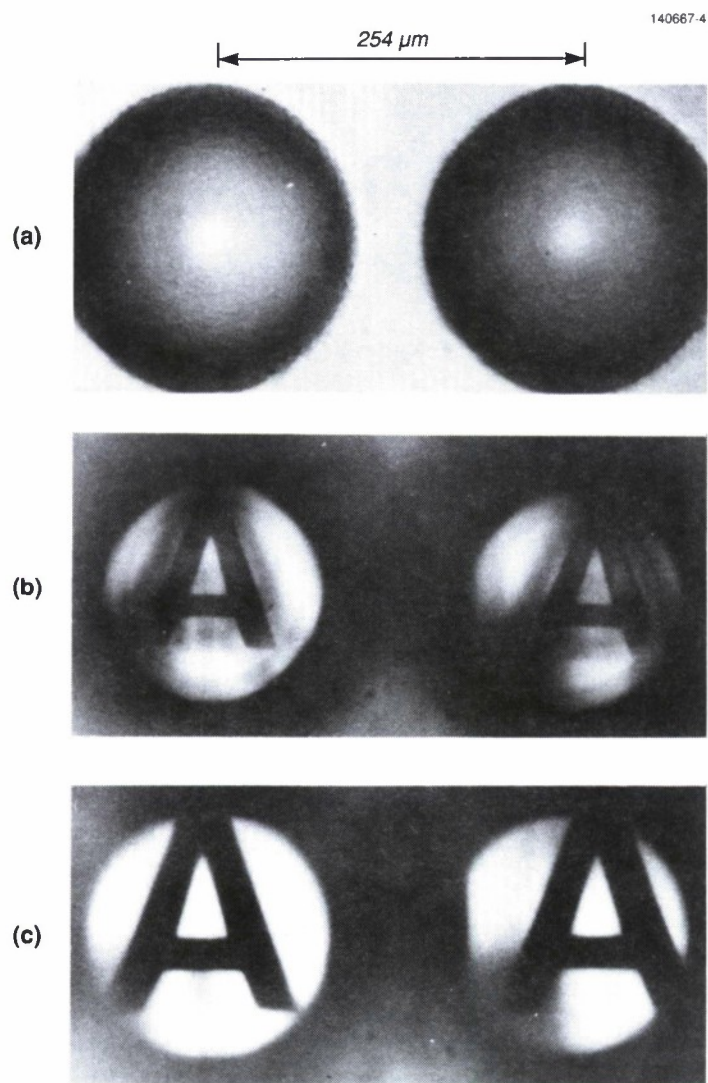


Figure 1-3. Longitudinal cross-sectional view of diode laser with monolithic integrated bifocal microlens. The microlens has two portions with different curvatures and coatings to separately optimize the optical feedback and beam collimation. The GalnAsP/InP gain region is a mass-transported buried heterostructure.



*Figure 1-4. (a) Optical micrographs of two bifocal microlenses. (b), (c) Images formed by collimating lens and spherical mirror portions, respectively.*

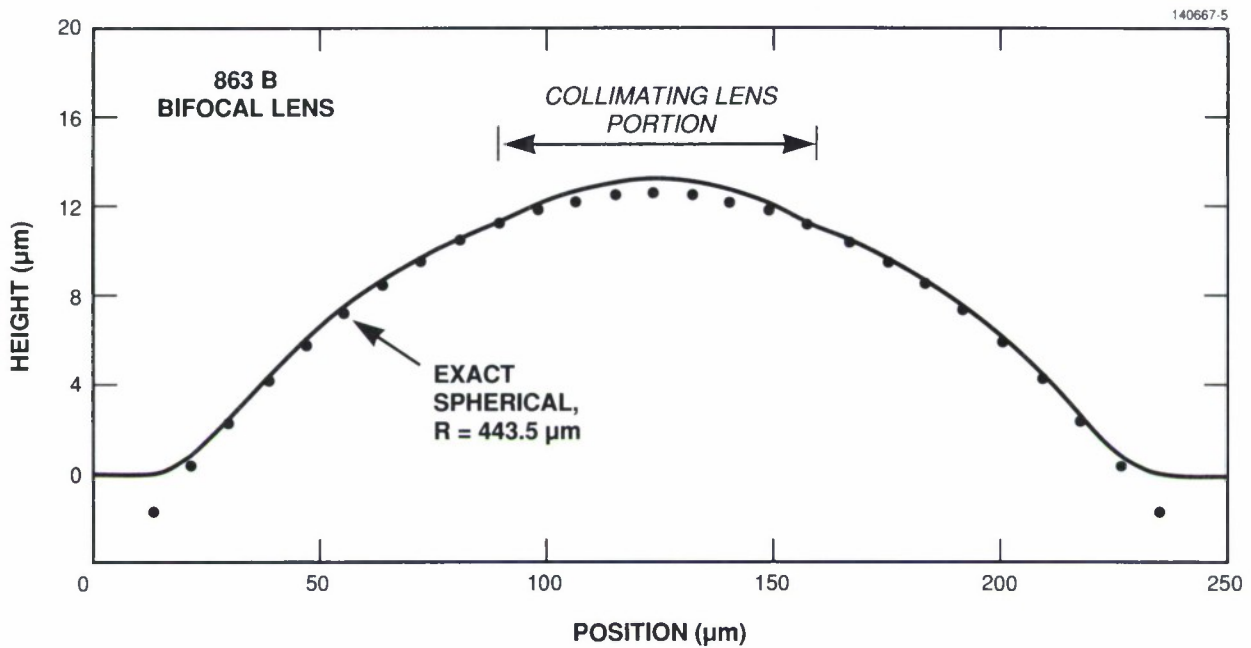


Figure 1-5. Stylus surface profiling of a bifocal microlens (solid trace) and a calculated exact spherical profile (dotted curve).

The  $45^\circ$  and vertical mirrors were then fabricated by chemical etching and mass transport [9]. The  $45^\circ$  mirror was made slightly parabolic to favor the coupling between the spherical mirror and the BH waveguide. After the mirror formation, the BH waveguide was formed, again by using chemical etching and mass transport [9-11]. Figure 1-6 shows micrographs of a fabricated wafer. Note that the  $45^\circ$  mirror and the BH mesa are well centered to the concentrated spot of light produced by the microlens.

The wafer was then coated with a  $0.4\text{-}\mu\text{m}$ -thick PSG layer on the BH side and a  $0.23\text{-}\mu\text{m}$ -thick (quarter wavelength)  $\text{SiO}_2$  layer on the  $n$ -side. Alloyed Au/Zn contacts were formed in the PSG openings on the BH mesas, and Au/Sn alloyed contacts were then formed in the  $\text{SiO}_2$  openings in regions outside the microlenses. The  $n$ -side was subsequently coated by a Ti/Au evaporation, except the collimating lens portion, where the  $\text{SiO}_2$  layer was retained as an antireflection coating (see Figure 1-3). The BH side was then sputtered with Ti/Pt/Au and the wafer was saw-cut to yield individual devices.

The devices were tested junction-side down under room-temperature pulsed operation. The light output vs current characteristic of a device with 92-mA threshold current is shown in Figure 1-7(a). The lowest threshold obtained was 70 mA. Although very low threshold current has not been achieved in the present work, we believe this is not owing to fundamental limitations. Threshold and power approaching those of the conventional devices should be achievable with further development of microlens and mirror fabrication technologies and improved integration skills (front-and-back wafer handling, and precision alignment and etching).



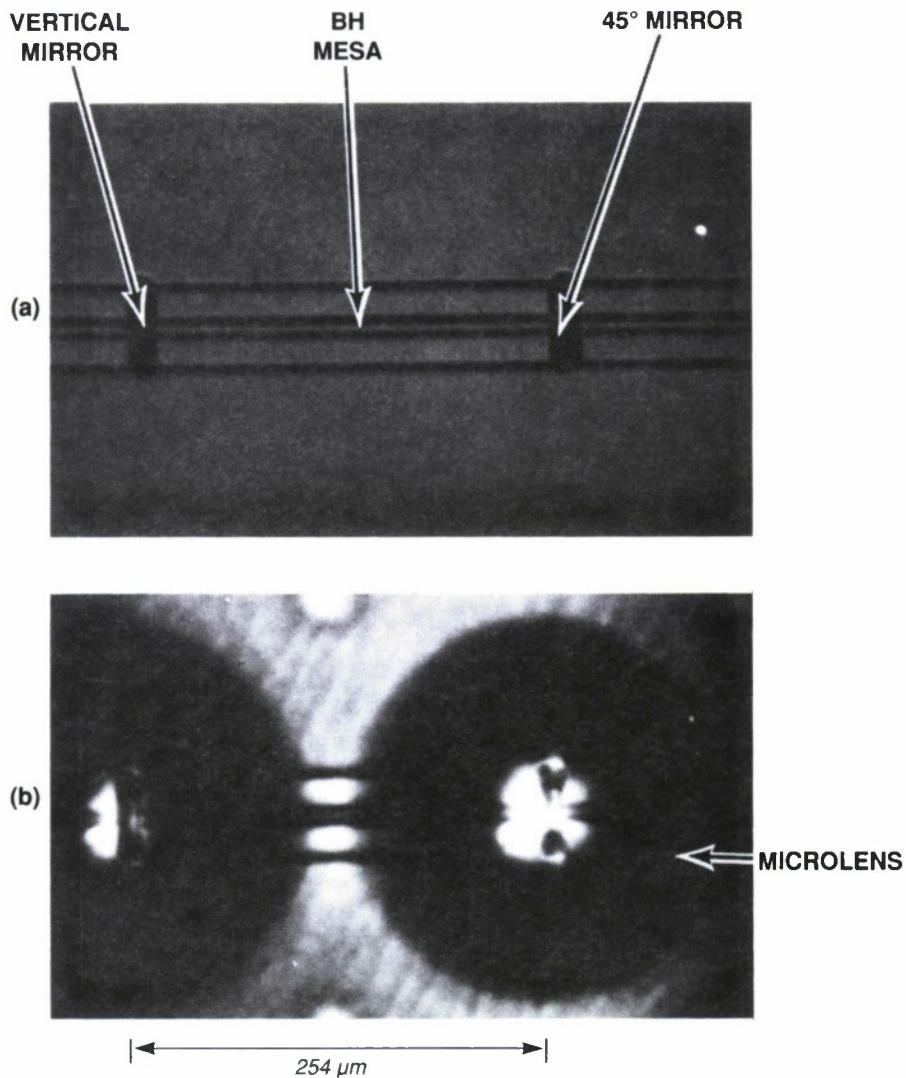


*Figure 1-6. Micrographs of an integrated lens-laser structure (before metallization) obtained by (a) reflected visible light and (b) transmitted infrared. The underlying microlenses and the concentrated spots of light they produce are clearly seen in the infrared micrograph.*

Narrow beam divergence has been observed as shown in the far-field scan in Figure 1-7(b). The measured full width at half-maximum of the central lobe is  $1.25^\circ$  and is close to the diffraction-limited beam divergence of a  $70\text{-}\mu\text{m}$ -diam. aperture [12]. The sidelobes resemble diffraction rings but with higher intensities and some irregularities. This could be a result of possible morphological defects observed on some microlenses (caused by insufficient wafer protection during mass transport), a possible small deviation from the ideal lens profile, or a slightly off-centered detector in the far-field scan.



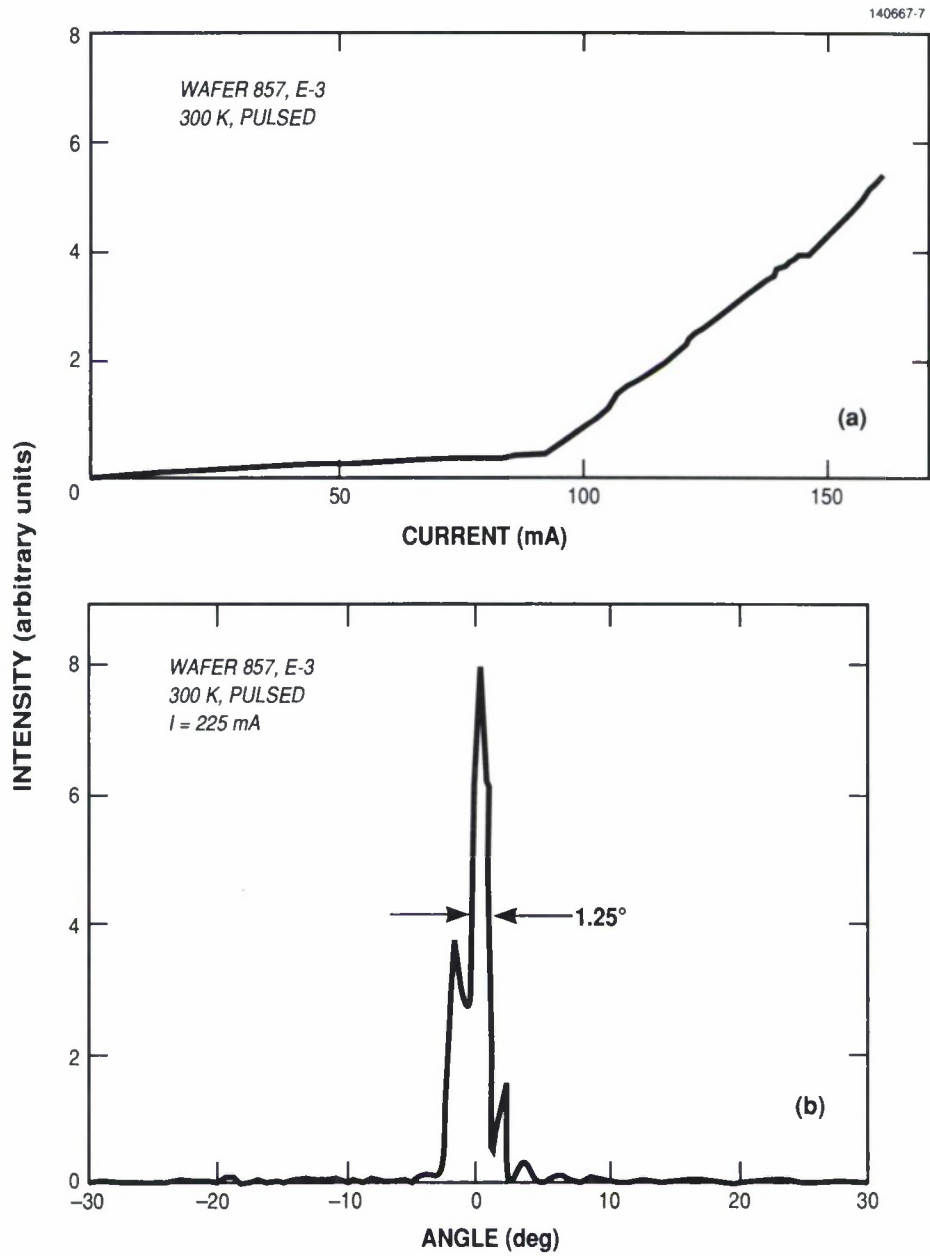


Figure 1-7. (a) Light output vs current characteristic and (b) far-field pattern of a monolithic lens-laser.

In conclusion, monolithic integration of a microlens with a diode laser has been demonstrated. A bifocal microlens has been proposed and fabricated, which is ideally suited for the present application. A technique has been developed to achieve accurate alignment between the microlens and the small region of gain. Further perfection of the fabrication technologies is needed to achieve threshold and power performance approaching those of the conventional diode lasers.

Z.L. Liao	L.J. Missaggia
J.N. Walpole	D.E. Mull

## REFERENCES

1. K-W. Wang, Appl. Phys. Lett. **51**, 2127 (1987).
2. J. Lindhard, M. Scharff, and H.E. Schiøtt, Mat.-Fys. Medd. Dan. Vid. Selsk. **33**, 1 (1963).
3. J.P. Donnelly and C.E. Hurwitz, Appl. Phys. Lett. **31**, 418 (1977).
4. J.D. Woodhouse, M.C. Gaidis, J.P. Donnelly, and C.A. Armiento, Appl. Phys. Lett. **51**, 186 (1987).
5. M.C. Gaidis, S.M. thesis, Massachusetts Institute of Technology, 1989.
6. J.D. Woodhouse, J.P. Donnelly, P.M. Nithishin, E.B. Owens, and J.L. Ryan, Solid-State Electron. **27**, 677 (1984).
7. P.N. Favenne, L. Henry, M. Salvi, A.M. Huber, and G. Morillot, Solid-State Electron. **26**, 771 (1983).
8. Z.L. Liao, V. Diadiuk, J.N. Walpole, and D.E. Mull, Appl. Phys. Lett. **52**, 1859 (1988); Appl. Phys. Lett. **55**, 97 (1989).
9. Z.L. Liao and J.N. Walpole, Appl. Phys. Lett. **46**, 115 (1985).
10. J.N. Walpole and Z.L. Liao, Appl. Phys. Lett. **48**, 1636 (1986).
11. Z.L. Liao and J.N. Walpole, Appl. Phys. Lett. **50**, 528 (1987).
12. See, for example, M. Born and E. Wolf, *Principles of Optics*, 5th edition (Pergamon, London, 1959), Chapter 8.

## 2. QUANTUM ELECTRONICS

### 2.1 STARTING DYNAMICS OF A PASSIVELY MODE-LOCKED Ti:Al<sub>2</sub>O<sub>3</sub> LASER

With the discovery of mode locking using an optical fiber in a coupled cavity [1-4], a new class of easily controlled, tunable, femtosecond-pulse lasers may be realized. A problem in the development of such devices, however, is the need to actively mode lock the laser to initiate passively mode-locked operation [1,2]. The Ti:Al<sub>2</sub>O<sub>3</sub> laser with self-starting mode locking [4] simplifies the fabrication of coupled-cavity mode-locked lasers by eliminating the need for active mode locking, which has the beneficial effect of improving stability.

We have studied the dynamics of self-starting to understand how a laser with an extremely weak nonlinearity becomes passively mode locked. Our observations show that mode-locked pulses form by successive narrowing of the mode-beating modulation in CW operation with a constant pulse-shortening rate. Despite the fact that the self-phase modulation in the fiber brings about a phase shift of  $10^{-3}$  rad, the transition from continuous to mode-locked operation occurs in only 230  $\mu$ s. The self-starting dynamics depends upon the phase of the feedback from the coupled cavity with distinct regimes observed for continuous, self-starting mode-locked, and sustained mode-locked operation.

The passively mode-locked Ti:Al<sub>2</sub>O<sub>3</sub> laser is shown in Figure 2-1. When pumped by an argon-ion laser at 5.4 W, the Ti:Al<sub>2</sub>O<sub>3</sub> laser with a 15-cm optical fiber produces chirped pulses of 1.4- to 3-ps duration with an average power of 300 mW at a repetition rate of 80 MHz. By using an external grating pair for dispersive compensation of the chirp, 200-fs pulses are obtained. To evaluate the self-starting dynamics, the beam in the external cavity is mechanically chopped while the output and the second-harmonic signal are monitored with photodiodes. The length of the coupled cavity is selected to produce the shortest starting time.

Shown in Figure 2-2 are the output power monitored with a slow photodiode (1- $\mu$ s rise time), the output power monitored with a fast photodiode (1-ns rise time), and the second-harmonic signal. The slow photodiode trace [Figure 2-2(a)] demonstrates that after a transient of  $\sim 40$   $\mu$ s associated with the opening of the coupled cavity, the average output power is constant. The constant average output indicates that Q-switching of the laser by opening the coupled cavity is not important for self-starting. Another implication of the constant average power is that the energy in a single pulse,  $\tau I$ , where  $\tau$  is the pulse duration and  $I$  is the peak intensity, is fixed. Thus, the peak intensity is inversely proportional to the pulse duration.

The fast photodiode trace [Figure 2-2(b)] indicates that the pulses shorten until the 1-ns limit imposed by the rise time of the detector is reached after 220  $\mu$ s. Allowing for the finite bandwidth, we find that the pulse duration decreases from 6 to 1 ns with a constant pulse-shortening rate of 0.3 ps per round-trip.

Between 220 and 230  $\mu$ s after the coupled cavity is opened, the second-harmonic signal [Figure 2-2(c)] rises rapidly to a steady-state value, indicating that picosecond pulses have formed. The

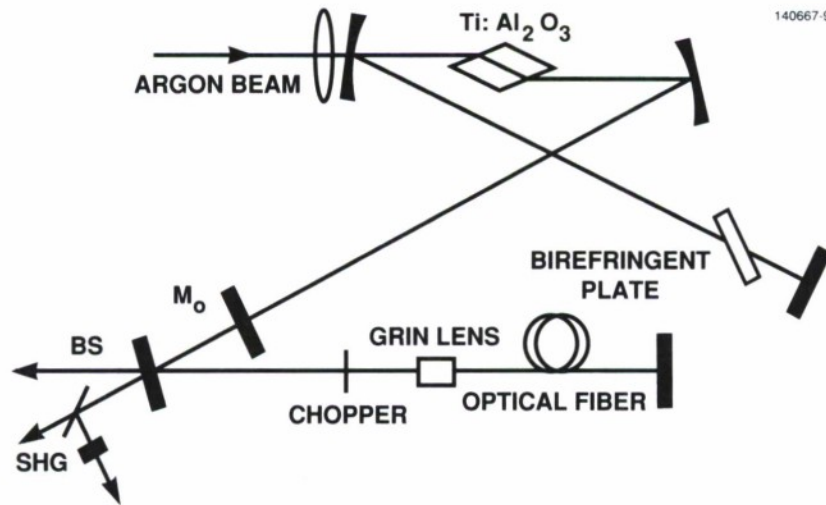


Figure 2-1. Schematic of the passively mode-locked  $\text{Ti:Al}_2\text{O}_3$  laser. The main laser cavity is astigmatically compensated and contains only the gain medium and a birefringent tuning plate. The coupled cavity begins at output coupler  $M_0$  and terminates at the mirror butt-coupled to the optical fiber. To study the self-starting dynamics, the coupled cavity is opened with a chopper while the output power and second-harmonic signal are monitored. BS, beam splitter; GRIN, graded index; SHG, second-harmonic generator.

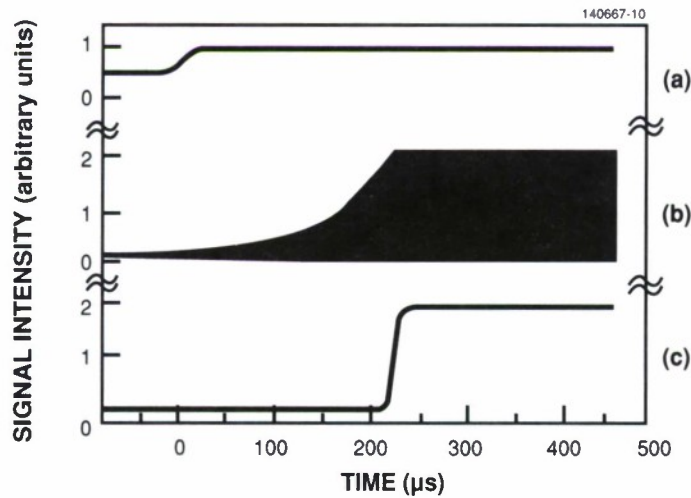


Figure 2-2. Signals from  $\text{Ti:Al}_2\text{O}_3$  laser showing start-up of passive mode locking. Output power monitored with (a) a slow photodiode and (b) a fast photodiode, and (c) the second-harmonic signal monitored with a slow photodiode.

signal is proportional to  $\tau I^2$  and is also inversely proportional to pulse duration, since the energy in the pulse,  $\tau I$ , is constant. The transition time of 10  $\mu\text{s}$  for the second-harmonic signal to rise from baseline (50 ps) to steady state (2 ps) implies a pulse-shortening rate consistent with that seen in Figure 2-2(b).

These results confirm that passive mode locking starts from mode beating of the laser. The main cavity alone showed strong sinusoidal mode beating with 50-percent modulation and a 4-ns period. With the coupled cavity open but at power levels where the mode locking did not self-start, the mode-beating modulation increased to 80 percent with a 12.5-ns period equal to the round-trip time in the cavity. At higher power levels, pulses evolved from this mode-beating modulation into the self-starting mode-locked operation.

Figure 2-3 shows the second-harmonic signal for a scan of one-half wavelength (400 nm) of the coupled cavity. The operating state of the laser depends on the phase difference between the main laser cavity and the coupled cavity and on the direction of the scanning. For a range of phase the laser is bistable, and mode-locked operation can be sustained but self-starting does not occur. In the self-starting region the laser is mode locked while scanning in either the forward or backward direction. When this

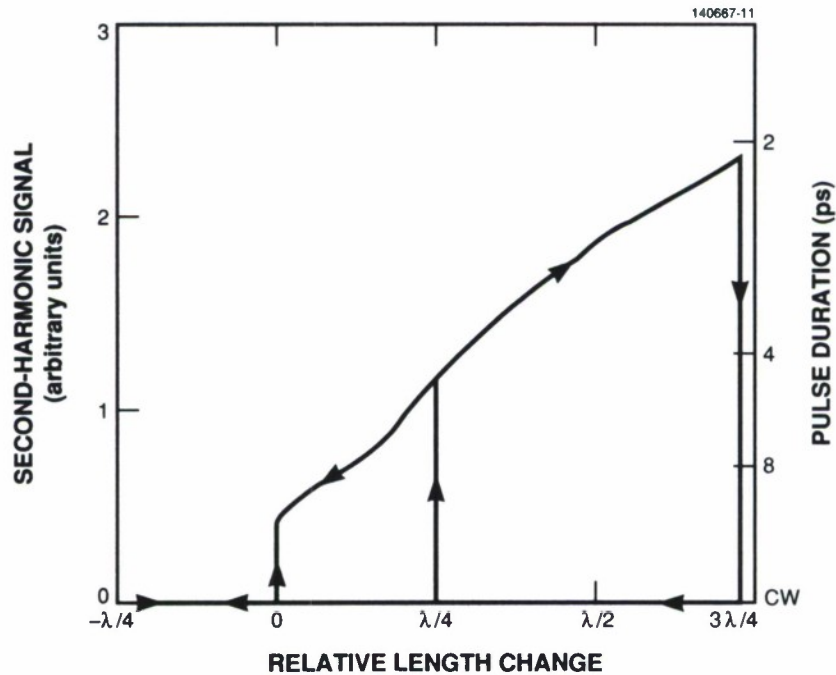


Figure 2-3. Second-harmonic signal and pulse duration as a function of the change in length of the external cavity. Lack of a second-harmonic signal indicates continuous operation; generation of a second-harmonic signal while scanning in either the forward or backward direction indicates self-starting mode-locked operation; bistability indicates sustained mode-locked operation.



region extends over a wide range of phases the laser has good stability, although pulses are longer than in the region of sustained mode locking. In the region of continuous operation the effect of the coupled cavity is to increase the pulse width, so mode locking cannot be sustained.

The self-starting range and pulse stability are significantly affected by laser power, fiber length, fiber dispersion, and gain bandwidth. As expected, the self-starting range decreases with low power in the fiber, resulting in less stable operation. To achieve a wider self-starting range at low power, the use of fibers longer than 20 cm has been attempted. However, this results in system instabilities or double pulsing caused by excessive nonlinear phase modulation. To stabilize the system the gain bandwidth must be restricted, such as by use of two- or three-plate birefringent filters. Dispersion in the fibers is important because of the different group and phase velocities, both of which are critical in the passively mode-locked operation of the laser.

These results on self-starting dynamics in a  $\text{Ti:Al}_2\text{O}_3$  laser suggest approaches for realizing passive mode locking in other systems, such as the Nd:YAG laser, where pulses of 10 ps may be possible.

J. Goodberlet\*

J.G. Fujimoto\*

J. Wang\*

P.A. Schulz

## 2.2 FREQUENCY-CHIRPED Nd:YAG LASER

A Nd:YAG laser with a fast, linear frequency chirp has been built for use in a frequency-chirped radar. The advantage of frequency chirping is that bandwidth-limited range resolution can be achieved with long pulses having low peak intensity, and thus potential optical damage can be avoided. In addition, ambiguities associated with the range and Doppler shift of the target can be minimized.

The laser operating at  $1.06\ \mu\text{m}$  consisted of a Nd:YAG crystal, a Brewster-cut MgO-doped  $\text{LiNbO}_3$  crystal, and an end mirror (see Figure 2-4). The cavity was formed by a high-reflectivity coating on one end of the Nd:YAG crystal and the 10-percent transmitting end mirror. The pump source was a  $\text{Ti:Al}_2\text{O}_3$  laser tuned to 808 nm. The frequency chirp was obtained by applying a voltage ramp across the  $\text{LiNbO}_3$ .

The laser was operated single frequency at 20 percent above threshold; at higher powers a second mode was observed. At an input power of 30 mW the output power was 0.8 mW. The laser ran single frequency up to 20 percent above threshold because the absorption length (2 mm) of the Nd:YAG crystal was very short. Other longitudinal modes, which could take advantage of the excess gain between spatial hole burning regions, occur far enough from the peak of the  $\text{Nd}^{3+}$  profile that they have significantly lower gain. During multimode operation, the modes were separated by multiples of 8 GHz. The 8-GHz spacing was consistent with etaloning caused by the end surfaces of the Nd:YAG crystal.

To provide the required radar waveform, a series of ten 140-ns-long sawtooth voltage pulses were applied to the  $\text{LiNbO}_3$  crystal. A function generator formed each sawtooth pulse with 20 voltage steps; the pulses were then amplified by 50 dB using a 25-W linear RF amplifier (250 kHz to 150 MHz). This

---

\* MIT Department of Electrical Engineering and Computer Science and Research Laboratory of Electronics.

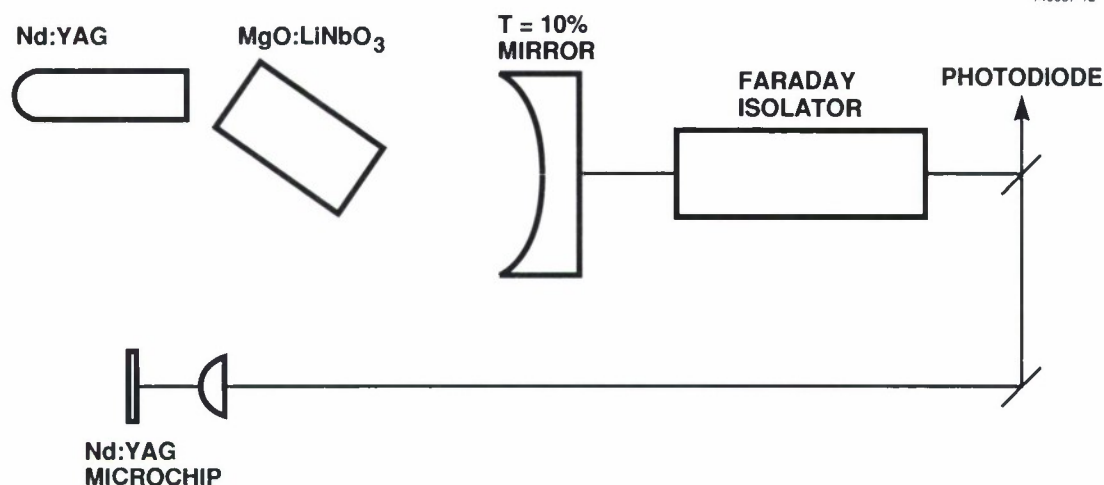


Figure 2-4. Schematic of the frequency-chirped Nd:YAG laser. The Nd:YAG laser consists of a Nd:YAG rod with a high-reflectivity mirror coated on one end, a Brewster-cut LiNbO<sub>3</sub> crystal acting as an electrooptic phase modulator, and an end mirror ( $R = 7.5$  cm) with 10-percent transmission. The voltage applied across the LiNbO<sub>3</sub> is produced by a function generator and a 25-W RF amplifier. The laser output is heterodyned against the single-frequency output of a microchip laser.

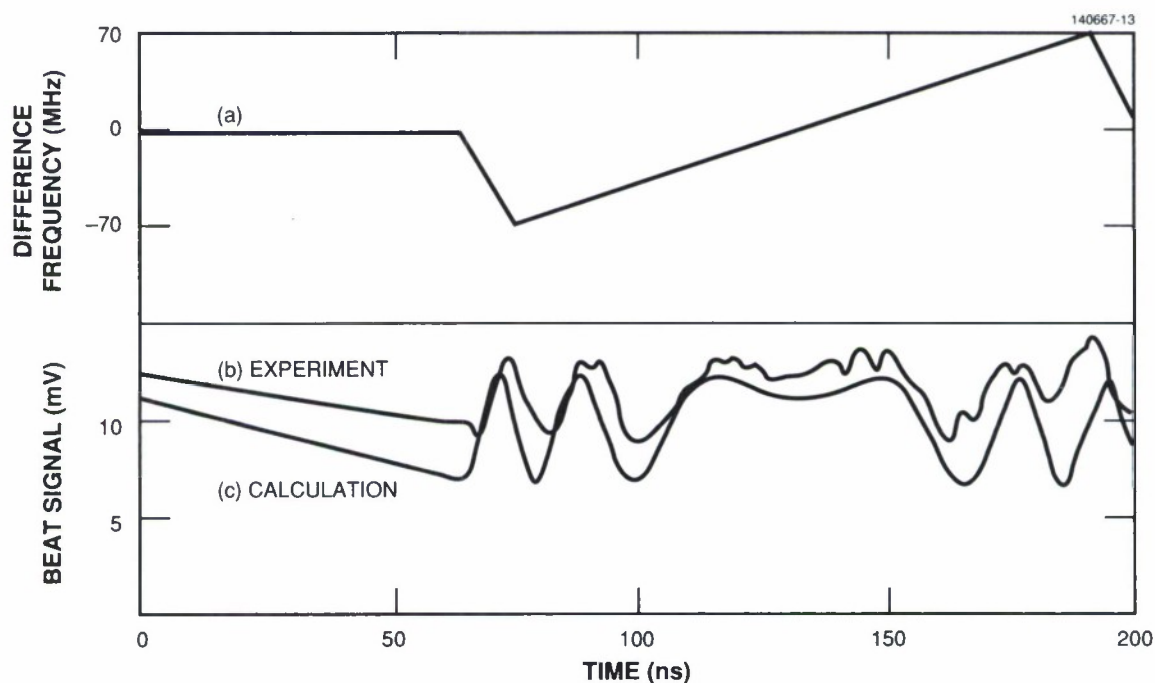


Figure 2-5. (a) Output of the function generator. This RF signal is amplified by 50 dB and applied to the electrooptic phase modulator. The laser output frequency should be linearly related to the applied voltage. (b) Heterodyne signal between the frequency-chirped laser and the stable laser. (c) Computer-calculated heterodyne signal for an initial frequency difference of 4 MHz, frequency chirp of 140 MHz, and chirp time of 120 ns. The calculated and measured waveforms are in good agreement; the discrepancies arise from pickup.

amplifier worked well for the 7-MHz repetition rate sawtooth waveform, but showed appreciable non-linearity for waveforms that had frequency components below 4 MHz. A linearity of 1 percent is required to suppress the range sidelobes by 30 dB.

Figure 2-5 shows a heterodyne beat note between the chirped laser and a single-frequency microchip laser. On the assumption that the measured dc response of the electrooptic tuner is equal to its high-frequency response (as expected in  $\text{LiNbO}_3$ ), the applied voltage has been converted to frequency (see Figure 2-5). The heterodyne beat note is compared with the calculated beat note assuming a 140-MHz chirp. The good agreement between experiment and calculation indicates that the frequency chirp occurs in 120 ns with a 20-ns reset time. This frequency-chirped Nd:YAG laser should be a useful source for a frequency-chirped laser radar at 1.06  $\mu\text{m}$ .

S.R. Henion  
P.A. Schulz

### 2.3 SUM-FREQUENCY GENERATION OF SODIUM-RESONANCE RADIATION

Development has been completed of a solid state source of long-pulse-length, sodium-resonance radiation. This radiation was generated by sum-frequency mixing the output of a 1.064- $\mu\text{m}$  Nd:YAG laser with the output of a 1.319- $\mu\text{m}$  Nd:YAG laser. Each laser was operated at 10-Hz repetition rate and with a pulse length of about 100  $\mu\text{s}$ . By operating these lasers at wavelengths very close to the peak of their tuning curves, it was possible to match the wavelength of the sum-frequency radiation to that of the sodium  $D_2$  absorption wavelength [5].

The most important consideration involved in the efficient sum-frequency mixing of long-pulse Nd:YAG laser radiation is the attainment of high laser intensities in the nonlinear crystal. Because the laser pulse lengths are so long, the average power per pulse is relatively low (1 J/100  $\mu\text{s}$  = 10 kW). Simultaneous mode locking of both laser oscillators can increase the peak powers. In addition, substantial focusing of the laser radiation will raise the peak intensities to levels consistent with efficient sum-frequency mixing. As a result of the focusing of laser radiation, the nonlinear crystal is subject to both high peak intensities and very high fluences. Lithium iodate is the only crystal we have yet found that can sustain these high intensities and fluences and generate sum radiation with high conversion efficiencies.\* Unfortunately, lithium iodate has a very narrow acceptance angle for mixing. This narrow acceptance angle along with the need for substantial focusing of the input radiation requires that the Nd:YAG

---

\* A new crystal, lithium triborate (LBO), is presently being investigated. This crystal has a very large angular acceptance and a large temperature acceptance (several degrees Celsius) and is *reputed* to have a very high damage threshold. Moreover, this crystal can be temperature tuned and *noncritically* phase matched for sum-frequency mixing of 1.06- and 1.32- $\mu\text{m}$  radiation.



laser radiation have near-diffraction-limited beam quality. As a result we operated the laser oscillators in the  $TEM_{00}$  spatial mode.\*

Both the 1.06- and 1.32- $\mu\text{m}$  Nd:YAG lasers were configured as master oscillators followed by power amplifiers (Figure 2-6). Each 1.5-m-long oscillator consisted of a 40-percent output coupler, a flash-lamp-pumped Nd:YAG rod, a beam expanding telescope (for greater mode filling of the Nd:YAG rod), a dielectric polarizer, a 0.5-cm-long antireflection-coated lithium iodate crystal, an acoustooptic mode locker, and a high reflector with a 7-m radius of curvature. An intracavity aperture restricted laser oscillation to the  $TEM_{00}$  cavity mode for both Nd:YAG lasers. The lithium iodate crystals served to suppress laser spiking through intracavity second-harmonic generation [6]. The 1.32- $\mu\text{m}$  laser cavity contained a dichroic mirror (transmission at 1.32  $\mu\text{m}$  and reflection at 1.06  $\mu\text{m}$ ) for the suppression of 1.06- $\mu\text{m}$  parasitic laser oscillation. The 1.06- $\mu\text{m}$  oscillator produced 160 mJ/macropulse at 10 Hz and the 1.32- $\mu\text{m}$  oscillator produced 110 mJ/macropulse at 10 Hz synchronously with the 1.06- $\mu\text{m}$  macropulses. Each macropulse was 100  $\mu\text{s}$  long and consisted of a train of mode-locked micropulses 0.5 to 1.0 ns long and spaced at intervals of 10 ns. The acoustooptic mode lockers were driven by a single-frequency source so that the mode-locked laser micropulses would be phase locked. The relative phase of the mode-locker drive signals was adjusted so that the micropulses from the 1.06- and 1.32- $\mu\text{m}$  lasers overlapped in time at the sum-frequency mixing crystal.

The output of the 1.06- $\mu\text{m}$  laser oscillator passed through a Pockels cell for the elimination of the first, and only, relaxation oscillation on the laser pulse. (We have found that the temporal overlap of the initial relaxation oscillation from either Nd:YAG laser with any part of the other laser pulse is very likely to result in damage to the sum-frequency mixing crystal.) The 1.06- $\mu\text{m}$  radiation passed through a beam expander and then through a Nd:YAG amplifier, and after amplification had an energy of 1 J. The output of the 1.32- $\mu\text{m}$  laser oscillator was amplified in a two-stage amplifier. The 1.32- $\mu\text{m}$  radiation passed directly into a beam expander and was then double-passed through the first-stage Nd:YAG amplifier. This radiation was then passed through a 90° polarization-rotator quartz crystal in order to compensate the thermally induced birefringence in the two amplification passes. The laser beam was then reexpanded and double-passed through the second-stage Nd:YAG amplifier. The first-stage amplifier was operated near the small-signal limit and resulted in a gain of about 4 while the second stage was operated nearer to saturation and resulted in a gain of only 2.

After amplification the 1.32- $\mu\text{m}$  laser radiation had an energy of 0.8 J. Since the 1.32- $\mu\text{m}$  laser pulse had an initial relaxation oscillation, this pulse was timed to slightly precede the 1.06- $\mu\text{m}$  pulse so that the 1.32- $\mu\text{m}$  relaxation oscillation did not overlap in time with any 1.06- $\mu\text{m}$  radiation.

---

\* It should be possible to obtain greater diffraction-limited energy from the oscillators by configuring them as unstable resonators with mirrors that have a Gaussian reflectivity profile in the radial direction.

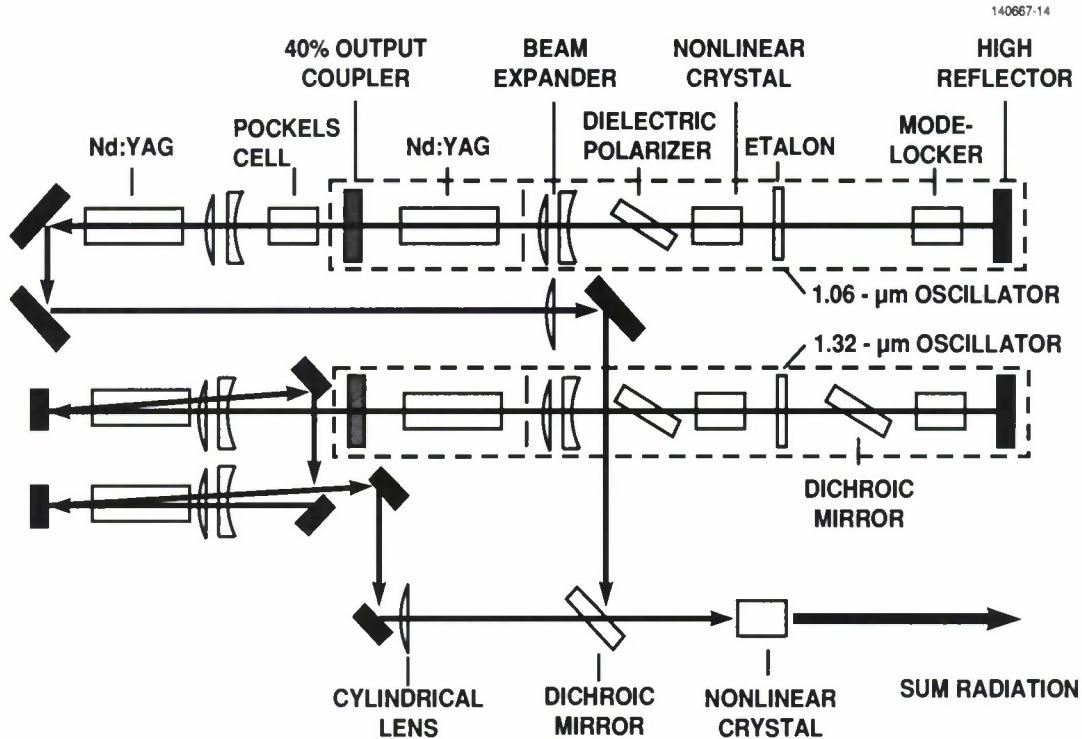


*Figure 2-6. Nd:YAG laser system for long-pulse-length, sum-frequency generation of sodium-resonance radiation.*

The 1.06- and 1.32-μm radiation were each passed through 0.5-m cylindrical lenses prior to being combined on a common beam path by the dichroic mirror. The cylindrical lenses focused the beams in the dimension to which the nonlinear crystal is least angularly sensitive. This was done in order to keep the infrared energy within the phase-matching acceptance angle. By focusing 1.0 J of 1.06-μm radiation and 0.8 J of 1.32-μm radiation into an area  $3 \times 10^{-3} \text{ cm}^2$  in a 2-cm-long lithium iodate crystal, we have generated as much as 0.5 J of sodium-resonance radiation.

T.H. Jeys  
T.C. Hotaling  
J. Korn



## 2.4 PUMP SOURCE REQUIREMENTS FOR END-PUMPED LASERS

Relationships between the properties of the pump beam and the gain medium in end-pumped lasers have been derived. A novel scheme for power scaling of end-pumped lasers using multiple sources is described in terms of these relationships. End-pumped lasers offer the advantages of high efficiency and good beam quality over side-pumped lasers. However, it has been argued that scaling the output power from these devices is limited because only a few sources can be focused into the fundamental mode of the laser. Some techniques that have been used to increase the number of pump sources in end-pumping include polarization coupling, fiber bundles [7], and multiple ends [8,9]. Each of these has limitations. As an alternative, we have demonstrated and analyzed a technique that uses multiple sources based on geometric multiplexing [10]. This technique is compatible with the other techniques for additional scaling. Here we present the results of an analysis for matching a pump source to an end-pumped laser and a description of geometric multiplexed pump sources based on these results.

For an efficient, fundamental transverse mode, end-pumped laser, two conditions must be satisfied. The gain medium must be long enough to absorb a large fraction of the pump light, and the pump radiation must be focused inside the cross section of the fundamental mode over this length as shown in Figure 2-7. The bow-tie region in the figure represents the pump beam. The fundamental mode is assumed to have a constant beam radius  $\omega_0$  in the gain medium and defines a cylindrical volume into which the pump light must be focused. With the above geometric constraint, using conservation of radiance of the pump beam, and for optimum focusing of the pump beam into the gain medium, we have derived approximate relationships between the pump beam properties and the pump intensity and unsaturated single-pass gain that can be attained.

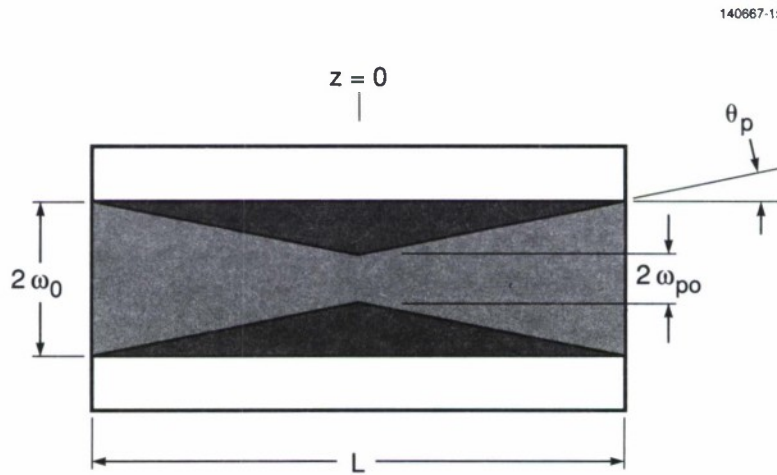


Figure 2-7. Schematic of the fundamental mode with radius  $\omega_0$  and the pump beam with waist  $\omega_{po}$  and far-field diffraction angle  $\theta_p$  in the gain medium.

Conservation of radiance implies that the product of the pump beam waist and the far-field divergence is a quantity that is characteristic of the pump beam and must be conserved through optical transformation. The radiance or brightness  $B$  is defined as

$$B = P / (\pi \omega_{po} \theta_p)^2 , \quad (2-1)$$

where  $P$  is the pump power and  $\omega_{po}$  and  $\theta_p$  are the pump beam radius and far-field divergence angle as shown in Figure 2-7. The optimum focusing condition gives the best trade-off between  $\omega_{po}$  and  $\theta_p$  to achieve the maximum pump intensity over the gain medium length. The result is summarized by the following basic equation in which the equality corresponds to the optimum focusing condition:

$$I \leq n(BP)^{1/2} / 2L , \quad (2-2)$$

where  $I$  is the pump intensity incident at the gain medium,  $n$  is the refractive index of the gain medium, and  $L$  is the gain medium length (chosen to be on the order of one absorption length). The pump intensity is directly related to the resulting unsaturated single-pass gain  $\Gamma$  of the pumped laser. For an ideal four-level laser

$$\Gamma = \left( \frac{I}{I_s} \right) \left( \frac{\lambda_p}{\lambda_L} \right) , \quad (2-3)$$

where  $I_s$  is the saturation intensity for the laser transition and  $\lambda_p / \lambda_L$  is the ratio between the pump and lasing wavelengths.

Equation (2-2) can be used to analyze a novel scheme for end-pumped solid state lasers by geometric multiplexing of multiple diode lasers. Figure 2-8 shows a pump source composed of seven individual sources each of which is collimated by a lens. The brightness of this pump beam as a whole

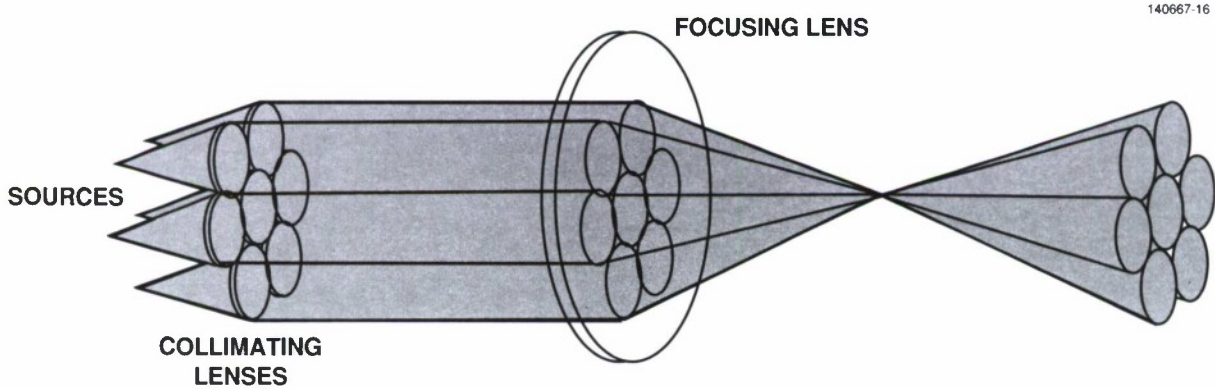


Figure 2-8. Schematic of a pump source consisting of seven individual sources, each of which is collimated by a lens.

is the same as the brightness of a beamlet from a single source with its collimating lens, which in turn is determined by the power, size, and far-field diffraction angle of the individual source. The brightness is constant because as more sources are added, neither the intensity nor the far-field diffraction angle of the pump beam as a whole changes. Thus, in terms of Equation (2-2), one can obtain for this case  $7^{1/2}$  times higher pump intensity and 7 times higher power from the pump beam as a whole compared with a single source. As even more sources are added the pump power and intensity increase further. Geometric multiplexing should be useful in building high-power and high-energy lasers operating in a fundamental transverse mode using two-dimensional arrays of diodes collimated with two-dimensional arrays of lenslets.

In summary, equations that relate the pump beam properties and the gain medium properties in end-pumped, fundamental transverse mode lasers have been derived. These equations are useful in the analysis of geometrically multiplexed, multiple diode laser pumped lasers.

T.Y. Fan  
A. Sanchez

## 2.5 LIMITS IMPOSED BY SPATIAL HOLE BURNING ON THE SINGLE-MODE OPERATION OF MICROCHIP LASERS

Spatial hole burning imposes an upper limit on the power level at which microchip lasers [11] will operate in a single longitudinal mode. Let us assume that the microchip laser contains a homogeneously broadened gain medium of length  $\ell$ . If the round-trip loss, and therefore the round-trip gain, of the cavity are relatively low, a well-defined standing-wave intensity pattern will develop. (For cavities with a large round-trip loss the intensity of the modes would not oscillate as strongly in space, and the effects of spatial hole burning would be reduced. This would allow single-mode operation at higher power levels than indicated by the following equations.) If a plane-wave approximation is made for the transverse mode profile, the intensity of mode  $m$  within the microchip laser can be written as

$$I_m(z) = 4I_m \sin^2(2\pi z / \lambda_m) , \quad (2-4)$$

where  $I_m$  is the intensity of the beam traveling in one direction within the laser cavity,  $\lambda_m$  is the wavelength and  $z$  is the dimension along the cavity axis. The laser cavity is located between  $z = 0$  and  $z = \ell$ . Assuming that spatial cross-relaxation of the inverted population is slow compared with the stimulated relaxation of the inversion density, we can write the CW rate equations for each of the oscillating modes as

$$\sigma_m \int_0^\ell N(z) I_m(z) dz = \gamma_m I_m , \quad (2-5)$$

and for the inversion density  $N(z)$

$$P(z) = \sum_m \sigma_m N(z) I_m(z) / \hbar \omega_m + N(z) / \tau_{\text{eff}} , \quad (2-6)$$

where  $P(z)$  is the pump rate,  $\sigma_m$  is the value of the emission cross section at the frequency corresponding to mode  $m$ ,  $\gamma_m$  is the total round-trip loss for mode  $m$  (including transmission through the cavity mirrors),  $\omega_m$  is the lasing frequency of mode  $m$ , and  $\tau_{\text{eff}}$  is the relaxation time for the inversion density in the absence of stimulated emission. Spatial cross-relaxation, if included, would tend to wash out the spatial holes in the inversion density, and would lead to single-mode operation at higher power levels than indicated by the results obtained below.

We can immediately solve for the inversion density  $N(z)$ . For single-mode operation

$$N(z) = \frac{N_0(z)}{1 + I_1(z) / I_{\text{sat},1}} , \quad (2-7)$$

where  $N_0(z)$  is the inversion in the absence of saturation and is proportional to the local pump rate,  $I_1(z)$  is the intensity of the lasing mode, and  $I_{\text{sat},1}$  is the saturation intensity at the lasing frequency  $\omega_1$ , given as

$$I_{\text{sat},1} = \frac{\hbar \omega_1}{\sigma_1 \tau_{\text{eff}}} . \quad (2-8)$$

If we assume that  $\ell$  is much greater than  $\lambda_1$  and that  $N_0(z)$  changes much more slowly with  $z$  than  $\sin^2(2\pi z/\lambda_1)$ , both valid assumptions for microchip lasers, Equations (2-4), (2-5), and (2-7) can be combined to yield a condition for single-mode operation,

$$\langle N \rangle < \zeta(1,2) N_{\text{thresh}} , \quad (2-9)$$

where the indices 1 and 2 correspond to the first and second mode to lase,  $\langle N \rangle$  is the average inversion density,

$$\langle N \rangle \equiv \frac{1}{\ell} \int_0^\ell N_0(z) dz , \quad (2-10)$$

$N_{\text{thresh}}$  is the threshold for lasing,

$$N_{\text{thresh}} = \frac{\gamma_1}{2\sigma_1 \ell} , \quad (2-11)$$

and  $\zeta(1,2)$  is the ratio of the maximum single-mode inversion density to the threshold inversion density, and is a function of the cavity parameters, the gain cross sections at the frequencies corresponding to modes 1 and 2, and the phase relationship between modes 1 and 2

$$\zeta(1,2) \equiv \frac{\beta(1,2) - \langle \psi(1,2) \rangle}{1 - \langle \psi(1,2) \rangle} \left\{ \frac{2[\beta(1,2) - \langle \psi(1,2) \rangle]}{1 - \langle \psi(1,2) \rangle} - 1 \right\} . \quad (2-12)$$

The discrimination factor  $\beta(1,2)$  is given by

$$\beta(1,2) \equiv \frac{\sigma_1 \gamma_2}{\sigma_2 \gamma_1} , \quad (2-13)$$



and the correlation factor  $\langle \psi(1,2) \rangle$  is the weighted average value of the cosine of the phase difference between the standing-wave intensity patterns generated by modes 1 and 2. For a longitudinally pumped microchip laser

$$\langle \psi(1,2) \rangle = 1 / [1 + (2\pi\Delta m / \alpha\ell)^2] , \quad (2-14)$$

where  $\alpha$  is the absorption coefficient at the pump wavelength and  $\Delta m$  is the difference in the longitudinal mode numbers of modes 1 and 2. If we model the gain profile of the microchip laser as a Lorentzian, the discrimination factor  $\beta(1,2)$  is given by

$$\beta(1,2) = 1 + [\Delta\lambda(1,2) / \lambda_{\text{half}}]^2 , \quad (2-15)$$

where  $\lambda_{\text{half}}$  is the half-width of the Lorentzian and  $\Delta\lambda(1,2)$  is the difference in wavelength between the first mode to oscillate (mode 1) and a potential second mode (mode 2)

$$\Delta\lambda(1,2) = \Delta m \lambda_0^2 / 2n\ell , \quad (2-16)$$

in which  $\lambda_0$  is the wavelength at the gain peak, and  $n$  is the refractive index of the gain medium.

As an example, consider a Nd:YAG microchip laser operating at a wavelength of  $1.32 \mu\text{m}$ . Let one of the mirrors, the pump mirror, be highly reflecting at all potential lasing frequencies ( $R > 99.9$  percent) and highly transmitting at the pump wavelength. Let the other mirror, the output coupler, have a flat reflectivity over the gain peak at  $1.32 \mu\text{m}$  and a greatly reduced reflectivity at all other gain peaks, so that only the  $1.32\text{-}\mu\text{m}$  peak needs to be considered. At room temperature, the  $1.32\text{-}\mu\text{m}$  gain peak can be approximated as a Lorentzian with a half-width  $\lambda_{\text{half}}$  of  $0.4 \text{ nm}$ . Assume that the microchip laser is

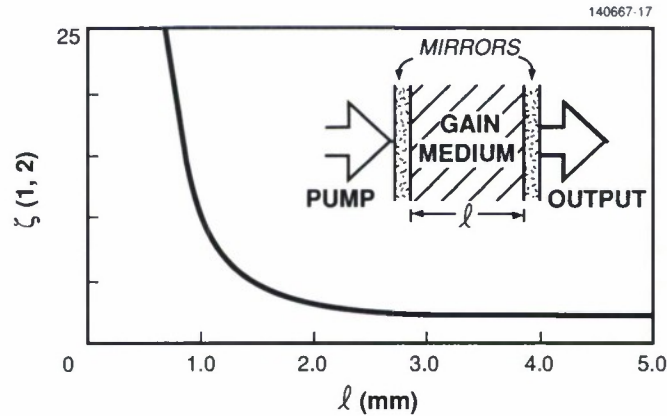


Figure 2-9. Inversion ratio  $\zeta(1,2)$  as a function of cavity length  $\ell$  for a longitudinally pumped laser cavity completely filled with Nd:YAG (see inset), operating at  $1.32 \mu\text{m}$ .



pumped with a diode laser at 808 nm, and that the Nd concentration is such that the absorption length for the pump is 1 mm. We will neglect any reflection of the pump light by the output coupler. The question we will ask is: how does the maximum single-mode power change as the cavity length is changed? To simplify the analysis we will change the cavity length discretely, such that one of the cavity modes always falls at the peak of the gain profile. This will always be the first mode to lase. The smallest value of the inversion ratio  $\zeta(1,2)$  corresponds to  $\Delta m = 1$  for all cavity lengths, and is plotted as a function of cavity length in Figure 2-9.

J.J. Zayhowski

## 2.6 THERMAL WAVEGUIDING IN MICROCHIP LASERS

In a longitudinally pumped microchip laser the planar uniformity of the cavity is broken by the pump beam, which deposits heat as it pumps the crystal. The heat diffuses outward from the pump beam, resulting in a radially symmetric temperature distribution. For materials with a positive  $dn/dT$ , such as Nd:YAG, this results in a thermal waveguide.

To study the waist size of the lasing mode in a microchip laser, a charge injection device (CID) camera was used to measure the diameter of the output beam in the far-field. The far-field beam diameter was used to calculate the divergence of the beam. Since the far-field beam profile of the microchip lasers is a circularly symmetric Gaussian, the radius of the waist,  $\omega_0$ , can be calculated from the divergence angle  $\theta$  and the optical wavelength  $\lambda$  using the formula

$$\omega_0 = \lambda / \pi \theta . \quad (2-17)$$

The microchip laser used in these experiments consisted of a circular piece of Nd:YAG, 9 mm in diameter by 0.7 mm thick. One side of the Nd:YAG (the pump side) was dielectrically coated to be highly reflecting at  $1.064 \mu\text{m}$  and to transmit the pump light. The other side (the output side) was coated to be 1-percent transmitting at  $1.064 \mu\text{m}$  and to reflect the pump light. The microchip laser was longitudinally pumped with the 808- $\mu\text{m}$  output of a Ti:Al<sub>2</sub>O<sub>3</sub> laser. The pump spot was located near the center of the Nd:YAG crystal, which was set on a glass window.

Using the procedure described above, we measured the waist size of the beam as a function of pump power. For this experiment the pump beam was tight-focused, corresponding to a pump spot of roughly  $17 \mu\text{m}$  in radius at the pump surface of the microchip laser. The experimental results are shown in Figure 2-10. The experiment was repeated for several different Nd:YAG microchip lasers with nearly identical results.

The radius of the oscillating mode in the microchip laser was also studied as a function of pump-spot radius. The pump spot was varied by changing the distance between the microchip laser and the lens used to focus the pump light. The radius of the pump in the crystal was determined from a measure of the pump radius at the waist, a measure of the pump radius in front of the focusing lens, and the focal length of the lens. The radius recorded for the experiments corresponds to the radius at the pump surface of the microchip laser. For these experiments, the total pump power was kept constant at 100 mW. The experimental results are shown in Figure 2-11.

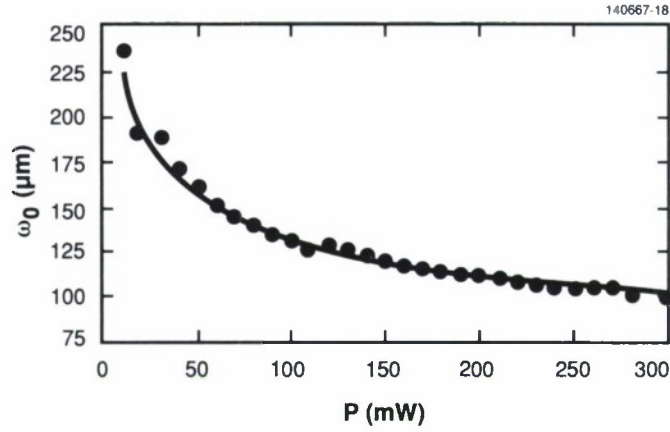


Figure 2-10. Waist size  $\omega_0$  of the  $TEM_{00}$  mode of a microchip laser as a function of incident pump power  $P$ . The circles represent experimental data. The solid curve corresponds to  $\omega_0^2 = 5986P^{-1/2} \mu m^2$ , with  $P$  in watts.

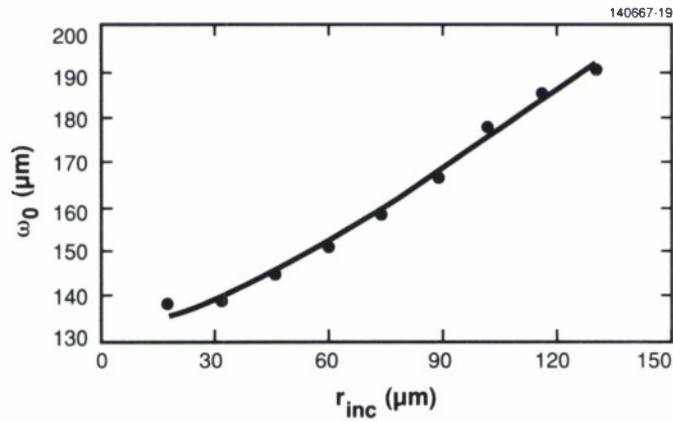


Figure 2-11. Waist size  $\omega_0$  of the  $TEM_{00}$  mode of a microchip laser as a function of the radius of the pump spot,  $r_{inc}$ . The circles represent experimental data. The solid curve corresponds to  $\omega_0^2 = 241(75^2 + r_{inc}^2)^{1/2} \mu m^2$ , with  $r_{inc}$  in micrometers.

Finally, a chopper was placed in the path of the pump beam to see if the pump duty cycle had an effect on the radius of the oscillating mode. The chopper blades were adjusted to pass the pump beam only 8 percent of the time, at a frequency of  $\sim 3$  kHz. It was observed that the waist size of the lasing mode was dependent on the average pump power incident on the microchip laser, not on the peak power. This eliminates nonlinear optical effects and gain guiding as possible factors in determining the waist size of the lasing mode, leaving only thermal waveguiding.

To better understand the experimental results, a simple model of thermal waveguiding in the microchip laser was developed. The thermal distribution caused by the longitudinal pumping of the microchip laser produces a change in refractive index of the form

$$\Delta n = \frac{dn}{dT} \Delta T, \quad (2-18)$$

where  $dn/dT$  is the linear change in refractive index with temperature, including the effects of temperature-induced stress. To solve for the thermal distribution in the microchip laser, we assume that all the heat flow in the microchip laser is directed radially away from the cavity axis, with an infinite heat sink at the edges of the crystal, and no heat sinking on either of the mirrored surfaces. The heat in the crystal is generated by the pump beam, which propagates along the axis of the laser perpendicular to the mirrored surfaces. The pump beam is assumed to be a Gaussian of constant amplitude, with an effective radius  $r_p$  centered at  $r = 0$ , depositing heat at a rate  $Q_p$  into the cavity of length  $\ell$ . With these approximations, we find that near the cavity axis the refractive index takes the form

$$n = n_0 - \frac{n_T r^2}{2}, \quad (2-19)$$

with

$$n_T = \frac{1}{k} \frac{Q_p}{\pi r_p^2 \ell} \frac{dn}{dT}, \quad (2-20)$$

where  $k$  is the thermal conductivity of the gain medium. For a material with constant  $n_0$  and  $n_T$  there is a guided Gaussian beam of constant radius  $\omega_0$ , given by

$$\omega_0^2 = \frac{\lambda}{\pi(n_0 n_T)^{1/2}}, \quad (2-21)$$

where  $\lambda$  is the optical wavelength of the beam [12]. Combining Equations (2-20) and (2-21) we have

$$\omega_0^2 = \lambda r_p \left[ \frac{\ell k}{\pi Q_p n_0 (dn/dT)} \right]^{1/2}. \quad (2-22)$$

To compare the experimental results with theory, we assume that the rate of heat generation is proportional to the incident pump power

$$Q_p = \eta P, \quad (2-23)$$

and postulate that the effective pump radius is given by

$$r_p = (r_0^2 + r_{\text{inc}}^2)^{1/2} , \quad (2-24)$$

where  $r_{\text{inc}}$  is the radius of the pump at the pump surface of the microchip laser. Using  $\eta$  and  $r_0$  as adjustable parameters we are able to obtain a good fit to the experimental data, corresponding to

$$\omega_0^2 = 77(75^2 + r_{\text{inc}}^2)^{1/2} P^{-1/2} \mu\text{m}^2 , \quad (2-25)$$

with  $P$  in watts and  $r_{\text{inc}}$  in micrometers. These fits are shown as solid curves in Figures 2-10 and 2-11. The corresponding value of  $\eta$  is smaller than the measured heat-generating efficiency of the pump, but is of the proper order of magnitude. The discrepancy, along with the large value of  $r_0$ , is most likely due to the simplifying assumptions used in the thermal modeling of the microchip laser. The fits are good enough, and the experimental results repeatable enough, however, to make Equation (2-22) a useful model for the microchip laser when the effective pump radius and the experimental values of  $\eta$  and  $r_0$  are used.

Thermal waveguiding has several important consequences in both the selection of the gain media for microchip lasers and the performance of the devices. The thermal coefficients of the gain media determine the waist size of the lasing mode. The properties of Nd:YAG are such that the diameter of the thermally guided mode is much larger than the diameter of a tightly focused pump spot. This results in an output beam with small divergence. As long as the pump spot is much smaller than the waist of the lasing mode, the transverse quality of the lasing mode will be insensitive to the shape of the pump spot. The transverse quality of the lasing mode is determined by the temperature profile of the microchip gain medium, which smooths out irregularities in the pump profile. This accounts for the good TEM<sub>00</sub> output beams that have been obtained from diode-pumped microchip lasers [13], even when the diodes were operating in several transverse modes. In designing miniature microchip laser packages, care should be taken to maintain a proper temperature profile in the gain medium.

J.J. Zayhowski  
R.C. Hancock

## 2.7 MIRROR MISALIGNMENT TOLERANCES IN MICROCHIP LASERS

To study the tolerance in mirror misalignment on Nd:YAG microchip lasers, a thermal gradient was imposed on the microchip laser by cooling one side of a 9-mm microchip wafer and heating the other side. This thermal gradient resulted in an optic wedge between the two mirrors, with a wedge angle given by

$$\psi = \left( \frac{dn}{dT} + \gamma n_0 \right) \ell \frac{dT}{dr} , \quad (2-26)$$



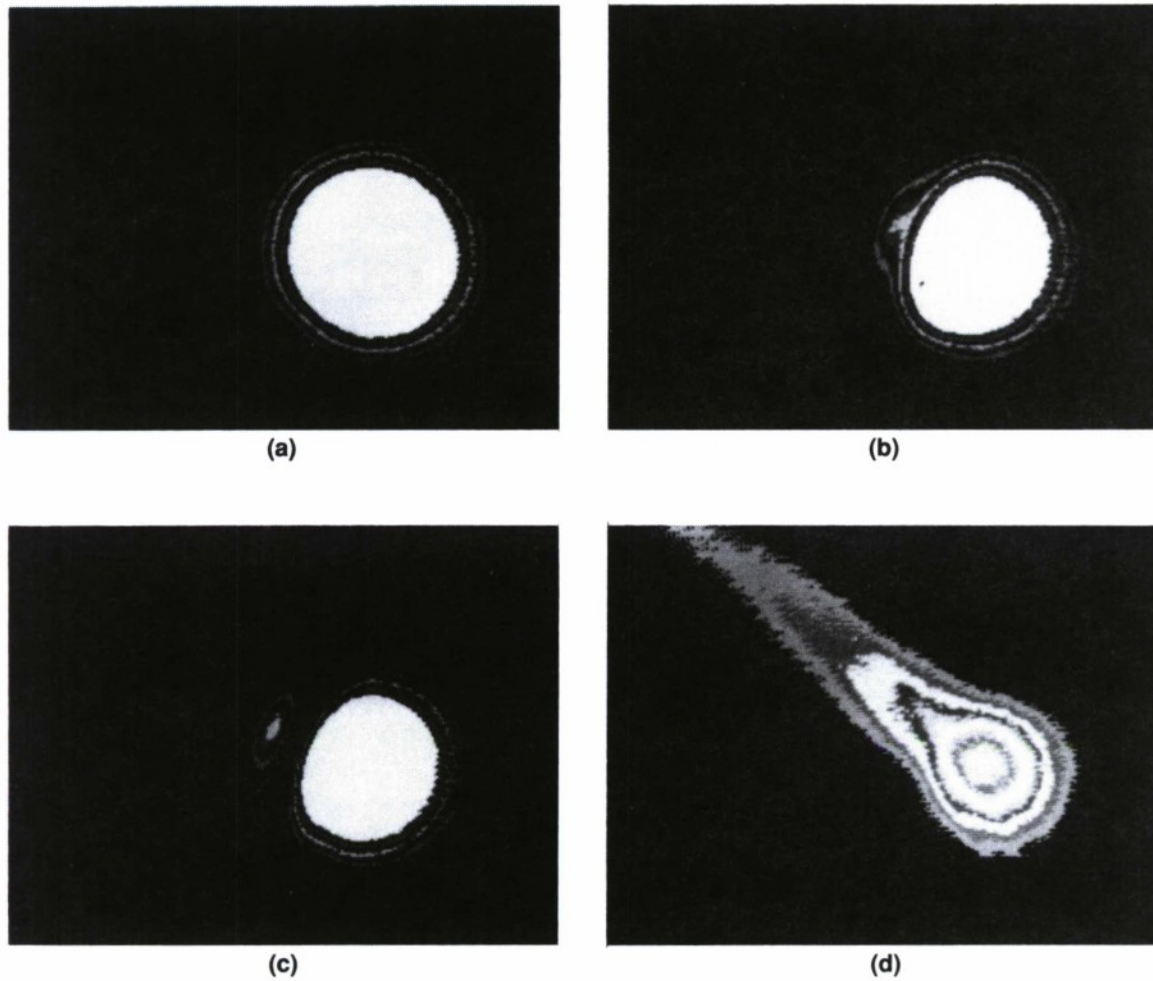


Figure 2-12. Far-field patterns of the microchip laser as a thermal gradient is applied across the microchip wafer. The pump power was 300 mW focused to a 17- $\mu\text{m}$  radius at the pump surface of the microchip laser. The magnitude of the thermally induced optical wedge is (a)  $\psi = 3.3 \times 10^{-5}$  rad, (b)  $\psi = 3.6 \times 10^{-5}$  rad, (c)  $\psi = 4.2 \times 10^{-5}$  rad, and (d)  $\psi = 9.2 \times 10^{-5}$  rad. Large white areas correspond to saturation of the CID camera.



where  $dn/dT$  is the direct temperature-induced variation of the refractive index ( $dn/dT = 9.05 \times 10^{-6} \text{ K}^{-1}$  at  $1.064 \text{ } \mu\text{m}$ ),  $\gamma$  is the thermal expansion coefficient ( $\gamma = 7 \times 10^{-6} \text{ K}^{-1}$ ),  $n_0$  is the refractive index ( $n_0 = 1.8$ ), and  $\ell$  is the length of the microchip laser. The length of the microchip laser used in these experiments was  $700 \text{ } \mu\text{m}$ . The optical wedge has the same effect as a misalignment of the cavity mirrors by the same angle, but can be more easily and more accurately controlled.

The far-field pattern of the microchip laser was observed as a function of applied thermal gradient for several pump powers. It was found that for a tightly focused pump beam, the thermal gradient at which the far-field pattern was no longer circularly symmetric was proportional to the incident pump power. The rest of the experiment described in this section corresponds to a pump power of  $300 \text{ mW}$ . The far-field pattern remained circularly symmetric up to a thermal gradient corresponding to  $\psi = 3.3 \times 10^{-5} \text{ rad}$ , as shown in Figure 2-12(a). With a slightly larger thermal gradient a small sidelobe began to develop [Figure 2-12(b)]. This lobe was located in the direction of the hot side of the crystal and had an intensity well below the intensity of the main peak. With further increase in thermal gradient, additional sidelobes appeared [Figure 2-12(c)]. The intensity of the sidelobes increased with thermal gradient, while the overall intensity of the microchip laser decreased. By the time the thermal gradient corresponded to  $\psi = 9.2 \times 10^{-5} \text{ rad}$  the sidelobes had smeared into a continuous tail [Figure 2-12(d)], and the intensity of the microchip laser had decreased by an order of magnitude.

The mirror misalignment tolerance for the microchip laser can be understood in terms of the thermal waveguiding effects in the microchip laser [14]. The thermally induced waveguide can be viewed as a radially dependent change in the optical length of the cavity. We expect that a waveguided mode cannot exist when the two cavity mirrors are out of parallel by an angle  $\psi$  that is comparable to the maximum gradient in the optical cavity length associated with the thermal waveguide. Using the same thermal modeling as in Reference 14, we find that the first sidelobe observed in the far-field intensity pattern of the microchip laser corresponds to a mirror misalignment of  $\sim 0.5$  times the calculated maximum thermally induced gradient in the optical cavity length. For a microchip laser similar to the one used in the experiments described here, this gives a mirror misalignment tolerance of  $\psi_{\text{max}} = 10^{-4} P_{\text{min}}$  rad, where  $P_{\text{min}}$  is the minimum pump power, in watts, for which the microchip laser should oscillate in a circularly symmetric  $\text{TEM}_{00}$  mode.

J.J. Zayhowski  
R.C. Hancock

## REFERENCES

1. L.F. Mollenauer and R.H. Stolen, *Opt. Lett.* **9**, 13 (1984); F.M. Mitschke and L.F. Mollenauer, *IEEE J. Quantum Electron.* **QE-22**, 2242 (1986).
2. K.J. Blow and D. Wood, *J. Opt. Soc. Am. B* **5**, 629 (1988).
3. K.J. Blow and B.P. Nelson, *Opt. Lett.* **13**, 1026 (1988); P.N. Kean, X. Zhu, D.W. Crust, R.S. Grant, N. Langford, and W. Sibbett, *Opt. Lett.* **14**, 39 (1989); J. Mark, L.Y. Liu, K.L. Hall, H.A. Haus, and E.P. Ippen, *Opt. Lett.* **14**, 48 (1989); C.P. Yakymyshyn, J.F. Pinto, and C.R. Pollock, *Opt. Lett.* **14**, 621 (1989); P.M.W. French, J.A.R. Williams, and J.R. Taylor, *Opt. Lett.* **14**, 686 (1989).
4. J. Goodberlet, J. Wang, J.G. Fujimoto, and P.A. Schulz, *Opt. Lett.* **14**, 1125 (1989).
5. T.H. Jeys, A.A. Brailove, and A. Mooradian, *Appl. Opt.* **28**, 2588 (1989).
6. Solid State Research Report, Lincoln Laboratory, MIT (1989:2), p. 23.
7. K. Kubodera and J. Noda, *Appl. Opt.* **21**, 3466 (1982).
8. T.M. Baer, D.F. Head, and M. Sakamoto, *CLEO Tech. Dig.* (Optical Society of America, Washington, DC, 1989), Paper FJ5.
9. J. Frauchinger, P. Albers, and H. P. Weber, *Proc. Topical Mtg. Tunable Solid State Lasers* (Optical Society of America, Washington, DC, 1989), p. 284.
10. T.Y. Fan, A. Sanchez, and W.E. DeFeo, *Opt. Lett.* **14**, 1057 (1989).
11. J.J. Zayhowski and A. Mooradian, *Opt. Lett.* **14**, 24 (1989).
12. H. Kogelnik, *Appl. Opt.* **4**, 1562 (1965).
13. J.J. Zayhowski and A. Mooradian, *Proc. Topical Mtg. Tunable Solid State Lasers* (Optical Society of America, Washington, DC, 1989), p. 288.
14. Solid State Research Report, Lincoln Laboratory, MIT (1989:4), p. 26.

### 3. MATERIALS RESEARCH

#### 3.1 PtSi SCHOTTKY-BARRIER FOCAL PLANE ARRAYS FOR MULTISPECTRAL IMAGING IN ULTRAVIOLET, VISIBLE AND INFRARED SPECTRAL BANDS

The operation of Schottky-barrier infrared (IR) detectors is based on internal photoemission at the interface between a thin silicide film and a Si substrate [1]. Conventionally, these detectors are operated in the back-illumination mode, i.e., radiation is incident on the surface of the Si substrate opposite from the silicide film. The IR photons with energies less than the band gap of Si are transmitted through the substrate and absorbed in the silicide film, where they generate the electrical carriers that produce the detector signal. On the other hand, visible and ultraviolet (UV) photons, which have energies higher than the band gap, are absorbed in the Si. The absorption depth decreases from  $\sim 5 \mu\text{m}$  at 800 nm to  $\sim 0.004 \mu\text{m}$  at 280 nm [2]. Because the thickness of a typical Si wafer is 400 to 500  $\mu\text{m}$  and transport of photogenerated carriers toward the silicide-Si Schottky-barrier junction occurs primarily by diffusion, carrier collection is slow and inefficient. Furthermore, for the shorter absorption lengths a large fraction of the carriers are lost by surface recombination. Thinning the Si substrate to a thickness comparable to the absorption depth could improve collection efficiency for carriers generated in the Si, but this technique has several drawbacks, including an increase in processing complexity that usually causes a reduction in device yield.

In this investigation, we have shown that Schottky-barrier diodes consisting of a 2-nm-thick PtSi film on a *p*-type Si substrate exhibit excellent photoresponse in the visible and near-UV regions, as well as in the IR, when the devices are operated in the front-illumination mode, with radiation incident on the silicide film. In addition, we have demonstrated high-quality imaging in both the visible and 3- to 5- $\mu\text{m}$  spectral bands with  $160 \times 244$ -element PtSi focal plane arrays.

The structure and fabrication procedures for the PtSi Schottky-barrier detectors are similar to those reported previously for back-illuminated devices [3]. Briefly, the detectors are fabricated on *p*-type (100) Si wafers by using electron-beam evaporation to deposit a 1-nm-thick Pt film in an ultrahigh vacuum system and subsequently annealing *in situ* at 400°C to form PtSi. The  $160 \times 244$ -element front-illuminated focal plane arrays are essentially identical to those previously reported [4] for back-illumination operation except that the front-side optical cavity structure has been eliminated. Figure 3-1 shows a schematic cross section of a single pixel. Electrons generated by UV, visible, and IR photons are accumulated on the PtSi electrode and subsequently transferred to the buried charge-coupled device (CCD) channel. An Al light shield is used to prevent generation of carriers in the CCD channel and transfer gate by above-band-gap radiation. The pixel area is  $40 \times 80 \mu\text{m}^2$  and the active detector area is  $25 \times 50 \mu\text{m}^2$ , for a fill factor of 39 percent.

The quantum efficiency of individual PtSi detectors was measured as a function of wavelength from 290 nm to 7  $\mu\text{m}$ . The quantum efficiency at a given wavelength was found to be nearly independent of temperature in the range from 10 to 80 K, where detector dark current is small compared with photocurrent. Figure 3-2 shows quantum efficiency as a function of wavelength for a typical front-illuminated detector at 50 K. For wavelengths beyond  $\sim 1 \mu\text{m}$ , corresponding to photon energies below the band gap of Si, the detector response is produced by carriers generated by absorption in the PtSi film.

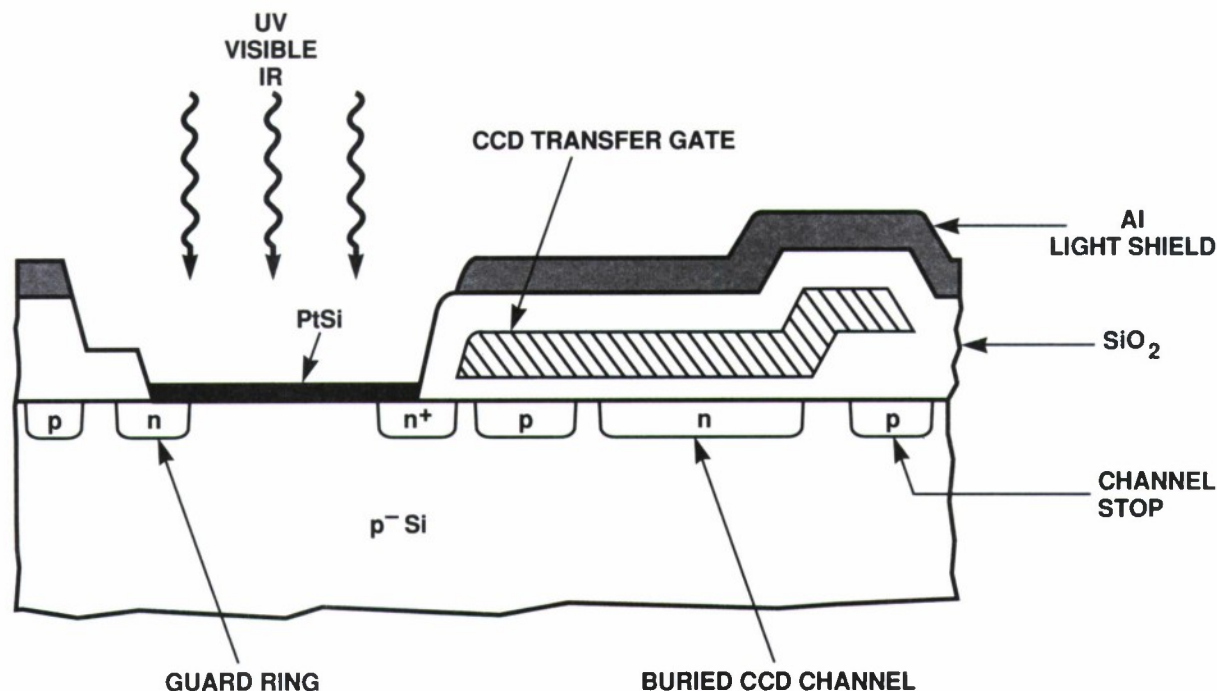


Figure 3-1. Schematic diagram showing a single pixel of a  $160 \times 244$ -element PtSi focal plane array operated in the front-illumination mode.

The wavelength dependence in this region is similar to that for back-illuminated Schottky-barrier detectors, with the efficiency decreasing from  $\sim 3$  percent at  $1.5 \mu\text{m}$  to  $\sim 0.02$  percent at  $6 \mu\text{m}$ . The scatter of the data beyond  $5 \mu\text{m}$  results because the output of the lamp used as the IR source drops rapidly beyond  $4 \mu\text{m}$ .

The data of Figure 3-2 between  $3.5$  and  $6.2 \mu\text{m}$  have been used to obtain the plot shown in Figure 3-3, where the square root of the product of quantum efficiency and photon energy is plotted as a function of photon energy. The experimental points can be fitted with a straight-line Fowler equation [5], which yields a Schottky-barrier height  $\psi$  of  $0.182 \text{ eV}$  and an emission coefficient  $C_1$  of  $0.08 \text{ eV}^{-1}$ . The value of  $C_1$ , which varies linearly with the fraction of incident radiation that is absorbed in the PtSi film,



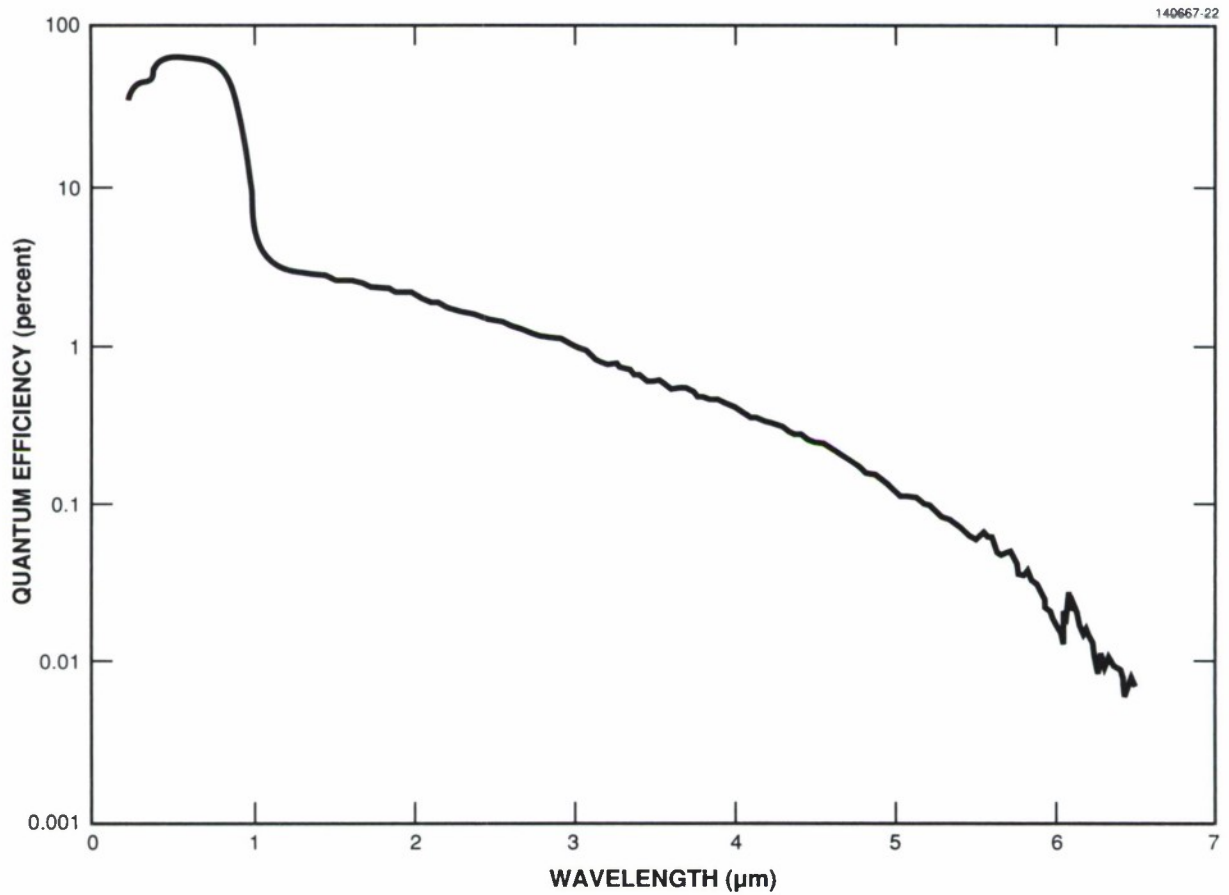


Figure 3-2. Quantum efficiency as a function of wavelength for a front-illuminated PtSi Schottky-barrier detector.

is a factor of 3 smaller than the  $C_1$  value of  $0.24 \text{ eV}^{-1}$  measured for the same detector when it was operated in the back-illumination mode. The reduction in  $C_1$  for front illumination occurs because absorption is decreased by reflection losses resulting from the high reflectivity of PtSi in the near-IR region; for back illumination, reflection losses in this region are reduced because the Si substrate serves as an index-matching layer for the PtSi.



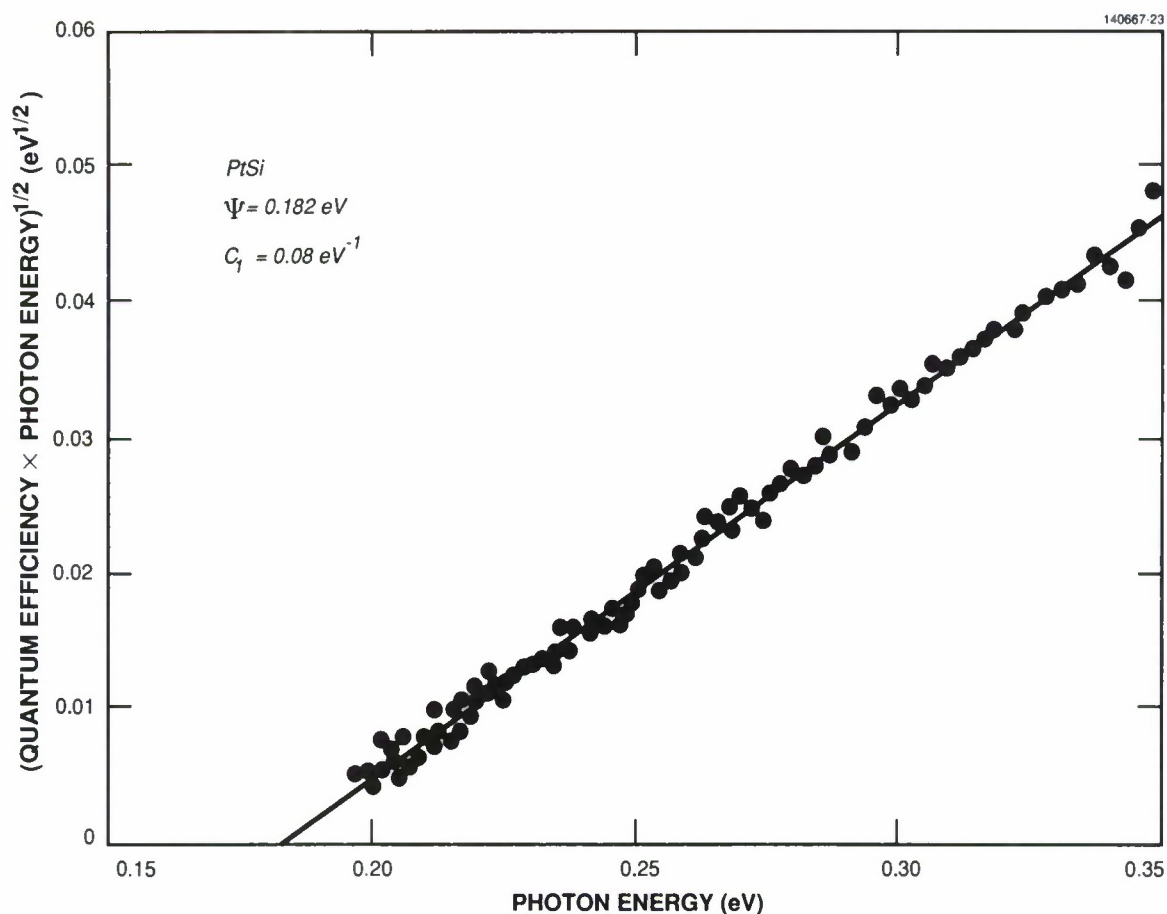


Figure 3-3. Fowler plot for the data of Figure 3-2 between 3.5 and 6.2  $\mu\text{m}$ .

When the photon energy is increased above the band gap of Si, the quantum efficiency increases drastically, as shown in Figure 3-2, because the radiation transmitted through the thin PtSi film is absorbed in the Si substrate and generates carriers that contribute to the detector response. The collection efficiency for these carriers is very high, since they are generated very close to the PtSi/Si interface, and this interface is of excellent crystalline quality. With decreasing wavelength the quantum efficiency rises to ~60 percent at 800 nm, remains essentially constant down to 400 nm, and then decreases to ~35 percent at 290 nm.

For a qualitative demonstration of the multispectral imaging capability of front-illuminated PtSi Schottky-barrier focal plane arrays, 160  $\times$  244-element arrays have been operated as both IR and visible sensors. The arrays were cooled to 77 K and evaluated in a benchtop imaging system. Figure 3-4(a) is

the IR image obtained without uniformity correction for a coffee mug that was partly filled with warm water. The radiation from the mug was focused on the array with an f/2.35 lens transmitting over the wavelength range from 3 to 5  $\mu\text{m}$ . The observed variation in brightness occurs because the handle and the region above the water level are cooler than the rest of the mug. The visible imaging capability of the same array is shown by Figure 3-4(b), which is the uncorrected image of the mug that was obtained in room light when the radiation was focused with an f/2.8 glass lens that did not transmit beyond  $\sim 2 \mu\text{m}$ .

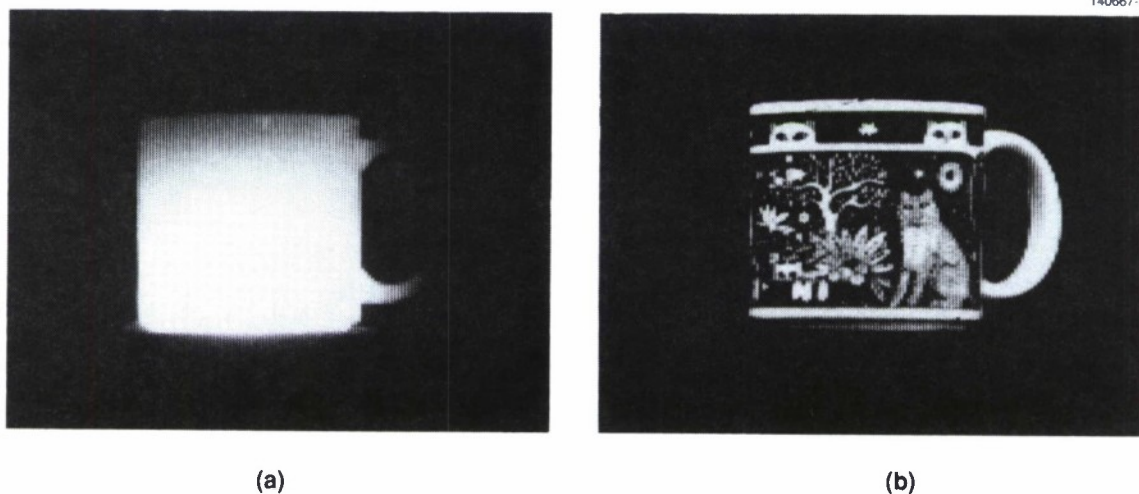


Figure 3-4. (a) Infrared and (b) visible images of a coffee mug obtained with a front-illuminated  $160 \times 244$ -element PtSi Schottky-barrier focal plane array.

In summary, front-illuminated PtSi Schottky-barrier diodes, in addition to being effective detectors for the 3- to 5- $\mu\text{m}$  region, exhibit excellent photoresponse in the visible and near-UV. In view of the demonstrated manufacturability of very large, highly uniform focal plane arrays integrating PtSi Schottky-barrier detectors and CCD readout circuitry, such arrays should be extremely useful for remote sensing and imaging applications where multispectral capability is advantageous.

B-Y. Tsaur  
C.K. Chen  
J.P. Mattia

### 3.2 EFFICIENT GaInAsSb/AlGaAsSb DIODE LASERS EMITTING AT 2.29 $\mu\text{m}$

The high-performance semiconductor diode lasers presently available are limited in emission wavelength to the spectral range between about 0.7 and 1.6  $\mu\text{m}$ . These devices incorporate heterostructures composed of III-V compounds and alloys — specifically, GaAs/AlGaAs and GaInAsP/InP heterostructures that are lattice matched to GaAs and InP substrates, respectively. High-performance lasers with emission wavelengths in the range of 2 to 5  $\mu\text{m}$  would be useful for a variety of applications, including optical communications employing fluoride-based fibers, laser radar exploiting atmospheric transmission windows, remote sensing of atmospheric gases, and molecular spectroscopy. With the objective of developing such devices, we have initiated an effort in the development of lattice-matched III-V diode lasers that incorporate GaInAsSb active layers and AlGaAsSb confining layers grown by molecular beam epitaxy (MBE) on GaSb substrates. Figure 3-5 is a plot of energy gap vs lattice constant for these two quaternary alloy systems at 300 K [6]. Since the emission wavelength corresponds approximately to the energy gap of the active layer, GaInAsSb/AlGaAsSb lasers can potentially provide room-temperature emission wavelengths from about 1.7 to 4.3  $\mu\text{m}$ .

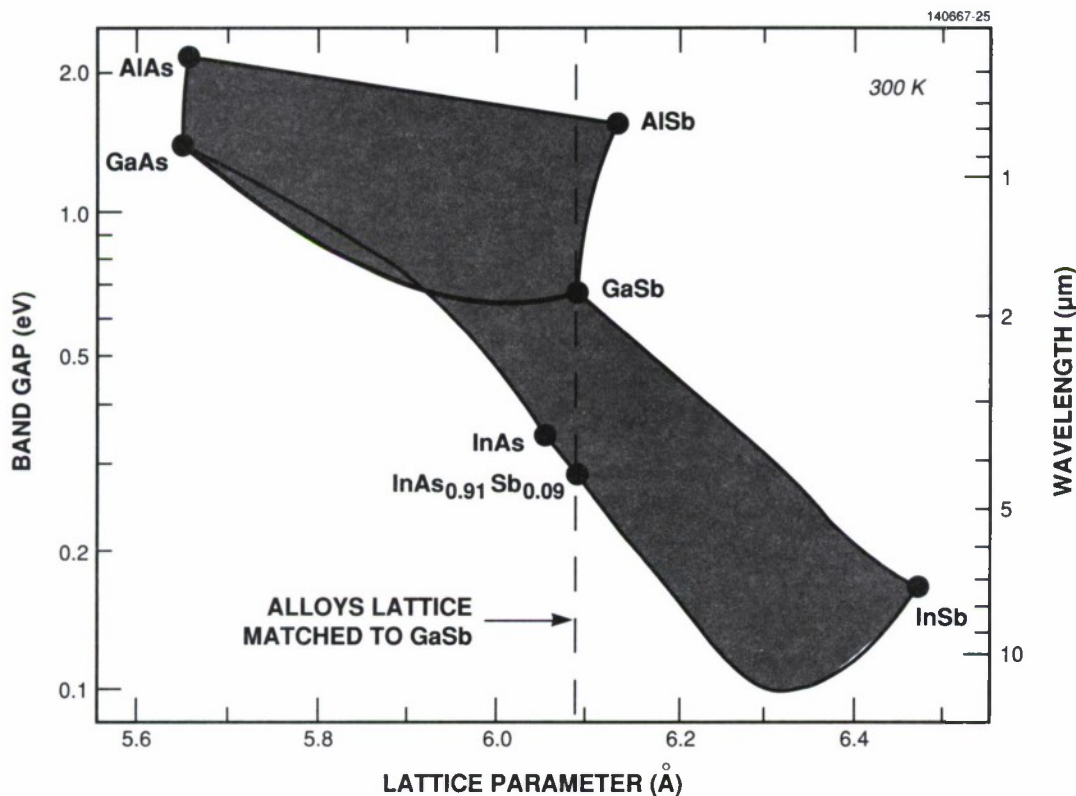


Figure 3-5. Energy gap vs lattice constant for GaInAsSb and AlGaAsSb quaternary alloys.

A number of groups have reported room-temperature operation of double-heterostructure GaInAsSb/AlGaAsSb lasers grown on GaSb by either liquid phase epitaxy (LPE) or MBE. The best performance has been obtained by Bochkarev *et al.* [7,8] for LPE-grown devices emitting at 2.2 to 2.3  $\mu\text{m}$ . They have reported a threshold current of 80 mA for CW operation of ridge-waveguide lasers [7] and a threshold current density  $J_{\text{th}}$  of 1.5  $\text{kA}/\text{cm}^2$  for broad-area devices [8]. The best results for MBE-grown lasers have been obtained by Chiu *et al.* [9], who reported pulsed operation with  $J_{\text{th}} = 4.2 \text{ kA}/\text{cm}^2$  for broad-area devices emitting at 2.2  $\mu\text{m}$ . In the present study, we have obtained  $J_{\text{th}} = 1.7 \text{ kA}/\text{cm}^2$  and a differential quantum efficiency of 15 percent per facet for pulsed room-temperature operation of MBE-grown broad-area lasers emitting at 2.29  $\mu\text{m}$ .

Commercial Te-doped  $n$ -GaSb (100) substrates were used for growth of the laser structures. Prior to MBE growth, a layer  $\sim 90 \text{ nm}$  thick was removed from the substrate by etching in  $\text{Br}_2:\text{HNO}_3:\text{HCl}:\text{CH}_3\text{COOH}$  [10]. The substrate was then loaded into the MBE vacuum system and heated in the presence of an Sb flux to desorb surface oxides and other contaminants. Reflection high-energy electron diffraction patterns revealed the  $3 \times 1$  reconstruction that is characteristic of Sb-stabilized GaSb (100) surfaces and showed that the substrate was clean and atomically smooth.

The sources used for MBE growth were the group III and group V elements, which yielded beams of Ga, In, and Al atoms and of  $\text{Sb}_4$  and  $\text{As}_4$  molecules. The substrate temperatures and V:III flux ratios for epilayer growth were optimized to yield the best surface morphology. A substrate temperature of  $530^\circ\text{C}$  was used for GaSb and AlGaAsSb, while  $500^\circ\text{C}$  was used for GaInAsSb. Since the efficiency of incorporation is near unity for Sb as well as for the group III elements, V:III flux ratios of  $\sim 1$  were used for GaSb growth. Arsenic is incorporated much less readily than Sb because, in comparison with  $\text{Sb}_4$ ,  $\text{As}_4$  has a shorter surface residence time (heat of sublimation of 37 kcal/mol for  $\text{As}_4$  vs 49 kcal/mol for  $\text{Sb}_4$  [11]) and is more stable (atomization energy of 252 kcal/mol for  $\text{As}_4$  vs 203 kcal/mol for  $\text{Sb}_4$  [11]). Therefore, the As and Sb mole fractions in the GaInAsSb and AlGaAsSb layers were controlled by using a large excess  $\text{As}_4$  flux and reducing the Sb:III ratio far enough below 1 to yield the desired Sb mole fraction. The impurity used for  $n$ -type doping was Te provided by the sublimation of GaTe, as suggested by Furukawa and Mizuta [12]. The  $p$ -type dopant was Be, which is conventionally used in the MBE growth of III-V materials.

As shown schematically in Figure 3-6, the laser structure consists of an  $n^+$ -GaSb buffer layer, an  $n\text{-Al}_{0.50}\text{Ga}_{0.50}\text{As}_{0.04}\text{Sb}_{0.96}$  confining layer, a nominally undoped  $\text{Ga}_{0.84}\text{In}_{0.16}\text{As}_{0.14}\text{Sb}_{0.86}$  active layer, a  $p\text{-Al}_{0.50}\text{Ga}_{0.50}\text{As}_{0.04}\text{Sb}_{0.96}$  confining layer, and a  $p^+$ -GaSb contacting layer. To fabricate broad-area lasers, the  $p^+$ -GaSb surface of the wafer was metallized with Cr/Au, and 100- or 300- $\mu\text{m}$ -wide stripes were defined by using photoresist lift-off. The  $p^+$  GaSb between the Cr/Au stripes was removed by etching in  $\text{H}_2\text{SO}_4:\text{H}_2\text{O}_2:\text{H}_2\text{O}$  to reduce current spreading. The wafer was lapped from the substrate side to 100- $\mu\text{m}$  thickness, and the  $n$ -GaSb surface was metallized with Au/Sn. Both metallizations were alloyed to form ohmic contacts. The wafer was cleaved into 300- $\mu\text{m}$  bars, which were then separated into individual lasers by scribing.



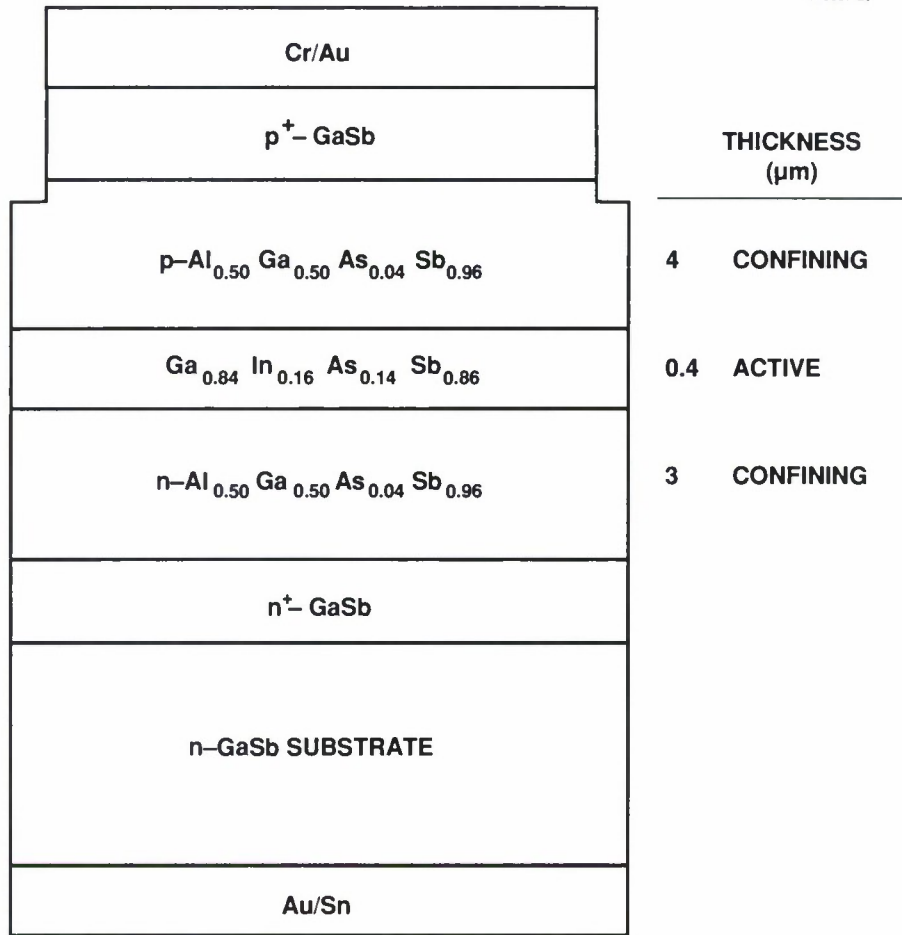


Figure 3-6. Schematic cross section of broad-stripe GaInAsSb/AlGaAsSb double-heterostructure diode laser.

Figure 3-7 shows the light output vs current for pulsed room-temperature operation of a  $300 \times 300\text{-}\mu\text{m}$  laser. The value of  $J_{\text{th}}$  is  $1.7 \text{ kA/cm}^2$ , and the differential quantum efficiency is 15 percent per facet. The highest power obtained, 250 mW per facet, was limited by the power supply used for the measurements. The emission spectrum, which is shown in Figure 3-8, is centered at  $2.29 \mu\text{m}$ . Very similar characteristics were measured for lasers fabricated from two wafers with nominally the same structure that were grown on consecutive days.

We regard the above results as highly encouraging, since they have been obtained in initial experiments on devices that are far from optimized. In particular, the  $J_{\text{th}}$  value of  $1.7 \text{ kA/cm}^2$  is well below the best value ( $4.2 \text{ kA/cm}^2$ ) previously reported for MBE-grown GaInAsSb/AlGaAsSb lasers and almost as low as the best value ( $1.5 \text{ kA/cm}^2$ ) reported for LPE-grown devices. Modifications in laser structure and device design, as well as further development of the MBE growth technique and device

processing procedures, can be expected to result in major improvements in performance, and it should not be difficult to achieve room-temperature CW operation for narrow-stripe devices with adequate heat sinking. Furthermore, on the basis of the present results for lasers emitting at  $2.29\ \mu\text{m}$ , we believe that it should be possible to extend the emission to significantly longer wavelengths by using the same basic structure of GaInAsSb/AlGaAsSb lattice matched to GaSb, but changing the composition of the active layer to reduce the energy gap. Because of the existence of a miscibility gap in the GaInAsSb system, the compositions of lattice-matched layers that can be grown by LPE are restricted to a range that places an upper limit of about  $2.3\ \mu\text{m}$  on the room-temperature emission wavelength. Because of the non-equilibrium character of the MBE process, however, in principle it should be possible to grow by MBE any GaInAsSb alloy that is lattice matched to GaSb. For the alloy with the lowest energy gap,  $\text{InAs}_{0.91}\text{Sb}_{0.09}$ , the emission wavelength would be  $4.3\ \mu\text{m}$ .

S.J. Eglash  
H.K. Choi

J.V. Pantano  
G.W. Turner

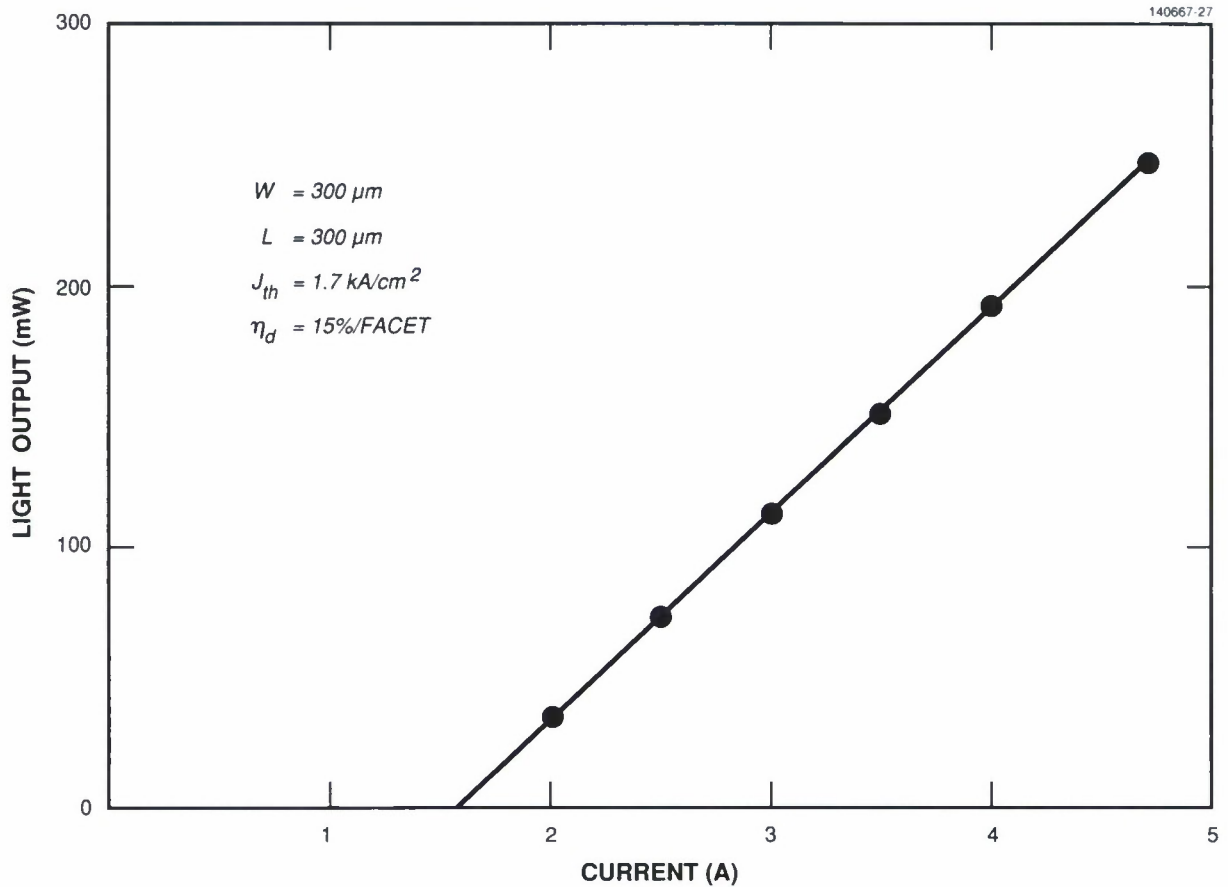
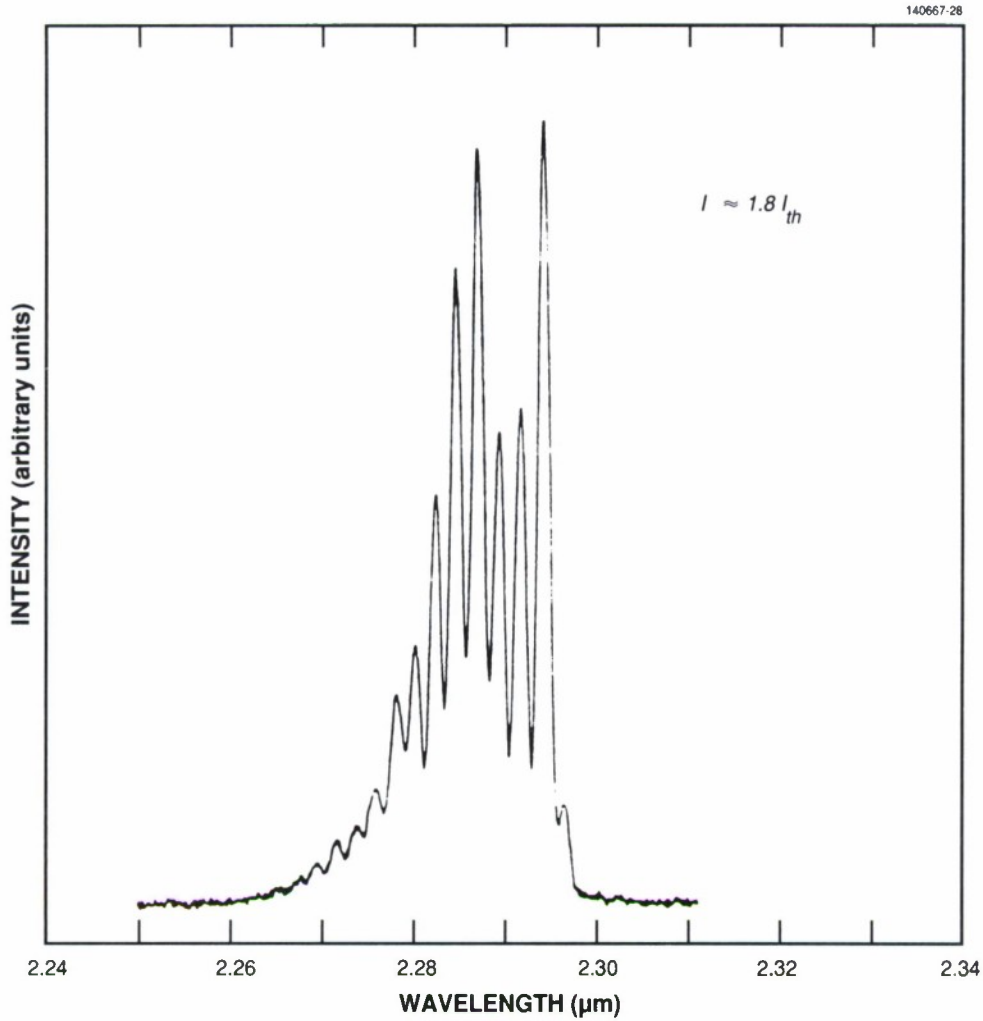


Figure 3-7. Light output vs current characteristic of GaInAsSb/AlGaAsSb diode laser for pulsed operation at room temperature.



*Figure 3-8. Emission spectrum of GaInAsSb/AlGaAsSb diode laser for pulsed operation at room temperature.*

### **3.3 ROOM-TEMPERATURE CONTINUOUS OPERATION OF GaAs/AlGaAs LASERS GROWN ON Si BY OMVPE**

By conveniently combining the most desirable features of both III-V and Si devices and circuits, monolithic GaAs-on-Si technology potentially offers important advantages for such applications as optoelectronic integrated circuits and optical interconnects between very large scale integrated circuits. Practical implementation of this technology will require the development of manufacturable GaAs/AlGaAs diode lasers, fabricated on Si substrates, that are capable of reliable CW operation with sufficiently low threshold currents. Room-temperature CW operation of GaAs/AlGaAs-on-Si lasers incorporating a

GaAs buffer layer adjacent to the substrate has been reported by Deppe *et al.* [13], who grew the buffer by MBE and the laser structure by organometallic vapor phase epitaxy (OMVPE). These authors obtained a threshold current of 24 mA for devices with a stripe width of 4  $\mu\text{m}$  and a cavity length of 305  $\mu\text{m}$ . Room-temperature CW operation has also been reported by Chen *et al.* [14], who grew both the buffer and the laser structure by MBE. They obtained a threshold current density  $J_{\text{th}}$  of  $\sim 300 \text{ A/cm}^2$  for broad-stripe devices with a cavity length of 980  $\mu\text{m}$ . For large-scale production, it would be advantageous to perform the growth entirely by OMVPE. In a brief report, Connolly *et al.* [15] have described all-OMVPE diode lasers with a pulsed  $J_{\text{th}}$  of  $1.5 \text{ kA/cm}^2$  for broad-stripe devices with a cavity length of 500  $\mu\text{m}$ , and a CW threshold current of 65 mA for ridge-waveguide devices with a stripe width of 5  $\mu\text{m}$ . In the present investigation, we have considerably improved the performance of all-OMVPE GaAs/AlGaAs-on-Si lasers by incorporating a defect-filtering layer between the buffer layer and the laser structure. Pulsed  $J_{\text{th}}$  values as low as  $350 \text{ A/cm}^2$  have been measured for broad-stripe lasers with a cavity length of 500  $\mu\text{m}$ , and CW threshold currents as low as 25 mA and a differential quantum efficiency  $\eta_d$  of 55 percent have been obtained for ridge-waveguide devices.

The substrate used for the all-OMVPE lasers was an  $n^+$ -Si wafer oriented  $2^\circ$  off (100) toward (110). An  $n^+$ -GaAs buffer layer  $\sim 1.5 \mu\text{m}$  thick, consisting of a 10-nm layer deposited at  $\sim 450^\circ\text{C}$  and the remainder deposited at  $\sim 680^\circ\text{C}$ , was grown at Kopin Corporation. The defect-filtering layer and the laser structure were grown at Lincoln Laboratory. The laser structure was a graded-index separate-confinement heterostructure (GRIN-SCH) with a single quantum well, consisting of the following layers: 1- $\mu\text{m}$ -thick  $n\text{-Al}_{0.7}\text{Ga}_{0.3}\text{As}$  cladding layer, 0.15- $\mu\text{m}$ -thick  $n\text{-AlGaAs}$  confining layer (AlAs mole fraction linearly graded from 0.7 to 0.2), 6-nm-thick GaAs active layer, 0.15- $\mu\text{m}$ -thick  $p\text{-AlGaAs}$  confining layer (AlAs mole fraction linearly graded from 0.2 to 0.7), 1- $\mu\text{m}$ -thick  $p\text{-Al}_{0.7}\text{Ga}_{0.3}\text{As}$  cladding layer, and 0.25- $\mu\text{m}$ -thick  $p^+$ -GaAs contacting layer. Growth was performed at  $800^\circ\text{C}$ , using trimethylgallium, trimethylaluminum, 100-percent arsine,  $\text{H}_2\text{Se}$ , and dimethyl zinc.

Four different defect-filtering layers were investigated: (1) a thin superlattice composed of AlGaAs and GaAs layers, each 10 nm thick, grown at  $800^\circ\text{C}$ ; (2) a thick superlattice composed of 10-nm-thick AlGaAs and 100-nm-thick GaAs layers grown at  $800^\circ\text{C}$ ; (3) a series of temperature-cycled GaAs layers (annealed at  $800^\circ\text{C}$  for 5 min, 100-nm-thick layer grown at  $700^\circ\text{C}$ , temperature lowered to  $300^\circ\text{C}$ , annealed at  $800^\circ\text{C}$  to begin the next cycle); and (4) a temperature-cycled thick superlattice (10-nm-thick AlGaAs grown at  $800^\circ\text{C}$ , 100-nm-thick GaAs grown at  $700^\circ\text{C}$ , temperature lowered to  $300^\circ\text{C}$ , then increased to  $800^\circ\text{C}$  for the next AlGaAs layer). Each defect-filtering layer consisted of 5 periods. The AlAs mole fraction in the AlGaAs layers was 0.7.

In order to characterize the quality of the laser structures grown on different defect-filtering layers, broad-stripe lasers were fabricated for testing under pulsed conditions. By means of evaporation and photolithographic lift-off, 100- $\mu\text{m}$ -wide Cr/Au stripes on 400- $\mu\text{m}$  centers were defined on the surface of the  $p^+$ -GaAs contacting layer, which was then etched away between the stripes to reduce current spreading. The wafer was thinned from the back side to  $\sim 70 \mu\text{m}$ , and Ti/Au was evaporated on the Si surface and subsequently alloyed. The wafer was cleaved into 500- $\mu\text{m}$  bars, which were then separated into individual lasers by scribing.



**TABLE 3-1**  
**Effect of Defect-Filtering Layers on Characteristics of Broad-Stripe**  
**AlGaAs/GaAs-on-Si Diode Lasers**

Defect-Filtering Layer	$J_{th}$ (A/cm <sup>2</sup> )	$\eta_d$ (percent)
Thin Superlattice	640	50
Thick Superlattice	540	53
Thermally Cycled Superlattice	370	59
Thermally Cycled GaAs	350	63

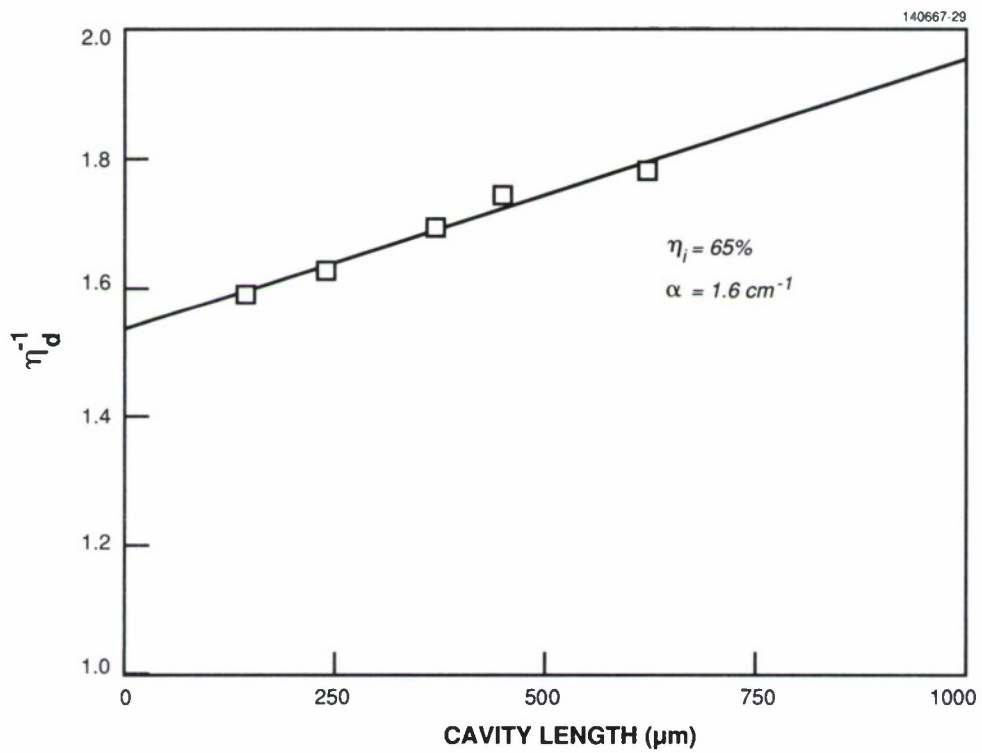


*Figure 3-9. Differential quantum efficiency vs cavity length for broad-stripe AlGaAs/GaAs-on-Si diode lasers with thermally cycled GaAs defect-filtering layer.*

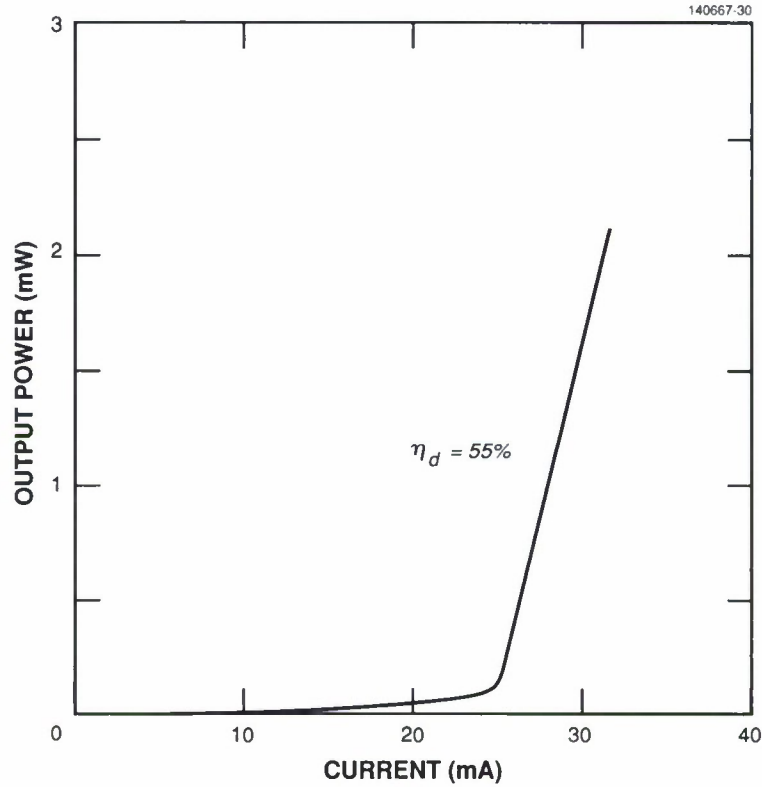


Figure 3-10. Light output vs current for room-temperature CW operation of ridge-waveguide AlGaAs/GaAs-on-Si diode laser with thermally cycled GaAs defect-filtering layer.

Testing was performed with 200-ns current pulses at 10 kHz. There was no abnormal delay in the laser emission, indicating that the density of saturable absorbers in the active layer is very low. The near-field pattern observed at twice the threshold current was fairly uniform across the entire stripe width. Table 3-1 summarizes the  $J_{th}$  and  $\eta_d$  values obtained from curves of light output vs current for lasers with a 500- $\mu\text{m}$  cavity length grown on the four types of defect-filtering layers. The poorest results were obtained with the thin superlattice filter, for which  $J_{th}$  is 640 A/cm<sup>2</sup> and  $\eta_d$  is 50 percent. The thermally cycled GaAs filter yielded the best laser performance, with  $J_{th}$  of 350 A/cm<sup>2</sup> and  $\eta_d$  of 63 percent. In comparison, broad-stripe lasers with the same GRIN-SCH structure grown by OMVPE on a GaAs substrate without defect filtering had  $J_{th}$  of 180 A/cm<sup>2</sup> and  $\eta_d$  of ~80 percent. (In an earlier study on all-OMVPE GaAs/AlGaAs-on-Si GRIN-SCH lasers grown without defect filtering, we measured  $J_{th}$  values as low as 300 A/cm<sup>2</sup> for broad-stripe devices, but these values were reduced by filamentary lasing, which was revealed by the near-field pattern [16]).

For broad-stripe lasers with a thermally cycled GaAs defect-filtering layer,  $J_{th}$  was found to decrease monotonically with increasing cavity length, from ~520 A/cm<sup>2</sup> for 300  $\mu\text{m}$  to ~320 A/cm<sup>2</sup> for 750  $\mu\text{m}$  and above. Figure 3-9 shows the dependence of  $\eta_d^{-1}$  on cavity length. The straight line drawn

through the points yields values of 65 percent for the internal quantum efficiency  $\eta_i$  and  $1.6 \text{ cm}^{-1}$  for the absorption coefficient  $\alpha$ . For devices with a slightly different laser structure grown on a GaAs substrate [17],  $\eta_i$  was higher than 90 percent and  $\alpha$  was  $2.5 \text{ cm}^{-1}$ .

In order to reduce the laser threshold current sufficiently to achieve CW operation, ridge-waveguide devices were fabricated from a wafer having the thermally cycled GaAs defect-filtering layer. The processing procedure was similar to the one used in our earlier study [16]. Figure 3-10 shows the light output vs current for CW operation at room temperature. The threshold current is 25 mA, and  $\eta_d$  is 55 percent. The light emitted was almost entirely TE polarized.

The ridge-waveguide lasers degraded rapidly under CW operation. The threshold current doubled in about 5 min, and  $\eta_d$  was significantly reduced during this time. For even the most reliable GaAs/AlGaAs-on-Si lasers so far reported [18], the CW threshold current increased by a factor of 3 in 10 h. This rapid degradation is caused by the formation and propagation of dark-line defects, which take place at high rates because GaAs and AlGaAs epilayers grown on Si by present techniques contain high densities of threading dislocations and are subject to high tensile stress. Major improvements in material quality are still necessary in order to increase the reliability of the lasers to the level required for practical applications.

H.K. Choi  
C.A. Wang

### **3.4 CHEMICAL VAPOR DEPOSITION OF BORON NITRIDE FOR COATING FUSED SILICA CRUCIBLES**

Fused silica is a very convenient container material for use in the synthesis and crystal growth of many semiconductors, because silica crucibles can be formed in almost any desired shape and silica ampoules can easily be sealed off under vacuum. However, materials with high melting points can become contaminated with Si when their melts are in contact with fused silica for extended periods. In the Bridgman growth of CdTe (m.p.  $1098^\circ\text{C}$ ), Si contamination is avoided by using silica ampoules coated with pyrolytic graphite, but pyrolytic graphite coatings are unsatisfactory for InP (m.p.  $1060^\circ\text{C}$ ) and GaAs (m.p.  $1240^\circ\text{C}$ ), since carbon is an electrically active impurity in these compounds. Crystals of these materials are generally grown from melts contained in pyrolytic boron nitride (PBN) crucibles. Although high-quality crystals can be obtained routinely, these crucibles are extremely expensive, their delivery times are usually very long, and they are limited in shape to tapered cylindrical sections.

In order to overcome these disadvantages, for our program on InP crystal growth we have developed a chemical vapor deposition process for coating fused silica crucibles, boats, and tubes with a thin film of BN. Data for crystals grown from the melt by the liquid-encapsulated Czochralski (LEC) method show that the same purity is obtained with BN-coated crucibles as with PBN crucibles. In addition to being much less costly, the BN-coated crucibles are advantageous for LEC growth because the coating can be restricted to the portion of the crucible that will be in contact with the melt. Radiative heat transfer

through the upper portion of the crucible, which remains transparent, reduces the radial temperature gradient in the solidified crystal and leads to a reduction in the dislocation density.

The BN deposition procedure is based on a process originally developed by Lewandowski [19] for using the high-temperature reaction between  $\text{NH}_3$  and  $\text{B}_2\text{H}_6$  (diborane) to coat small fused silica parts used in LPE of GaP. Deposition is performed inside a fused silica tube that is heated in a horizontal resistance furnace 45 cm long and 9.5 cm in inside diameter, which is wound with Kanthal wire. The object to be coated is cleaned by etching in a 2:1 mixture of  $\text{HCl}$  and  $\text{HNO}_3$ , rinsed with deionized water, and placed inside the fused silica tube. Growth crucibles are positioned with their open end facing the gas inlet. The system is purged with Ar gas, and the temperature is raised to 950 to 975°C. The Ar is turned off and  $\text{NH}_3$  is admitted at a flow rate of 140  $\text{cm}^3/\text{min}$ . Finally, a mixture of Ar with 1.5-percent  $\text{B}_2\text{H}_6$  is admitted at a flow rate of 65  $\text{cm}^3/\text{min}$  through a separate tube that extends into the crucible in order to limit BN deposition upstream. (If the  $\text{B}_2\text{H}_6$  mixture were introduced before the  $\text{NH}_3$ ,  $\text{B}_2\text{H}_6$  would decompose rapidly to form an undesirable B film.) Most coating runs are carried out overnight. To terminate deposition, the  $\text{B}_2\text{H}_6$  mixture is turned off. Then the  $\text{NH}_3$  is turned off, the Ar is turned on, and the furnace is cooled to room temperature. Thorough Ar purging is essential to prevent the gas lines and other components from becoming clogged, presumably by boric oxide formed by the reaction of  $\text{B}_2\text{H}_6$  with air, which occurs even at room temperature. For the same reason, all components, including pressure regulators, valves, flowmeters and manifolds, must be checked with a He leak tester (even if their tightness is guaranteed by the manufacturer). Since both  $\text{NH}_3$  and  $\text{B}_2\text{H}_6$  are toxic, the entire deposition system (except for the Ar cylinder) is placed in a chemical fume hood, and the  $\text{B}_2\text{H}_6$  concentration inside the hood is continuously checked by a toxic gas monitor.

With the gas flow rates given above, fused silica components held at 950 to 975°C for about 16 h are coated with a smooth, adherent, opaque white film a few micrometers thick. The flat-bottomed crucibles used in LEC growth, which are 7.5 cm in diameter and 6 to 8 cm high, are coated only on the inside. Deposition can be restricted to the lower part of the crucible by shielding the upper part with a tight-fitting cylindrical fused silica tube. Analysis of a test coating by Auger electron spectroscopy showed the atomic ratio of B to N to be unity within the experimental uncertainty of a few percent, and no other elements were detected. Examination by scanning electron microscopy showed that the coatings have a dendritic structure.

We are now routinely using BN-coated fused silica crucibles for LEC growth of InP crystals. The results of numerous growth runs using starting charges obtained from nominally undoped polycrystalline ingots synthesized in our laboratory show that essentially the same purity is obtained with BN-coated crucibles as with PBN crucibles. All the crystals are *n*-type, with electron mobilities showing that the residual donor impurities are uncompensated by acceptors. For nine crystals grown from charges in BN-coated crucibles, the average carrier concentration is  $5.0 \times 10^{15} \text{ cm}^{-3}$  and the average mobility at 77 K is  $3.1 \times 10^4 \text{ cm}^2\text{V}^{-1}\text{s}^{-1}$ ; the corresponding averages for eight earlier crystals grown from charges in PBN crucibles are  $5.2 \times 10^{15} \text{ cm}^{-3}$  and  $3.0 \times 10^4 \text{ cm}^2\text{V}^{-1}\text{s}^{-1}$ . (In contrast, for two crystals grown from charges in uncoated fused silica crucibles, the measured values of *n* were  $9.7 \times 10^{15} \text{ cm}^{-3}$  and  $2.1 \times 10^{16} \text{ cm}^{-3}$ .)



We have also used BN-coated fused silica crucibles in several runs for InP crystal growth by the vertical gradient-freeze method, in which the solidifying crystal is in contact with the crucible wall. All these runs yielded single crystals, showing that the BN coating does not cause secondary nucleation leading to polycrystalline growth.

H.R. Clark, Jr.  
G.W. Iseler

## REFERENCES

1. F.D. Shepherd and A.C. Yang, *IEDM Tech. Dig.* (IEEE, New York, 1973), p. 310.
2. E.D. Palik, *Handbook of Optical Constants of Solids* (Academic Press, Orlando, Florida, 1985), p. 555.
3. B-Y. Tsaur, M.M. Weeks, and P.W. Pellegrini, *IEEE Electron Device Lett.* **9**, 100 (1988).
4. W.F. Kosonocky, F.V. Shallcross, T.S. Villani, and J.V. Groppe, *IEEE Trans. Electron Devices* **ED-22**, 1564 (1985).
5. V.L. Dalal, *J. Appl. Phys.* **42**, 2274 (1971).
6. H.C. Casey, Jr. and M.B. Panish, *Heterostructure Lasers, Part B* (Academic Press, New York, 1978).
7. A.E. Bochkarev, L.M. Dolginov, A.E. Drakin, P.G. Eliseev, and B.N. Sverdlov, 11th IEEE Intl. Semiconductor Laser Conf., Boston, Massachusetts, 1988, Post-Deadline Paper No. 8.
8. A.E. Bochkarev, L.M. Dolginov, A.E. Drakin, P.G. Eliseev, and B.N. Sverdlov, *Sov. J. Quantum Electron.* **18**, 1362 (1988).
9. T.H. Chiu, W.T. Tsang, J.A. Ditzenberger, and J.P. van der Ziel, *Appl. Phys. Lett.* **49**, 1051 (1986).
10. M. Silga, F.W.O. da Silva, C. Raisin, and L. Lassabatere, *Vide Couches Minces* **241**, 163 (1988); L. Lassabatere, private communication.
11. C-A. Chang, R. Ludeke, L.L. Chang, and L. Esaki, *Appl. Phys. Lett.* **31**, 759 (1977).
12. A. Furukawa and M. Mizuta, *Electron. Lett.* **24**, 1378 (1988).
13. D.G. Deppe, D.W. Nam, N. Holonyak, Jr., K.C. Hsieh, R.J. Matyi, H. Shichijo, J.E. Epler, and H.F. Chung, *Appl. Phys. Lett.* **51**, 1271 (1987).
14. H.Z. Chen, A. Ghaffari, H. Wang, H. Morkoç, and A. Yariv, *Opt. Lett.* **12**, 812 (1987).
15. J.C. Connolly, N. Dinkel, R. Menna, D.B. Gilbert, and M.G. Harvey, *CLEO Tech. Dig.* (Optical Society of America, Washington, DC, 1989), Paper F06.
16. H.K. Choi, J.W. Lee, J.P. Salerno, M.K. Connors, B-Y. Tsaur, and J.C.C. Fan, *Appl. Phys. Lett.* **52**, 1114 (1988).
17. C.A. Wang, H.K. Choi, and M.K. Connors, *Photon. Technol. Lett.* **1**, 351 (1989).
18. D.C. Hall, D.G. Deppe, N. Holonyak, Jr., R.J. Matyi, H. Shichijo, and J.E. Epler, *J. Appl. Phys.* **64**, 2854 (1988).
19. R.S. Lewandowski, U.S. Patent No. 4,522,849 (11 June 1985).

## 4. SUBMICROMETER TECHNOLOGY

### 4.1 NEW PHOTOMASK TECHNOLOGY FOR 193-nm LITHOGRAPHY

An important aspect of our effort on 193-nm lithography is the evaluation of potential resist materials. In order to assist in testing the lithographic properties of such resists down to 0.1- $\mu\text{m}$  resolution we have used our electron-beam capabilities to design and fabricate appropriate masks for both contact and projection printing.

The mask used in contact printing has features ranging from 0.1 to 1.0  $\mu\text{m}$  in 0.1- $\mu\text{m}$  steps, and from 1.0 to 2.0  $\mu\text{m}$  in 0.2- $\mu\text{m}$  steps. To help speed characterization, the pattern is 1 mm long, so that it can be easily identified in optical and electron microscopes. A photomicrograph of the pattern from 0.7 to 1.4  $\mu\text{m}$  is shown in Figure 4-1, with areas of freestanding lines (lines separated by more than a linewidth), via holes in both positive and negative polarities, a corner turn, and gratings with equal lines and spaces. The mask used in projection lithography has nested lines and spaces 14.8, 18.5, and 22.2  $\mu\text{m}$  wide so as to yield 0.2-, 0.25-, and 0.3- $\mu\text{m}$  features when imaged by high-reduction optics.

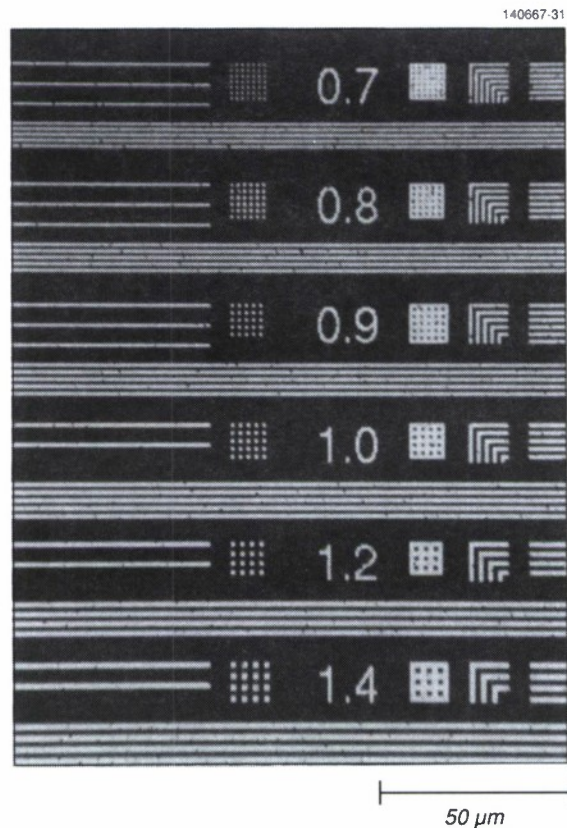


Figure 4-1. Photomicrograph of features from 0.7 to 1.4  $\mu\text{m}$  of a pattern fabricated with electron-beam lithography in Al on fused silica, and used in 193-nm contact printing. Areas from left to right are freestanding lines, via holes in positive polarity, via holes in negative polarity, a corner turn, and gratings with equal lines and spaces.

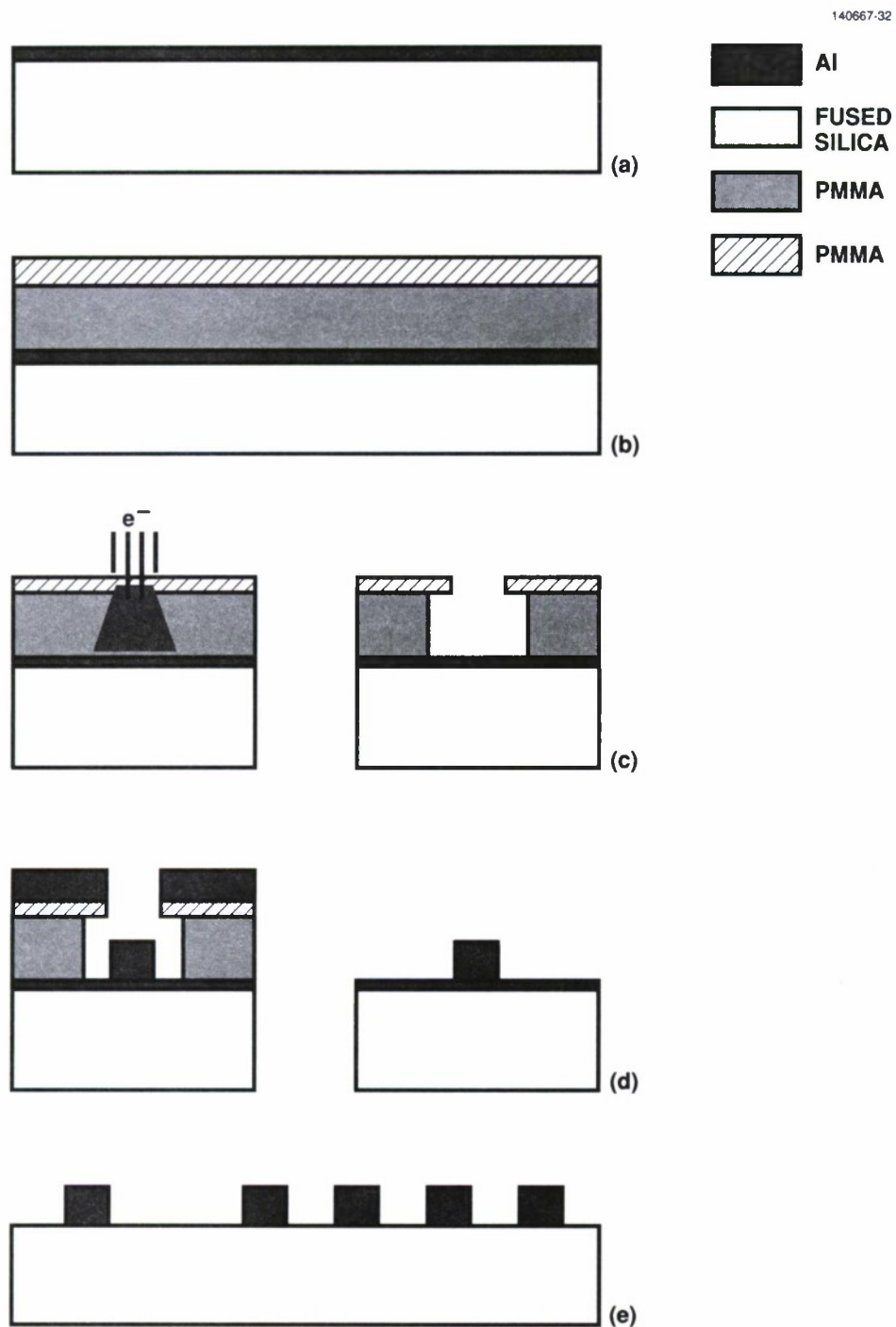
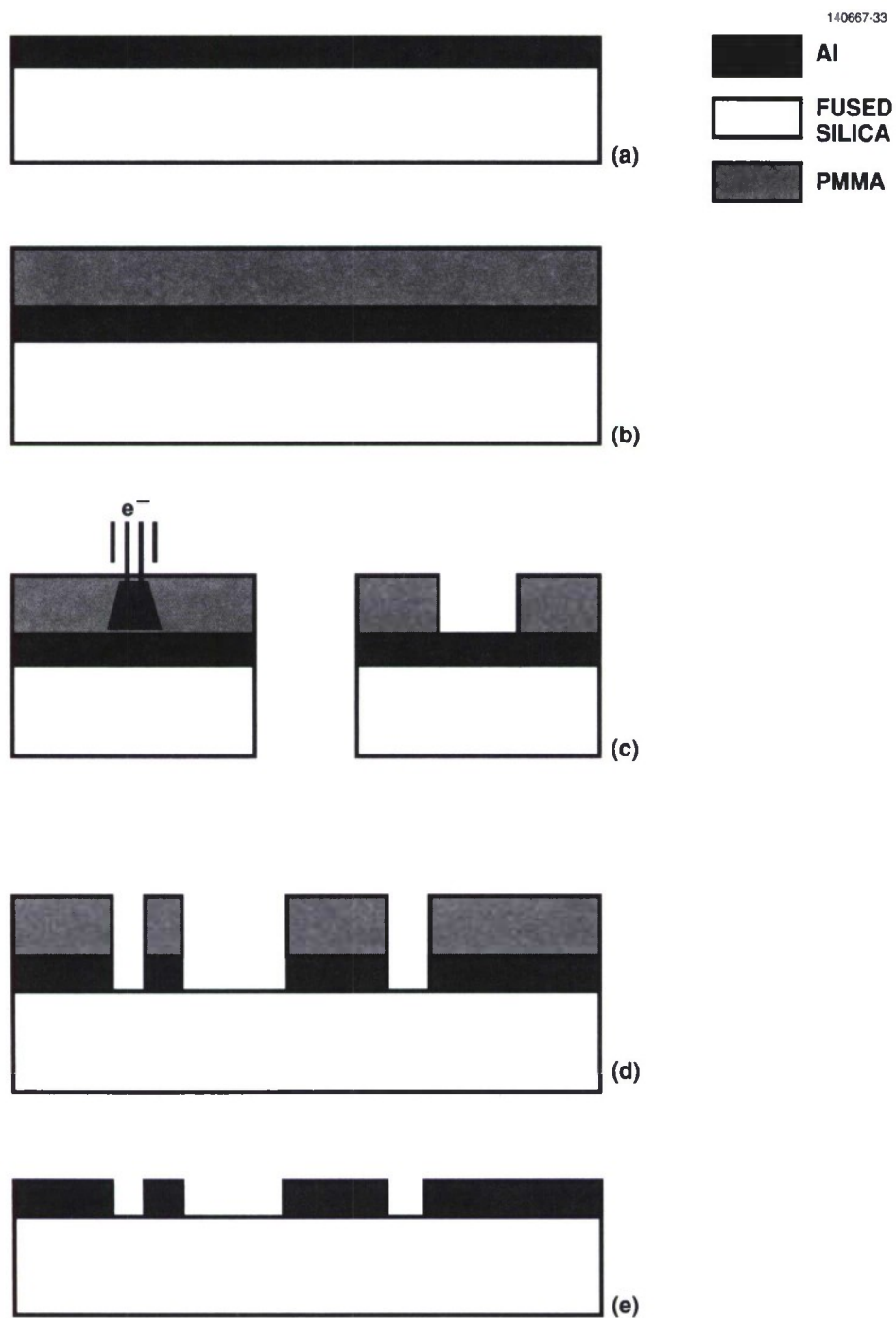


Figure 4-2. Process sequence in fabrication of photomask for 193-nm contact printing. Stages shown are (a) sample preparation, (b) resist spinning, (c) exposure and development, (d) evaporation and lift-off, and (e) aluminum etching.





*Figure 4-3. Process sequence in fabrication of photomask for 193-nm projection printing. Stages shown are (a) sample preparation, (b) resist spinning, (c) exposure and development, (d) aluminum etching, and (e) resist removal.*

The short exposure wavelength, 193 nm, introduces specific constraints on the choice of the substrate material and patterned metal. First, the low-expansion borosilicate glass used as substrate material in conventional photomasks is opaque at 193 nm. In fact, the list of transmissive materials includes only a few crystalline metal fluorides and high-purity fused silica. We chose the latter because of its mechanical stability and its commercial availability in large sizes and high quality. Specifically, highly polished disks (5- $\mu\text{m}$  flatness) are readily available with diameters of 25, 50, and 75 mm. Second, to minimize heat buildup on a photomask, the opaque sections need to be reflective; while at longer wavelengths chromium is the preferred metal, at 193 nm aluminum is the only metal with high reflectivity (0.93 for freshly deposited Al, as compared with 0.24 for Cr, 0.21 for Au, and 0.35 for Ni). We therefore chose Al for our masks. This choice implied the use of polymethylmethacrylate (PMMA) as the resist material, because the standard developers for novolac-based electron-beam resists prematurely etch Al, while the developer for PMMA (a mixture of methylisobutylketone and isopropanol) is relatively inert.

The fabrication processes for the two masks are shown schematically in Figure 4-2 for the smaller features used in contact printing, and in Figure 4-3 for the larger features used in projection printing. In the first step, the fused silica substrate is cleaned and 10 nm of aluminum is deposited on the surface to ensure that the substrate is conductive during electron-beam writing [Figure 4-2(a)]. Next, the substrate is coated with a bilayer resist system consisting of 150 nm of low-molecular-weight ( $1.28 \times 10^5$ ) PMMA and 50 nm of high-molecular-weight ( $4.5 \times 10^5$ ) PMMA [Figure 4-2(b)], and the patterns are written using a high-resolution, vector-scan electron-beam lithography system (200- $\mu\text{C}/\text{cm}^2$  dose, 25-kV electron energy). Because the PMMA layers have differing molecular weights (and therefore different sensitivities), a 1.5-min development in a 40/60-percent mixture of methylisobutylketone/isopropanol leaves the “cutback” profiles ideal for metal lift-off [Figure 4-2(c)]. Another 80 nm of Al are evaporated over the wafer, and the resist images are transferred to metal images by an acetone lift-off [(Figure 4-2(d)]. In the final step, the entire substrate is exposed to a short Al etch, which removes the exposed charge dissipation layer [Figure 4-2(e)].

For the larger features in projection printing masks, the simpler process shown in Figure 4-3 could be used. The fused silica wafer is cleaned and coated with 100 nm of Al [Figure 4-3(a)]. For wet-etching, a single layer of PMMA is sufficient, and a layer at least 500 nm thick is spun on and cured [Figure 4-3(b)]. The same exposure and development parameters are used as in the lift-off process (Figure 4-2). After development [Figure 4-3(c)], the PMMA serves as an etch mask and the aluminum is patterned chemically using a Transene etchant [Figure 4-3(d)]. The projection mask after the PMMA has been stripped away by acetone or a helium-oxygen plasma is shown in Figure 4-3(e).

Both masks have been successfully used to image features as small as 0.2  $\mu\text{m}$  in silylation schemes, in plasma-deposited imaging layers, and in spun-on silicon-containing photoresists at 193 nm.

C.L. Dennis  
T.M. Lyszczarz

## 4.2 SILYLATION PROCESSES FOR 193-nm LITHOGRAPHY

Several surface-imaging lithography processes have been developed in the past few years to alleviate problems caused by reflective substrates, shallow depths of focus, and resist opacity [1-3]. A surface-imaging process can also accomplish planarization of device topology without resorting to a multilayer process. Among the best known surface-imaging techniques are silylation processes. Negative- and positive-tone silylation processes are shown schematically in Figure 4-4. After exposure, the latent image in the resist film is used to distinguish the diffusion and reaction rates for a silicon-containing reagent in the exposed and unexposed regions. This selective incorporation of silicon is then used to create an etching mask during pattern transfer in an oxygen plasma. For instance, in most negative-tone processes, a novolac/diazoquinone resist is used, and exposure of the film converts the diazoquinone into a carboxylic acid. Diazoquinone remaining in the unexposed areas decomposes during the heated silylation step and is presumed [1-3] to crosslink with the novolac resin, which both hinders the diffusion and destroys some of the available sites for silylation.

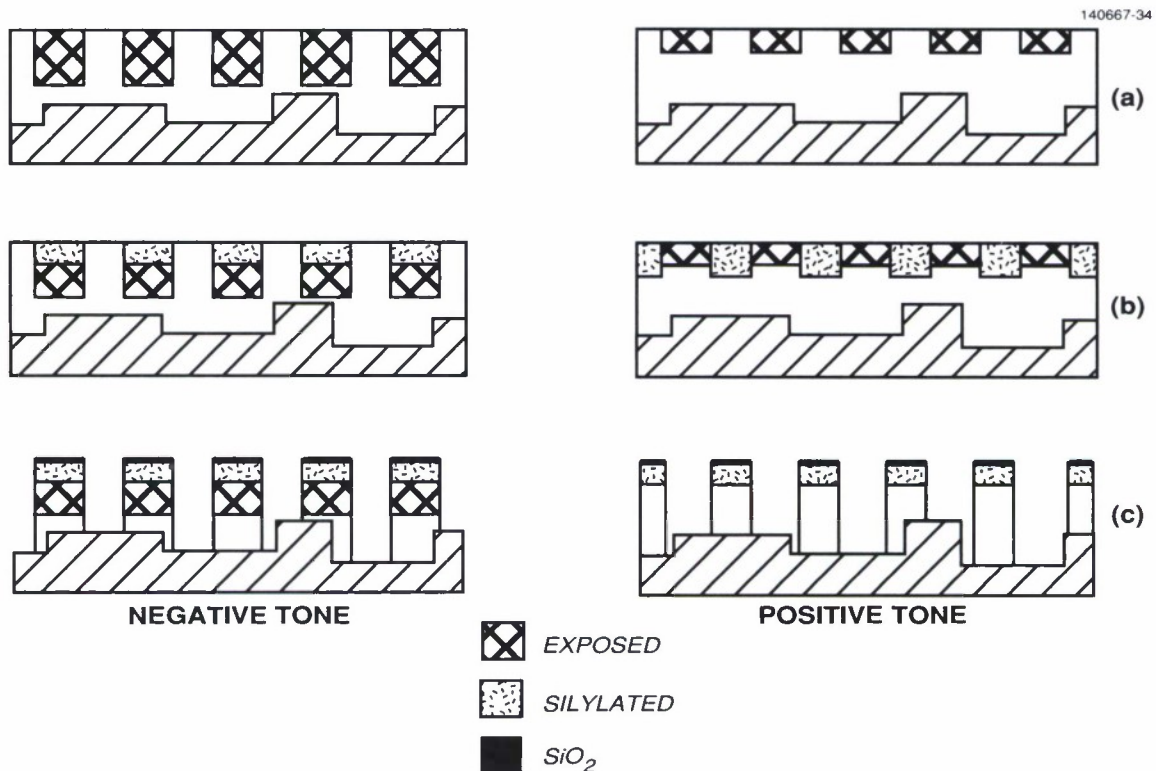


Figure 4-4. Schematic of negative- and positive-tone silylation processes, showing (a) exposure, (b) silylation, and (c) etching steps.



Silylation has been demonstrated [1-3] with *g*-line (436 nm), *i*-line (365 nm), and also recently [4] with KrF excimer laser (248 nm) optical lithography tools. Resolution down to 0.4  $\mu\text{m}$  has been obtained [1,4] in these systems. The silylation step in each instance was performed using hexamethyldisilazane (HMDS) as the silylating agent at temperatures between 140 and 180°C. We have extended the surface-imaging concept to 193-nm lithography with a variety of resists and silylation conditions. The resists included standard novolac/diazoquinone materials such as the Shipley 1400 series and MacDermid PR1024 resist, as well as UCB Plasmask resins designed for silylation (negative tone), a pure novolac resin (Shipley FSC) with no photoactive compound, and a resist system (Shipley SAL 601) designed [5] to catalytically crosslink upon exposure.

It is noted that, unlike long-wavelength exposure, 193-nm irradiation of novolac-based resists primarily causes crosslinking in the surface layers. The crosslinking manifests itself as increased resistance of the exposed areas to silylation under a wide range of reaction conditions (see below). Another effect of the crosslinking is modified dissolution rates of the resist in solvents, as shown in Figure 4-5. Figure 4-5 shows the interferometric traces obtained from a 1.0- $\mu\text{m}$ -thick film of MacDermid PR1024 photoresist developed with AZ 327 metal-ion-free (MIF) developer. The upper trace, which shows the development of an unexposed region, indicates that the film dissolved at a steady rate and was completely cleared in 45 s. The lower trace shows the dissolution of a region of film exposed to 200  $\text{mJ}/\text{cm}^2$ . For the first 250 s, the intensity changed very slowly, indicating a gradual film thinning as the crosslinked area was removed. Once this surface layer had been dissolved, the underlying film was removed in the next 45 s, at the same rate as the unexposed film. The absorption length of 193-nm radiation in novolac resins is typically 50 to 75 nm, and the crosslinked region is of a comparable thickness.

The photoinduced crosslinking and the resultant resistance to silylation imply that silylation of novolac-based resists may be effective at 193 nm mainly in the positive-tone mode (see Figure 4-4). However, as mentioned above, the elevated temperatures at which silylation typically takes place cause thermal crosslinking in the unexposed areas as well, severely reducing the achievable contrast. For instance, the conventional DESIRE process uses HMDS as a silylating agent, at a typical temperature of 160°C [1]. The thermal decomposition of the diazoquinone begins to cause crosslinking at temperatures above 120°C [3]. Novolac/diazoquinone resists could be silylated after 193-nm exposure using HMDS at temperatures between 140 and 160°C, although in several instances insufficient silylation occurred in the unexposed areas to create an etching mask.

As an alternative to HMDS, two silylamine compounds were studied that can be used at temperatures below those causing thermal crosslinking. The reagents were dimethylsilyl-dimethylamine (DMSDMA) and trimethylsilyl-dimethylamine (TMSDMA). The amines are slightly smaller molecules and diffuse more readily into the resist films than HMDS. In addition, they have a higher vapor pressure and may thus be used without needing to heat the reagent source. Typical temperatures for silylation were 100 and 140°C for the DMSDMA and TMSDMA, respectively.



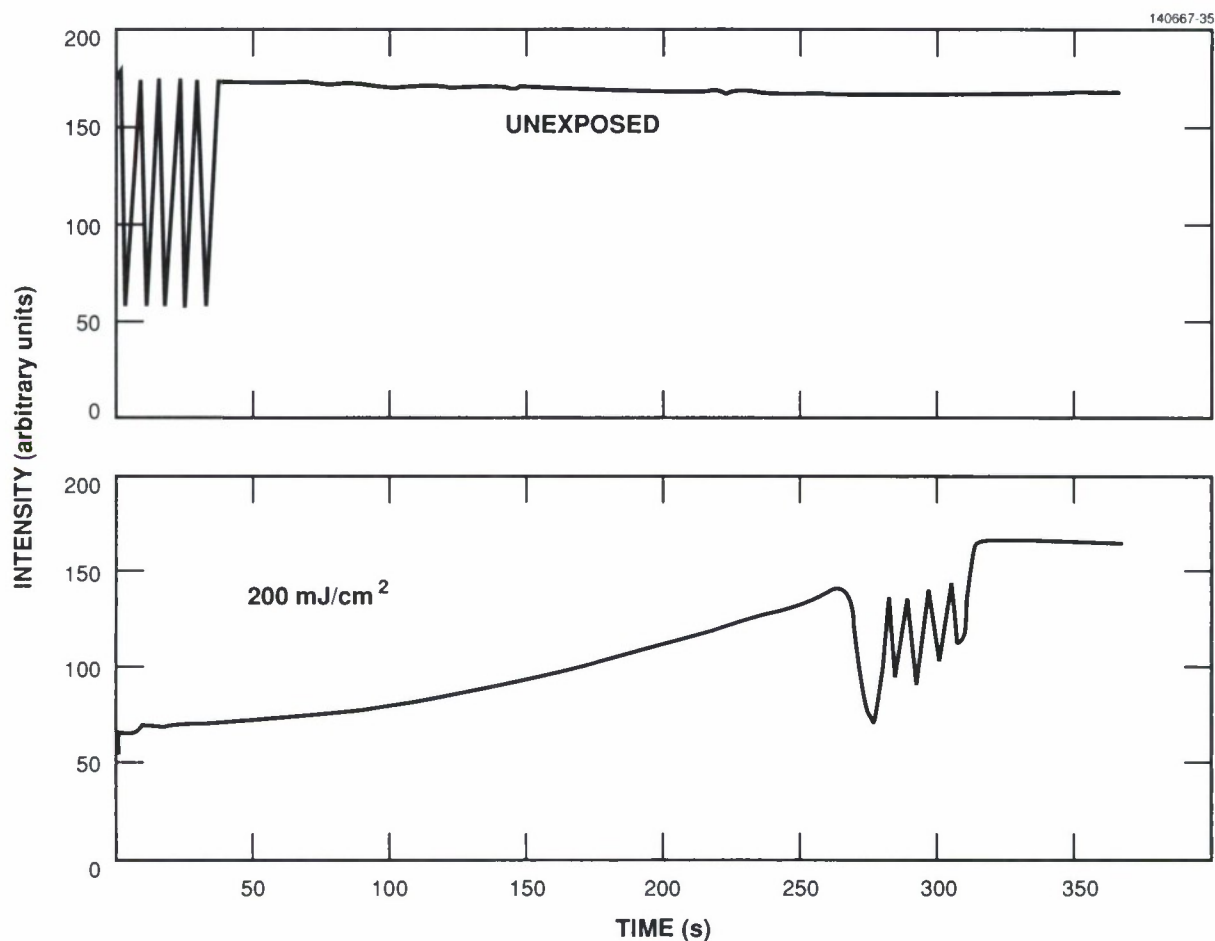


Figure 4-5. Interferometric traces from dissolution of a 1- $\mu\text{m}$ -thick PR1024 resist film in AZ 327 MIF developer. Upper trace is from an unexposed film, while lower trace was exposed to 200  $\text{mJ}/\text{cm}^2$  of 193-nm radiation. The effect of the laser-induced crosslinking is noted as inhibited dissolution for  $\sim 250$  s.

Silylated films were analyzed by Rutherford backscattering spectrometry (RBS) to determine the depth and concentration profiles for the diffused silicon. The RBS spectra for a series of different resists silylated at 100°C for 2 min using DMSDMA showed that the saturation level was comparable for all the materials at around 12 wt.% silicon. There was, however, a noticeable difference between the diffusion depths, which ranged from 81 nm for the 1400-27 resist to the entire film thickness ( $>700$  nm) for the FSC resin. Except for the FSC, all the resists contained diazoquinone and silylated to a lesser depth, indicating that either some crosslinking had occurred even at these relatively low temperatures, or that the diazoquinone inhibited the diffusion and reaction of the silylating agent.

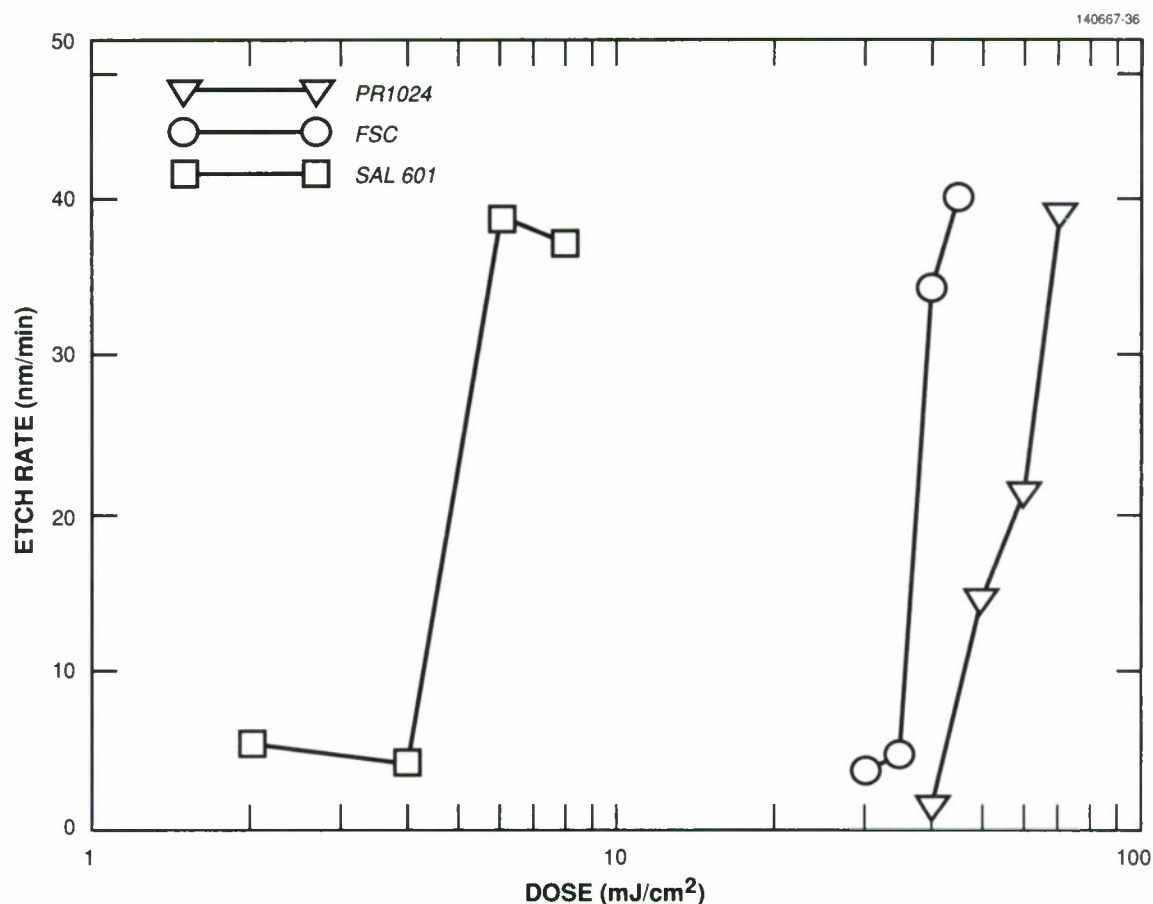
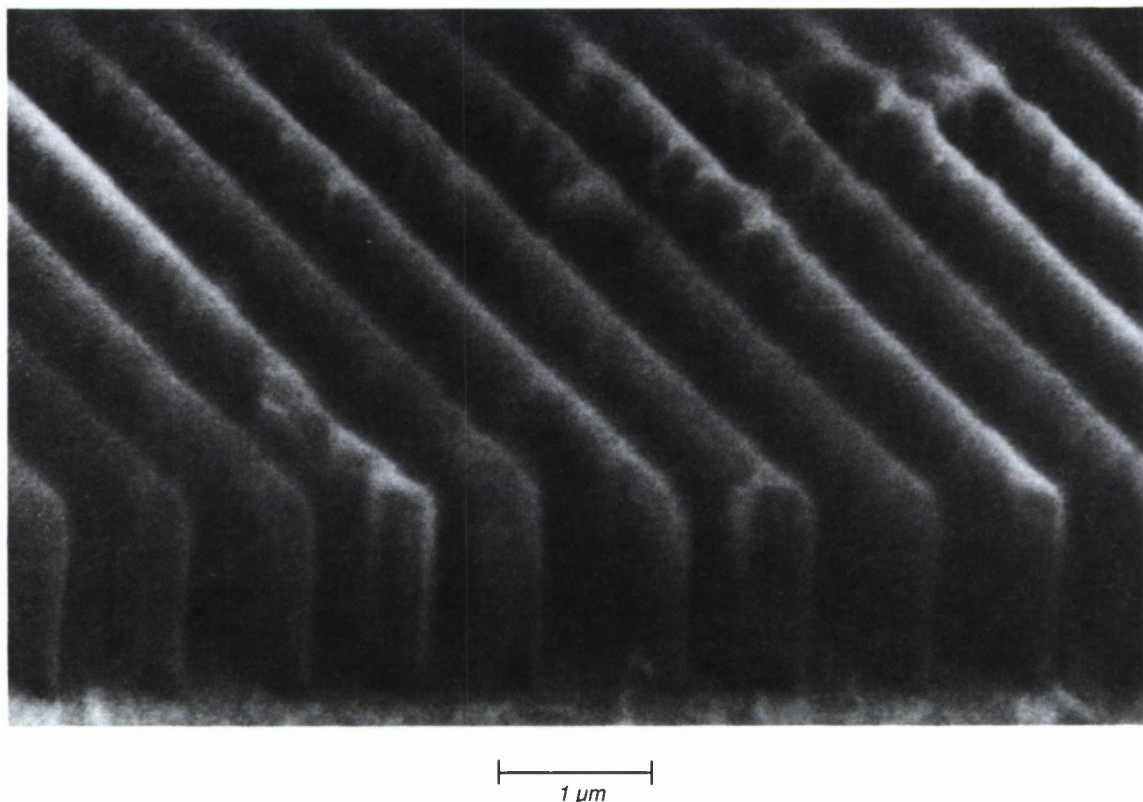


Figure 4-6. Exposure curves showing etch rate in an  $O_2$  RIE plasma as a function of 193-nm exposure dose for SAL 601, FSC, and PR1024 resists. Films were silylated at 100°C for 1 min in 10-Torr DMSDMA, and etched in an  $O_2$  RIE plasma with a bias voltage of -200 V for 20 min.

The combination of photocrosslinking at 193 nm and the development of noncrosslinking silylating conditions makes silylation an attractive lithographic process at this wavelength. In particular, high-resolution patterning is possible, since crosslinking exhibits a sharp, threshold-like behavior as a function of exposure dose. This is shown in Figure 4-6, where the rates of reactive-ion etching (RIE) of silylated films in an  $O_2$  plasma are plotted as a function of exposure dose. As expected, the acid-catalyzed crosslinking material is the most sensitive, with a dose of 6 mJ/cm<sup>2</sup> required to achieve greater than 20:1 etch selectivity. The pure novolac resin, FSC, requires a slightly higher dose of 40 mJ/cm<sup>2</sup>, while the novolac/diazoquinone photoresist PR1024 has a sensitivity of 70 mJ/cm<sup>2</sup>. The contrast for these processes is very high, with values of 4.1, 5.7, and 18 for the PR1024, SAL 601, and FSC, respectively. Further work has indicated that the crosslinking appears to be reciprocal with laser fluence.



*Figure 4-7. Scanning electron micrograph of 0.4- $\mu\text{m}$  lines and spaces in FSC resist exposed at 60  $\text{mJ}/\text{cm}^2$  of 193-nm radiation. Films were silylated at 100°C for 1 min in 10-Torr DMSDMA, and etched in an  $\text{O}_2$  RIE plasma with a bias voltage of -200 V for 40 min.*

The applicability of silylation schemes to 193-nm lithography is demonstrated in Figure 4-7. Here, 0.4- $\mu\text{m}$  lines and spaces are patterned in a film of FSC at a dose of 60  $\text{mJ}/\text{cm}^2$ . The film was silylated at 100°C for 1 min using DMSDMA and etched in an  $\text{O}_2$  RIE plasma at a bias of -200 V for 40 min.

In summary, silylation processes were extended to 193-nm lithography. Positive-tone patterning was obtained by combining exposure-induced crosslinking with the development of different silylation procedures that preserve the selectivity introduced by the laser exposure. Photoactive compounds are not necessary for the crosslinking to take place, and in fact, diazoquinone appears to hinder the silylation process. Dose and fluence requirements are compatible with specifications for proposed 193-nm exposure equipment, and imaging capabilities below 0.5  $\mu\text{m}$  have been demonstrated.

M.A. Hartney  
K. Stoy-Pavelle

## REFERENCES

1. B. Roland, R. Lombaerts, C. Jakus, and F. Coopmans, Proc. SPIE **771**, 69 (1987).
2. R.-J. Visser, J.P.W. Schellekens, M.E. Reuhman-Huisken, and L.J. van Ijzendoorn, Proc. SPIE **771**, 111 (1987).
3. B. Roland, J. Vandendriessche, R. Lombaerts, B. Denturck, and C. Jakus, Proc. SPIE **920**, 120 (1988).
4. S. Das, H. Gaw, and R. Hollman, KTI Microelectronics Seminar Interface '88, San Diego, California, 9-10 November 1988.
5. M. deGrandpre, K. Graziano, S.D. Thompson, H. Liu, and L. Blum, Proc. SPIE **923**, 158 (1987).



## 5. MICROELECTRONICS

### 5.1 IMPROVED PROCESS FOR THINNED, BACK-ILLUMINATED CCD IMAGING DEVICES

Thinned, back-illuminated charge-coupled device (CCD) imagers offer significant advantages over front-illuminated counterparts, including greatly increased quantum efficiency in the blue-ultraviolet (UV) spectral region, and excellent spatial uniformity. These advantages have made back-illuminated CCD imagers a very desirable choice for many applications [1,2], including use in Lincoln Laboratory's multichip focal-plane-array projects. Unfortunately, the use of back-illuminated CCD imagers has been hindered in the past either by incompatibilities between the wafer mounting and thinning procedures and standard wafer processing steps [1,2] or by difficulties in passivating the exposed back surface after fabrication [3]. We describe here an improved wafer mounting, thinning and laser-annealed back surface passivation process that produces mechanically rugged, back-illuminated thinned imagers with the above advantages but without perturbing the original processing steps of front-illuminated CCD imagers.

The process sequence is illustrated in Figure 5-1. These fabrication steps will convert any  $p$ -on- $p^+$  epitaxial wafer with fully fabricated and probe-tested front-illuminated CCD imagers to a wafer of back-illuminated devices. The mounting process is accomplished first by spinning epoxy on the front side of the device wafer, which is then attached to a supporting silicon wafer or glass substrate [Figure 5-1(a)]. Next, a two-step thinning process, developed to minimize pitting on the etched surface, is performed [Figure 5-1(b)]. The variation in thickness of the thinned silicon is controlled to within  $1\ \mu\text{m}$  by ultrasonic agitation ( $\sim 0.2\ \text{W}/\text{cm}^3$ ) during the etching process. After back surface doping and laser annealing, explained below, an antireflection coating and aluminum light shield are applied [Figure 5-1(c)]. Finally, the wafer is completed by photolithography and etching of Si and  $\text{SiO}_2$  to expose the undersides of the aluminum pads on the front side of the wafer [Figure 5-1(d)].

Thinned imagers with an unpassivated back surface have high dark current and unstable spectral response. To suppress the excess dark current and achieve stable spectral response, a shallow  $p^+$  accumulation layer is formed on the back surface. Under thermal constraints resulting from Al-metallization and epoxy layers on the front side, irradiation with a pulsed KrF excimer laser, leading to superficial melting of the exposed back surface of the silicon, is used to activate the low-energy (5 keV) implanted  $\text{BF}_2$  dopant without damage to the front surface. Figure 5-2 shows the sheet resistivity vs the laser energy density at two different doping levels. The sheet resistivity cannot be measured for laser energy density lower than  $0.3\ \text{J}/\text{cm}^2$ , indicating that the dopant is not activated below this level. Bright spots start to appear on the dark current pattern for irradiation energy density higher than the damage threshold, which is around  $0.6\ \text{J}/\text{cm}^2$ . The carrier concentration profile of the  $p^+$  accumulation layer doped at  $10^{14}\ \text{cm}^{-2}$ , as measured by spreading resistance, is shown in Figure 5-3. Figure 5-4 shows the activation level as well as the depth of the peak carrier concentration vs the number of pulses at  $0.56\ \text{J}/\text{cm}^2$ . The optimized process using four overlapping pulses at  $0.56\ \text{J}/\text{cm}^2$  completely suppresses the excess dark current due

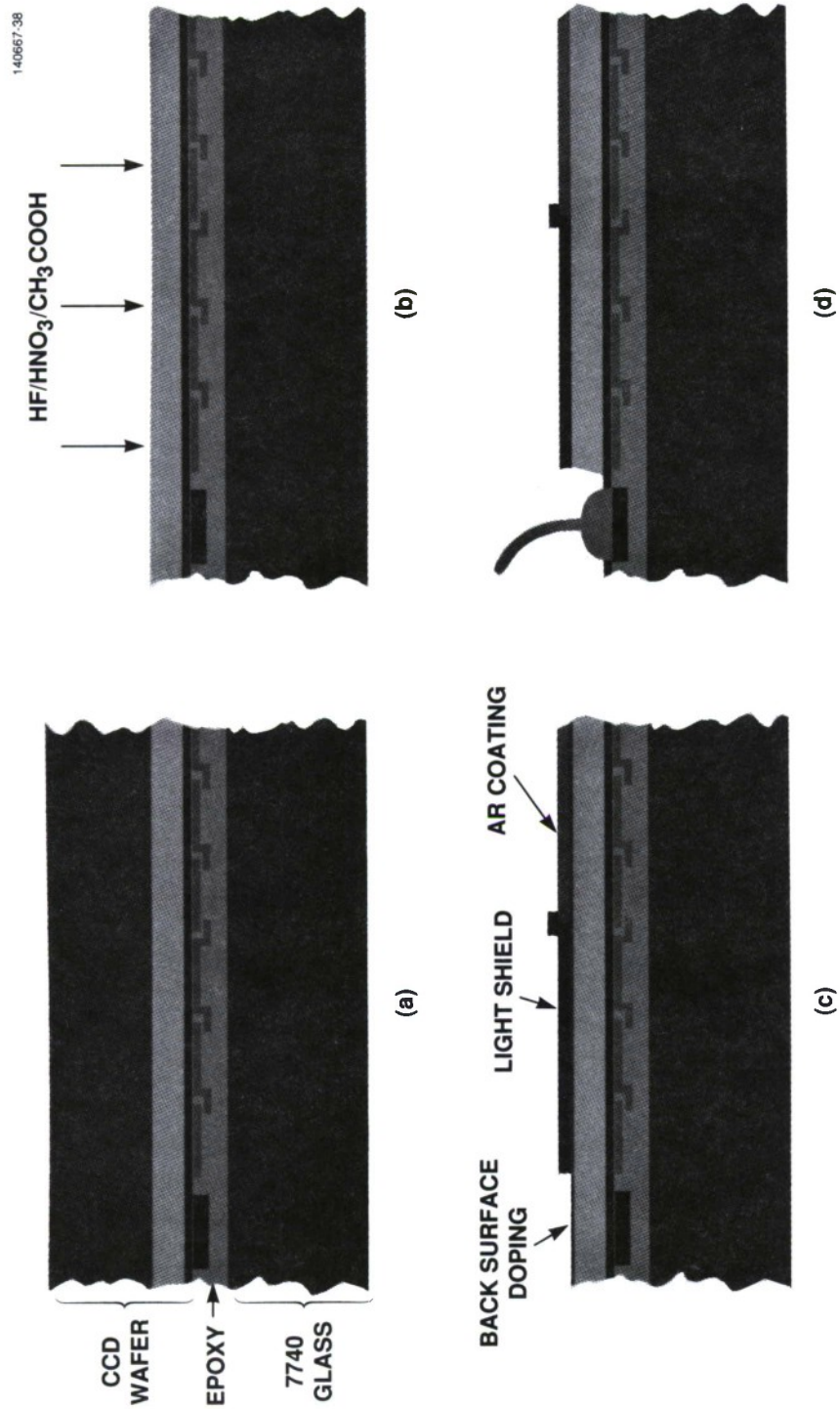


Figure 5-1. Back-illuminated CCD imager fabrication sequence: (a) wafer mounting to glass substrate, (b) selective etching to thin Si wafer down to epilayer, (c) back-surface processing, and (d) etching Si and SiO<sub>2</sub> to expose bonding pads.

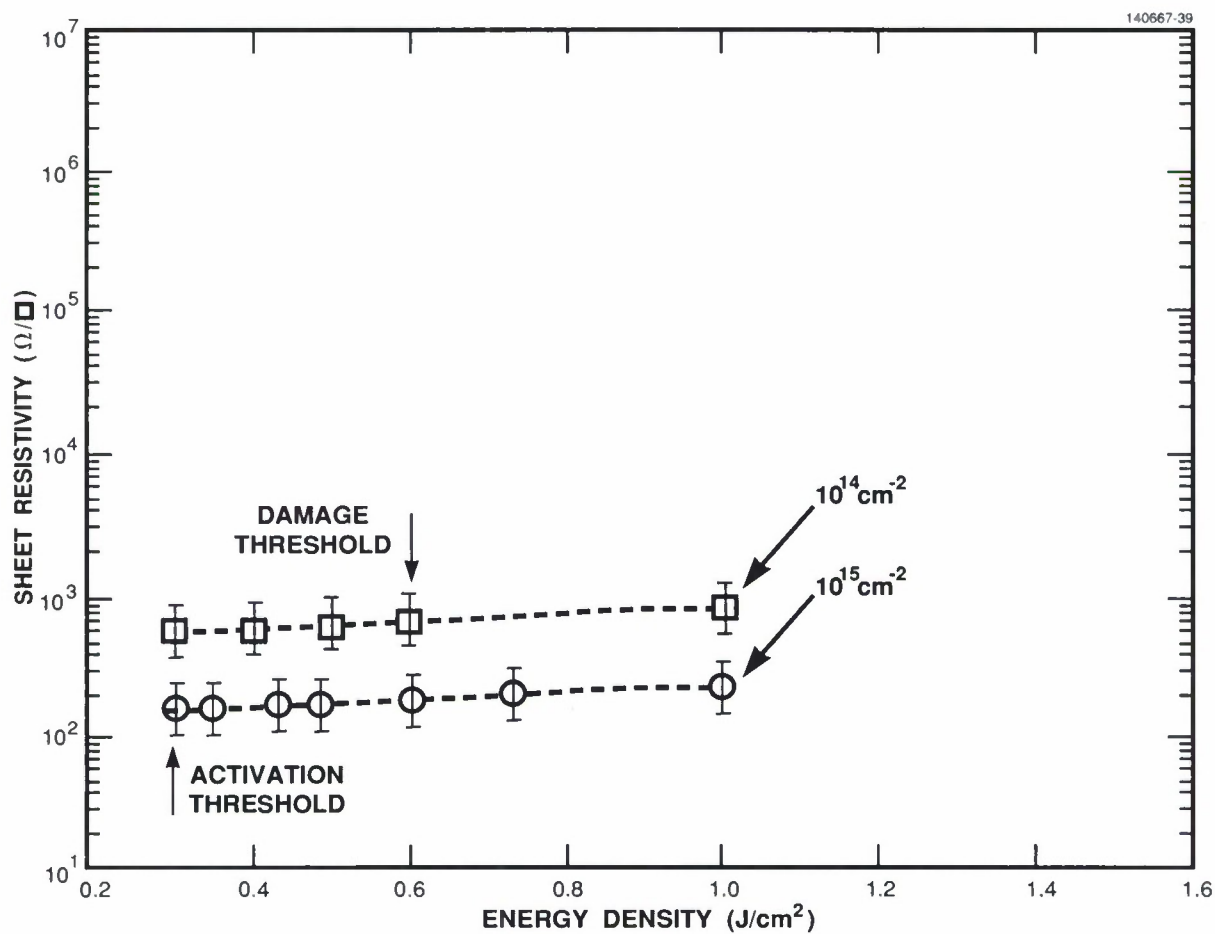


Figure 5-2. Dependence of sheet resistivity on laser energy density for two different levels of  $\text{BF}_2$  implantation.

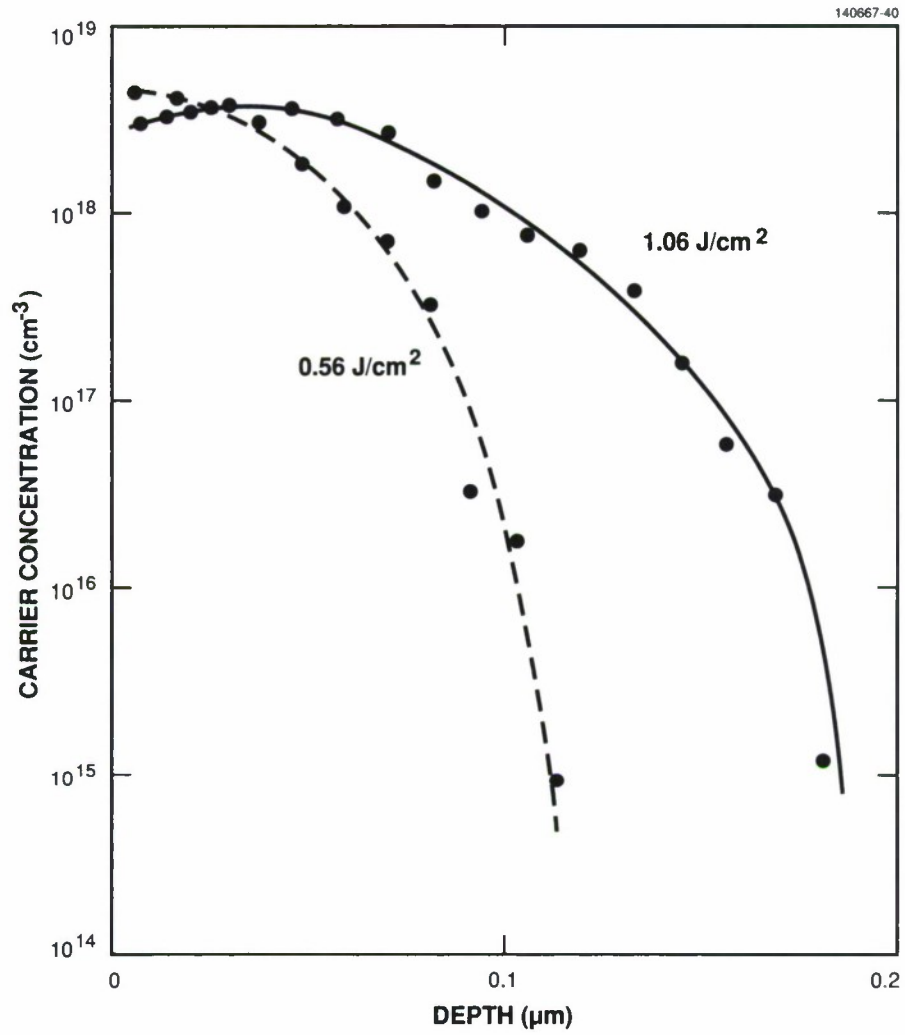


Figure 5-3. Doping profiles of the shallow accumulation layer formed by ion-implanted laser-annealed process.



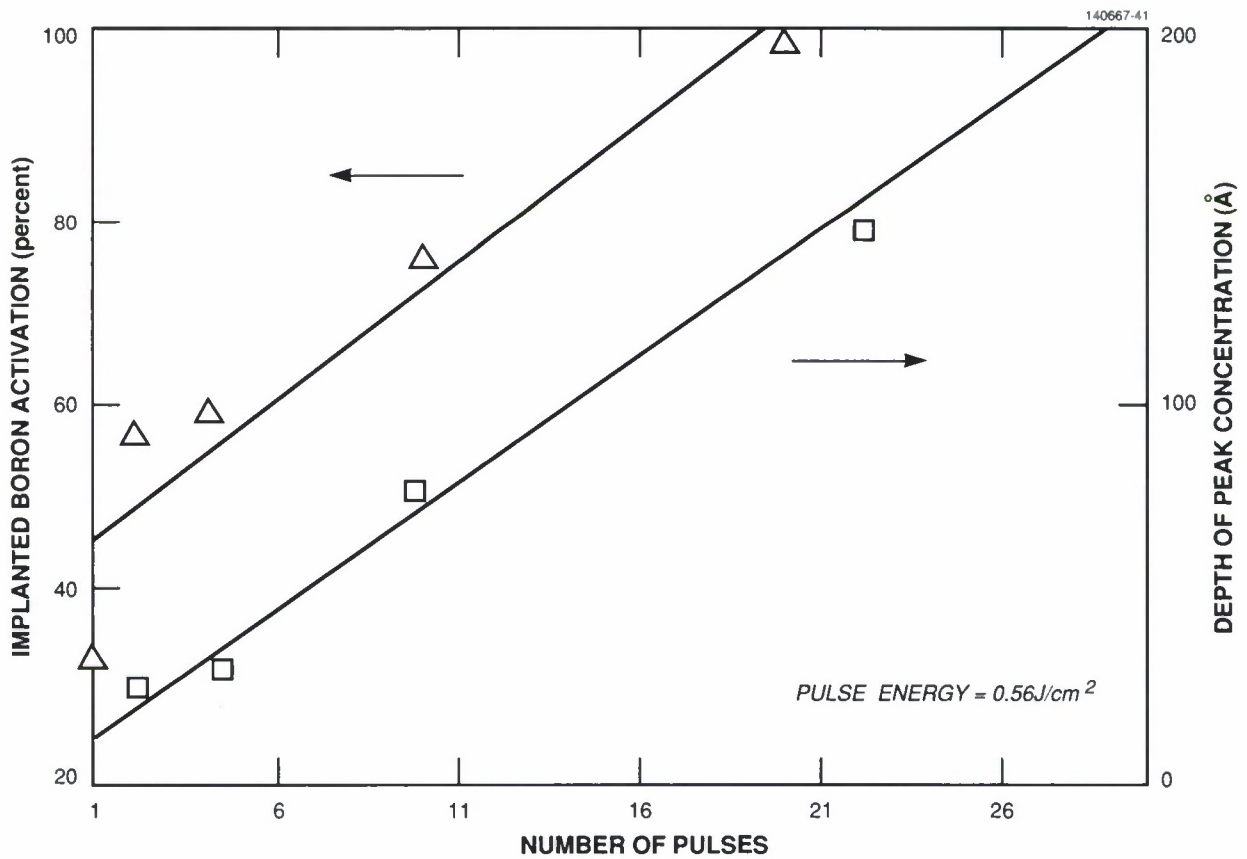
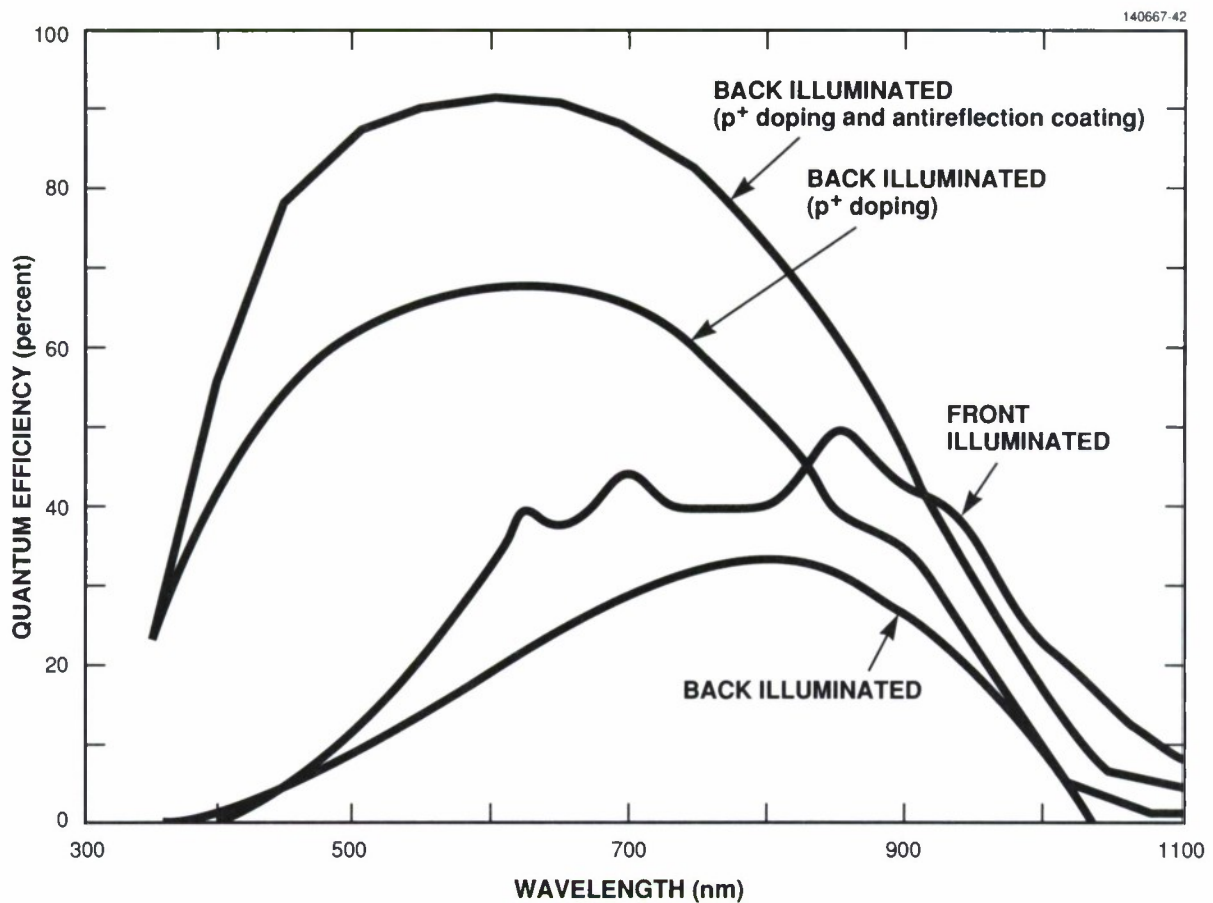


Figure 5-4. Activation of implanted boron and depth of peak carrier concentration vs number of irradiating laser pulses.



*Figure 5-5. Quantum efficiency of front-illuminated and back-illuminated CCDs with and without back passivation.*

to the thinned, unpassivated back surface, restoring the current to the level observed in front-illuminated imagers. Spectral response that is stable over time is achieved with this treatment. Figure 5-5 shows the measured quantum efficiency with and without back surface passivation. None of the other parameters such as the readout noise and the charge transfer efficiency (CTE) is degraded in the thinned device.

C.M. Huang	B.B. Kosicki
B.E. Burke	R.W. Mountain
G.A. Lincoln	E.D. Savoye

## 5.2 PROTON IRRADIATION OF CCD IMAGING DEVICES

As part of the radiation hardening program, CCD imaging devices and bulk Si wafers were irradiated with high-energy (MeV) protons and the resulting damage was characterized. The CCDs showed increased dark current and reduced CTE. There is some evidence that a small background charge will reduce the latter of these problems. Studies of bulk Si wafers indicate that the present effort to increase substrate resistivity will also result in a more proton-resistant CCD.

Several of the missions that will use Lincoln Laboratory CCD imagers in low earth orbit expose the devices to as much as 5 krad of high-energy protons over the mission life. In order to determine the effects of proton irradiation on these devices, functioning CCDs were irradiated at the Harvard Cyclotron Laboratory with either monoenergetic protons or a spectrum ranging in energy from 5 to 180 MeV. The exposures were between 100 and 10,000 rad of protons, corresponding to roughly  $5 \times 10^8$  and  $1 \times 10^{11}$  protons/cm<sup>2</sup>, respectively. At levels as low as 100 rad some effects on CTE could be seen, with CTE decreasing by about 70 ppm at a temperature of  $-65^\circ\text{C}$  in the imaging array. The effect of fluence on CTE loss appears to be linear, so a dose of 5 krad would decrease CTE to about 0.996, a very significant loss in the ability of the CCD to handle small charge packets. At  $-40^\circ\text{C}$ , however, the CTE was substantially improved, and images with charge packets as small as 60 electrons could be readily discerned even after 10-krad exposure. It appears that at this higher temperature a uniform background dark charge (36 electrons/pixel/frame in this case) keeps the trapping centers filled and reduces charge transfer loss. For reasons that are not yet understood, all decreases in CTE are confined to the imaging array and do not extend to the serial register. Dark current measurements, performed at  $-65^\circ\text{C}$  (the operating temperature of the different CCDs will range between  $-65$  and  $-40^\circ\text{C}$ ), indicate an increase in the dark current of about 2 fA/cm<sup>2</sup>-rad.

These changes in the CCD characteristics are probably due to the creation of point defect complexes as the protons course through the Si. These defects would increase the number of generation centers in the bulk, thereby increasing the dark current, and would also increase the number of electron traps, which would decrease the CTE. It is quite possible that the same defect influences both properties. In order to determine the effect of protons on the bulk characteristics of Si, bare Si wafers were irradiated with 10 krad of either 20- or 150-MeV protons. Tentatively, it appears that there is no difference in the change in minority carrier lifetime, as measured by surface photovoltage, for either energy (although 20-MeV protons produce much more damage than 150-MeV protons) or for either float zone or Czochralski Si. There is also the suggestion that higher levels of dopant decrease the hardness of the Si (although this change is not directly proportional to doping concentration), and that *n*-type Si is more susceptible to damage than *p*-type Si. The change in lifetime corresponds well to the change in dark current seen at  $-65^\circ\text{C}$ , and if we assume a recombination cross section of  $1 \times 10^{-15}$  cm<sup>2</sup>, then this suggests that we generate  $4 \times 10^9$  cm<sup>-3</sup> sites/rad of protons, a number which is in general agreement with past work on neutron bombardment of bulk Si.

Work is in progress to minimize the susceptibility of our CCD using an appropriate combination of operating temperature and clock rate (these parameters influence the ability of traps to decrease CTE), shielding requirements, starting material, and novel processing techniques that could reduce the volume

of the signal channel occupied by small electron packets, thus decreasing the volume over which traps could be filled.

J.A. Gregory	D.C. Harrison
B.E. Burke	M.W. Bautz
M. Cooper	

### 5.3 CCD NEURAL NET PROCESSOR

A generic CCD signal processor based on an algorithm for computing vector-matrix products, and which can be used as a one- or two-dimensional matched filter and a two-layer neural net computing module [4], has been designed and fabricated. Used as a neural net processor, the chip provides 2016 programmable interconnections between 144 input nodes and 14 output nodes, performs 2.8 billion arithmetic operations per second and dissipates <2 W at 10-MHz clock rate.

The block diagram of this neural net processor is shown in Figure 5-6. In order to make the device a generic processor, and also for faster data input, a design approach was taken so the 144 inputs are loaded and stored in six CCD shift registers, each 24 stages long. Associated with each of the 144 stages of these six registers is a CCD multiplying digital-to-analog converter (MDAC) [5] and a 14-stage 6-bit digital memory for shifting and holding the digital connection weights  $w_{ij}$ . At each stage of the CCD shift register, the floating gate is coupled to the analog input port of the corresponding MDAC. The output from each MDAC is a charge packet proportional to the product of the analog input and the digital connection weight. The outputs of all the MDACs are summed together in the charge domain.

The architecture of the digital connection-weight memory is shown in Figure 5-7. For each MDAC, there is a 14-word bit-parallel CCD digital memory to store the connection weights. The digital data are written into the memory using a 24-stage column pointer and a 6-stage row pointer to enable the selected location to receive data. The pointers consist of on-chip digital shift registers, along which a single bit is propagated, therefore selecting adjacent memory locations sequentially. The memory is designed so that one of the 14 preloaded weight vectors, each consisting of 144 6-bit digital words, is read out and applied to all 144 MDACs in parallel. The next memory-register clock pulse then reads out and applies the next memory vector to the MDACs, and so on for all 14 vectors. A low-power, high-packing-density CCD digital shift register has been used in this design for each memory register. Use of the normally volatile CCD device is possible in this case because the digital data are continuously read and rewritten into the memory, and are refreshed by providing feedback from the output to the input of the register.

In operation, weights  $w_{ij}$  are preloaded into  $14 \times 144$  digital memory locations, and a set of 144 analog inputs  $x_i$  is read in. Then, each of the 14 144-word bit-parallel CCD digital memory vectors is sequentially applied to the MDACs as described above. After the first shift register clock period, the total summed charge from all the MDACs is  $\sum_{i=0}^{143} w_{i0}x_i$ , i.e., the device computes the first output of the second layer,  $u_0$ . After the second clock period, the total summed charge is  $\sum_{i=0}^{143} w_{i1}x_i$ , that is,  $u_1$ . The procedure continues for 14 clock periods in total, thereby computing all 14 values of  $u_i$ . This computation function is common to many neural net models. For example, this device can be used with external circuitry to select the maximum of the output values and to enhance this maximum by adjusting the weights according to learning rules. Larger nets with more than two layers may be composed of multiple devices.



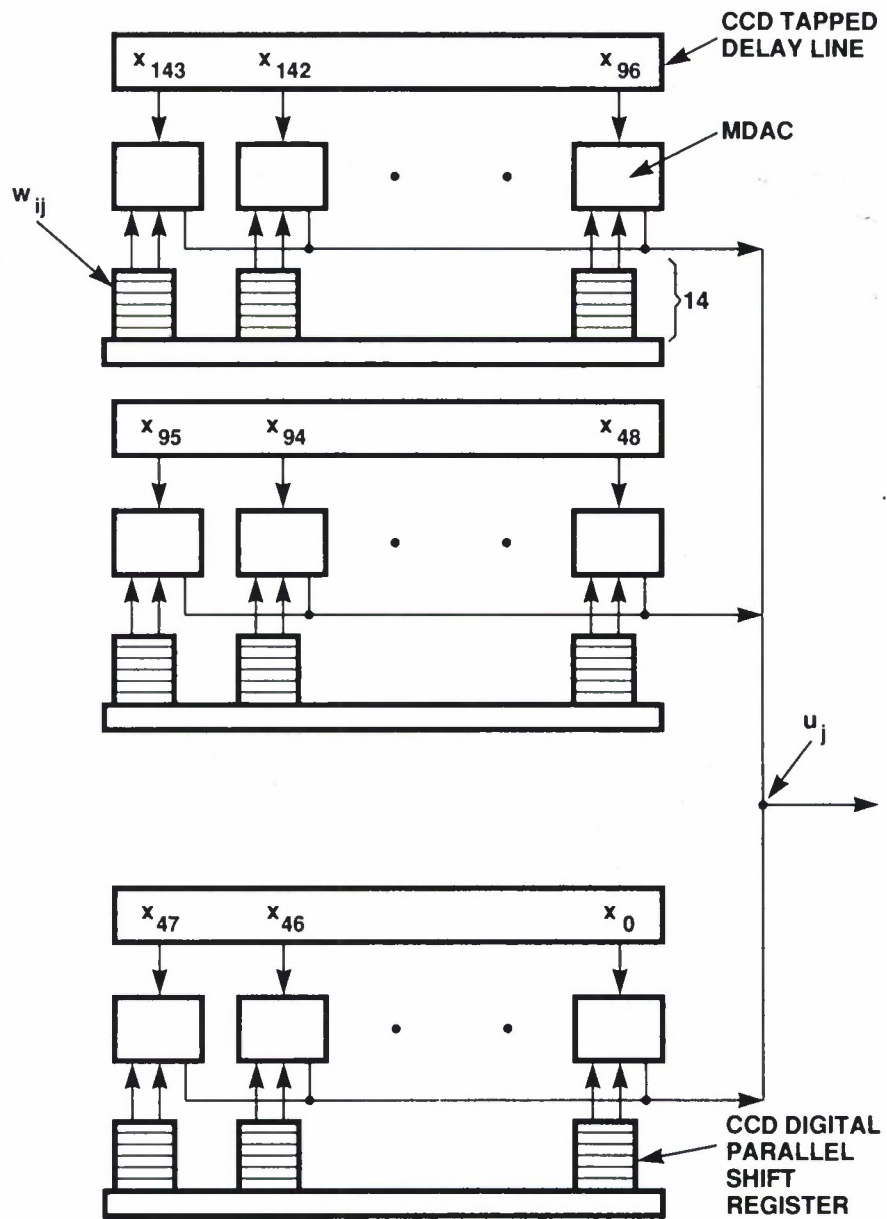


Figure 5-6. Block diagram of CCD neural net device.

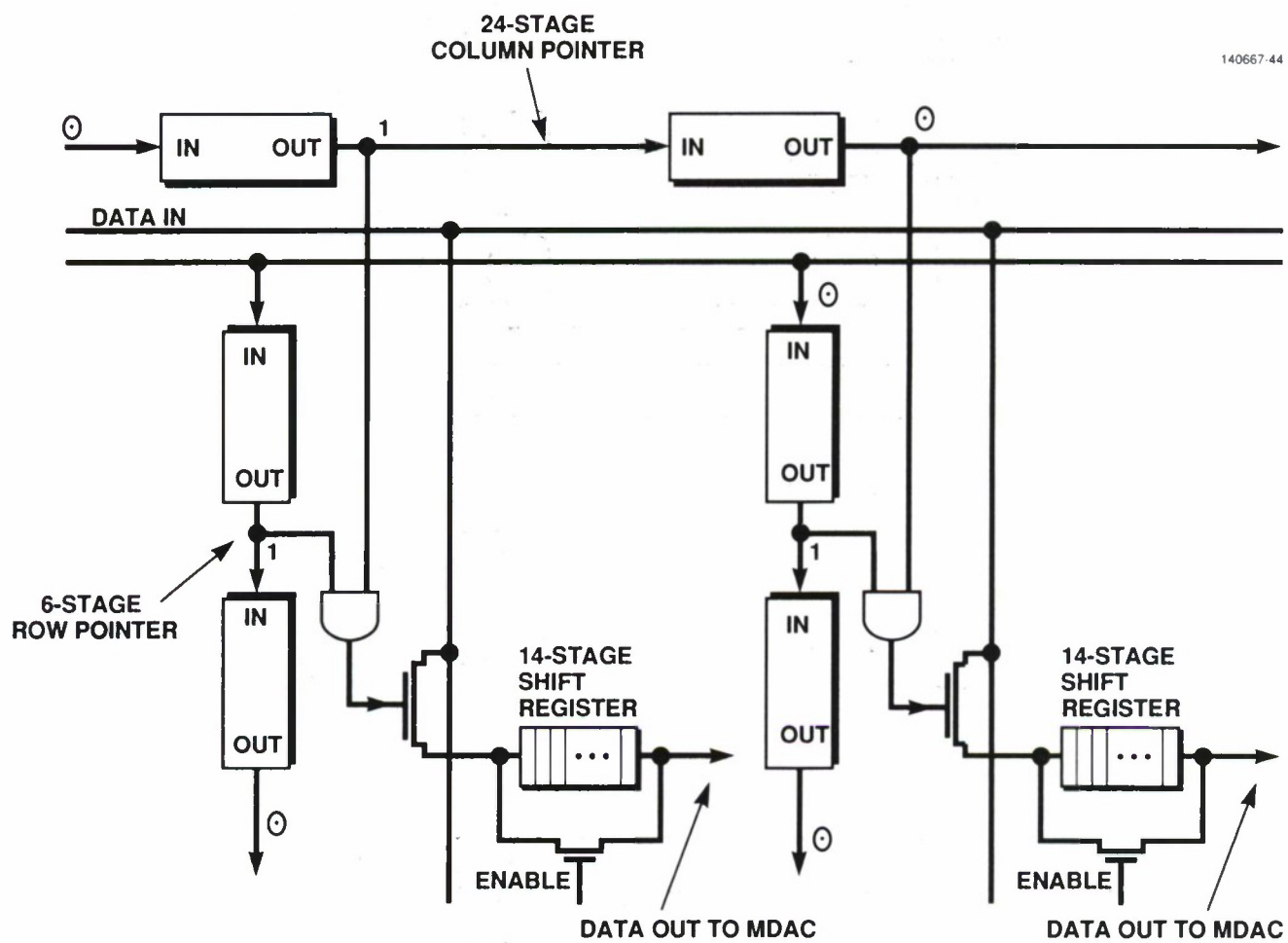


Figure 5-7. Architecture of digital connection-weight memory.

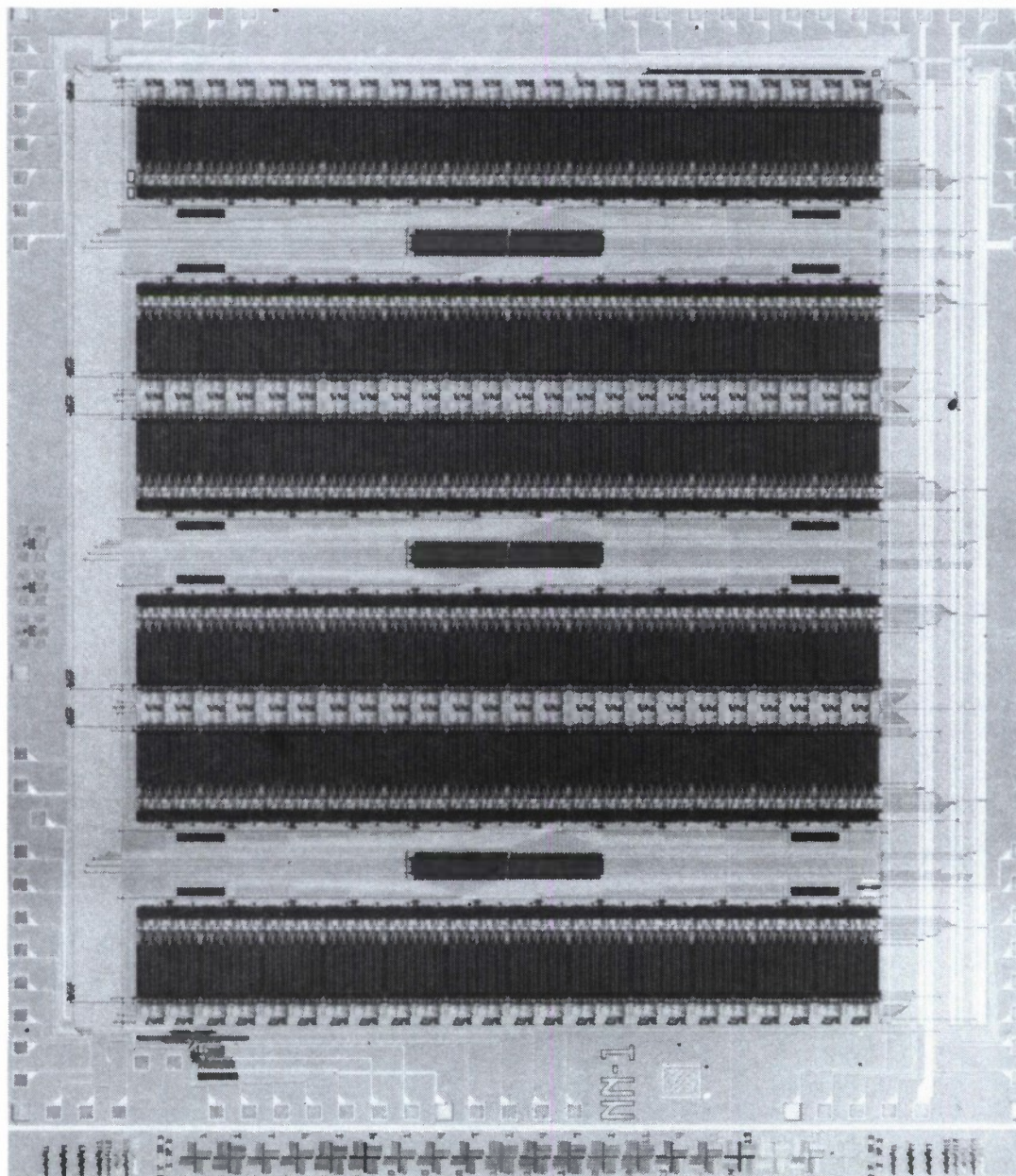


Figure 5-8. Photomicrograph of the neural net device.

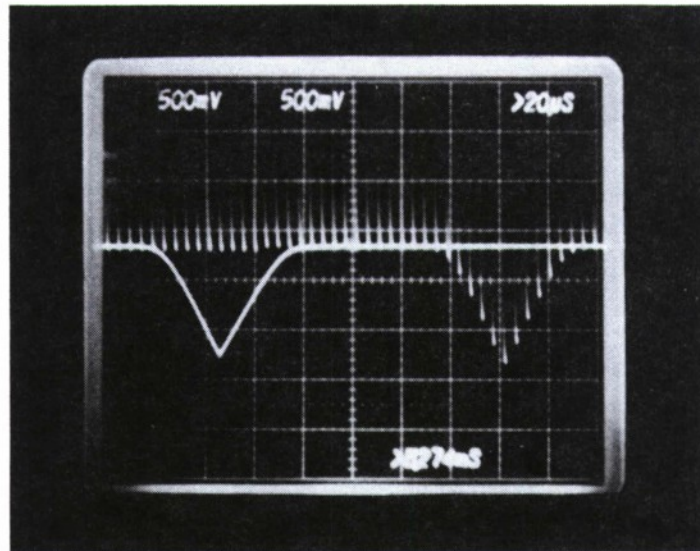


Figure 5-9. Input and output signals of a tapped delay line. The output is nondestructively sensed at tap 25 of a 48-stage delay line.

A photomicrograph of the neural net chip is shown in Figure 5-8. A 3- $\mu\text{m}$  double-polysilicon, double-metal CCD process was used, and the chip area is  $7 \times 7$  mm. The functionality of each component of the processor has been tested and demonstrated. For example, the performance of one of the on-chip CCD tapped delay lines is shown in Figure 5-9, demonstrating the input-output linearity. More detailed device characterization is currently being carried out.

A.M. Chiang	G.A. Lincoln
R.W. Mountain	J.R. LaFranchise
J.H. Reinold	

## REFERENCES

1. S.R. Shortes, W.W. Chan, W.C. Rhines, J.B. Barton, and D.R. Collins, *Appl. Phys. Lett.* **24**, 565 (1974).
2. E.D. Savoye, *Proc. SPIE* **570**, 95 (1985).
3. J.R. Janesick, *IEDM Tech. Dig.* (IEEE, New York, 1986), p. 350.
4. J.L. McClelland and D.E. Rumelhart, *Psychol. Rev.* **88**, 375 (1981).
5. A.M. Chiang, R.W. Mountain, D.J. Silversmith, and B.J. Felton, *ISSCC Tech. Dig.* (IEEE, New York, 1984), p. 110.



## 6. ANALOG DEVICE TECHNOLOGY

### 6.1 MICROWAVE DIELECTRIC PROPERTIES OF EVAPORATED SILICON MONOXIDE AT 4.2 K

The need for compact delay lines for signal processing devices requires thin dielectric films (2 to 5  $\mu\text{m}$ ) with low microwave loss. In particular, in support of the signal processing devices that we are developing, such as the time-integrating correlator [1], these dielectric films need to be deposited on niobium-coated silicon substrates. The processing temperature must be  $<300^\circ\text{C}$  to minimize both inter-diffusion of niobium and silicon and possible chemical reactions between the niobium and deposition compounds.

In the literature [2], the dielectric constant of evaporated  $\text{SiO}$  has been reported at liquid-helium temperature to be 5.7 in the 10- to 20-GHz range and nondispersive. However, the dielectric loss of  $\text{SiO}$  has not been reported previously at these frequencies. As the substrate temperature during evaporation can be maintained at  $<120^\circ\text{C}$ , this material is therefore a good candidate for signal processing applications.

We have recently fabricated a microstrip transmission-line resonator with a superconducting thin-film metallization in order to evaluate the dielectric properties of an evaporated film of silicon monoxide. A cross section of the device is shown in Figure 6-1(a). A film of silicon monoxide was evaporated to a thickness of 5  $\mu\text{m}$  onto a silicon substrate coated with a 3000- $\text{\AA}$  sputter-deposited niobium film. The stress in the silicon monoxide film was low and it adhered well to the niobium-coated substrate, even after repeated thermal cycling to liquid-helium temperature. On this surface a second 3000- $\text{\AA}$  niobium film was patterned into a 10- $\mu\text{m}$ -wide line as shown in Figure 6-1(b). This pattern resulted in a transmission-line resonator with a resonant frequency determined by the length of the line between the 1- $\mu\text{m}$  end gaps. The resonance condition is satisfied for line lengths equal to an integral number of half-wavelengths.

The fundamental resonant frequency of this structure was measured to be 1320 MHz. Knowing that the length of the resonant transmission line is 5.3 cm, we determine that the wave velocity in this structure was 1/2.14 times the speed of light in vacuum, giving an effective dielectric constant equal to 4.6. In the microstrip configuration shown in Figure 6-1(a), this wave velocity is strongly influenced by the air above the device structure, in addition to the dielectric property of the silicon monoxide itself. Taking this into account, we can deduce that the relative dielectric constant of the silicon monoxide is 6.2 at 4.2 K and 1.3 GHz. The measured quality factor of this resonator is 7500 at the same frequency, so the effective loss tangent ( $\tan \delta$ ) of the mixed dielectric is  $1.3 \times 10^{-4}$ . If the conductor loss is assumed to be negligible, this number represents a lower bound on the material (silicon monoxide) loss tangent. Simple energy and field-strength arguments, with consideration of the value of the effective dielectric constant, put the upper bound at  $1.5 \times 10^{-4}$ .

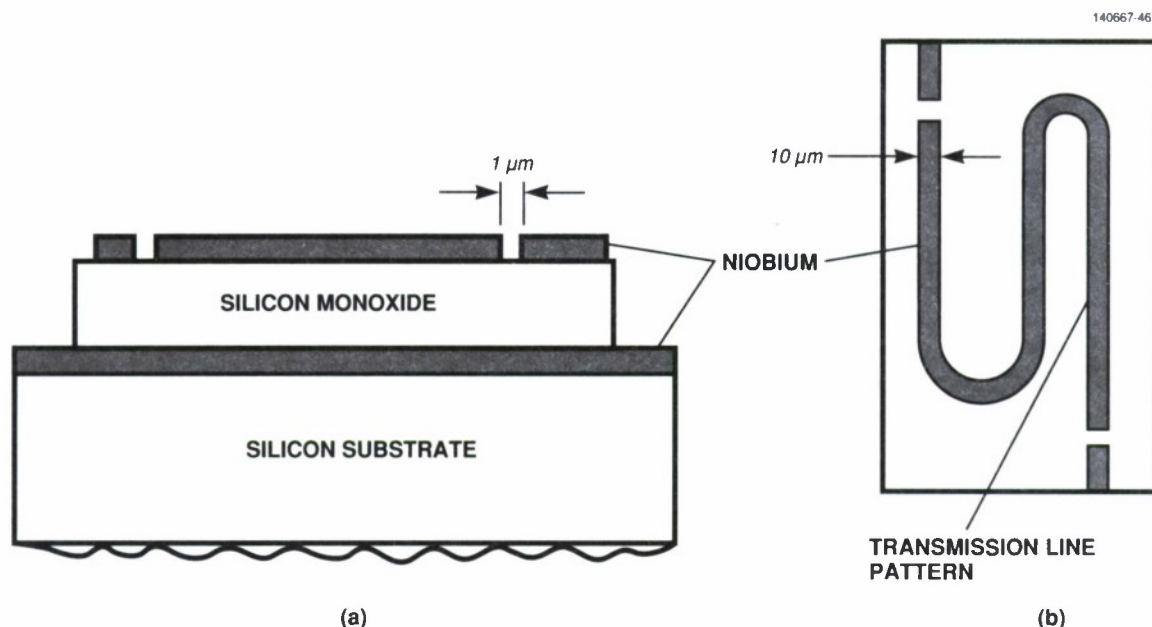


Figure 6-1. (a) Cross-sectional view of microstrip resonator with deposited silicon monoxide dielectric. (b) Top view of the microstrip resonator showing patterned niobium microstrip transmission line.

As the insertion loss (in decibels) for a transmission at frequency  $f$  on a line of propagation time  $\tau$  is given approximately by  $27f\tau \tan \delta$ , we see that the SiO dielectric can support microstrip lines up to 100 ns long, with a tolerable loss of  $<3$  dB at 8 GHz.

J.B. Green  
M. Bhushan

## 6.2 ANALYSIS OF THE EFFECT OF COUNTERDOPING IN THE GAPS OF A SINGLE-GATE-LEVEL CCD PROCESS

A key parameter of the basic cell of charge-coupled devices (CCDs) is the separation between adjacent electrodes. For efficient charge transfer, the gap has to be small to provide strong coupling between adjacent potential wells. In earlier CCDs, in which the separation was defined photolithographically, the gap was large (a few micrometers) and the charge transfer efficiency (CTE) was poor. Subsequent development led to the two- or three-level poly-Si gate structure, with overlapping gates separated by thermally grown poly-Si oxide [3]. With this multi-poly-Si process, the interelectrode gap can easily be kept under  $0.4 \mu\text{m}$ . Unfortunately, the two- or three-level process is not compatible with state-of-the-art processes; in addition, the parasitic capacitance of the overlapping electrodes is not desirable in high-speed CCDs.

There are several approaches to producing nonoverlapping electrodes made of a single level of poly-Si. We have found that by using a traditional projection aligner with some process improvements, CCDs with a 0.8- $\mu\text{m}$  gap are readily achievable. However, testing of these single-poly-Si CCDs has shown, not surprisingly, that the relatively large gap results in a very poor CTE. We suggest a very simple processing step (counterdoping in the gap) to significantly reduce the charge trapped in the interelectrode region and to increase the CTE of these 0.8- $\mu\text{m}$ -gap CCDs. A detailed analysis of CCD operation has been made, and the effect of the counterdoping has been predicted.

It is well known that, in buried-channel (BC) CCDs, the charge trapped in the interelectrode potential troughs can be a major source of charge transfer inefficiency. In the single-poly-Si CCDs the interelectrode region is accessible and can be ion implanted. To determine the effect (if any) of an interelectrode implant, we have solved Poisson's equation in two dimensions and obtained the minimum potential in the channel and the electron concentration under the different conditions that are typical of the operation of our CCDs. Since we are mainly concerned with the interelectrode region, we analyzed a structure with only two electrodes,  $\Phi_1$  and  $\Phi_2$ , separated by a distance  $G$  (Figure 6-2). The substrate is  $p$ -type, and the profile of the BC is shown in Figure 6-3.

The CCDs (imagers) operate with three-phase, 0- to 12-V clocks. The clock timing is schematically shown in Figure 6-4. The simulated channel potential when the wells are empty is shown in Figure 6-5. When  $t = t_1$  the gate voltages are  $\Phi_1 = 0$  V and  $\Phi_2 = 12$  V. The fringing fields between the two electrodes are strong enough to control the interelectrode region, despite the large gap. When the two electrodes are at the same potential ( $t = t_3$  and  $t = t_4$ ), the potential trough is maximum. During the transfer,  $\Phi_2$  clocks from 12 to 0 V ( $t = t_2$ ). The simulations show that, for  $\Phi_1 = 0$  V and  $\Phi_2 < 10$  V, there is a potential trough in the interelectrode region where charge could be trapped. The transfer to the next well,  $\Phi_3$ , would then be incomplete and the CTE would be poor. These results are, at least qualitatively, consistent with our expectations.

Simulations with charge in the wells showed an unexpected and potentially serious problem with this CCD design. Figure 6-6 shows the potential of the BC well in a cross section under an electrode with  $\Phi_2 = 12$  V, for different signal packets  $Q_n$ . The corresponding charge distribution is shown in Figure 6-7. We see that for  $Q > Q_4$  some of the charge is touching the interface. In practice the imagers operate with a maximum signal of  $Q_3$  ( $10^6$  electrons) so the charge under the electrodes is always safely confined in the BC, away from the surface. In the gap region, however, the situation is very different. The surface potential is not completely controlled by the electrodes and tends to float down to the channel potential (Figure 6-8). Even for a small charge packet, the potential well becomes very shallow or even completely flat, as in the extreme case shown here ( $\Phi_1 = \Phi_2 = 12$  V). Consequently, even for small packets, the charge will touch the interface in the gap region (Figure 6-9). Qualitatively, we know that this will contribute to noise and to an additional degradation of the CTE, caused by surface-state trapping and by a reduction of the mobility. Without a full transient analysis we cannot predict how much charge will be at the interface during the transfer or estimate the magnitude of this degradation.

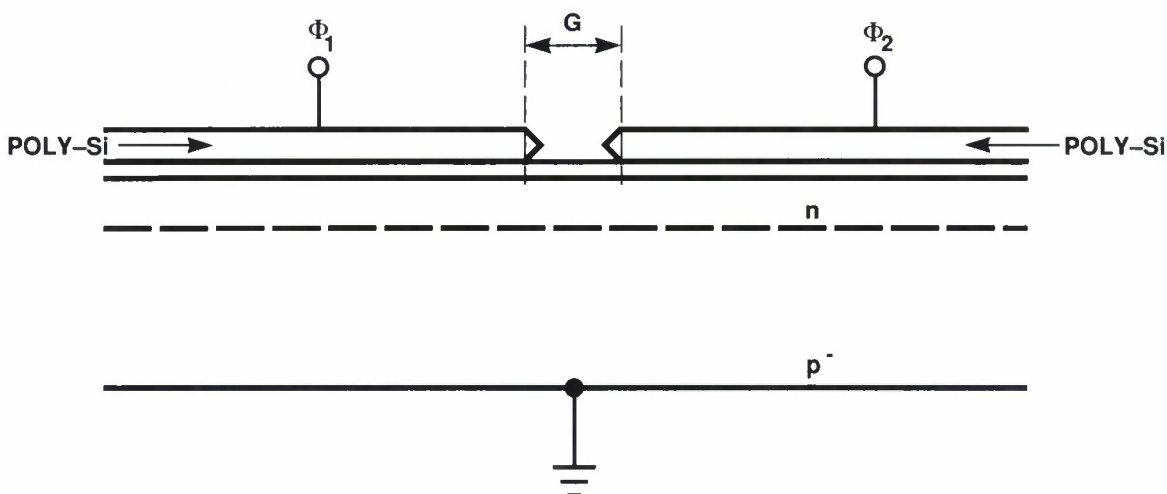


Figure 6-2. Single-poly-Si CCD structure; only two electrode phases are shown.

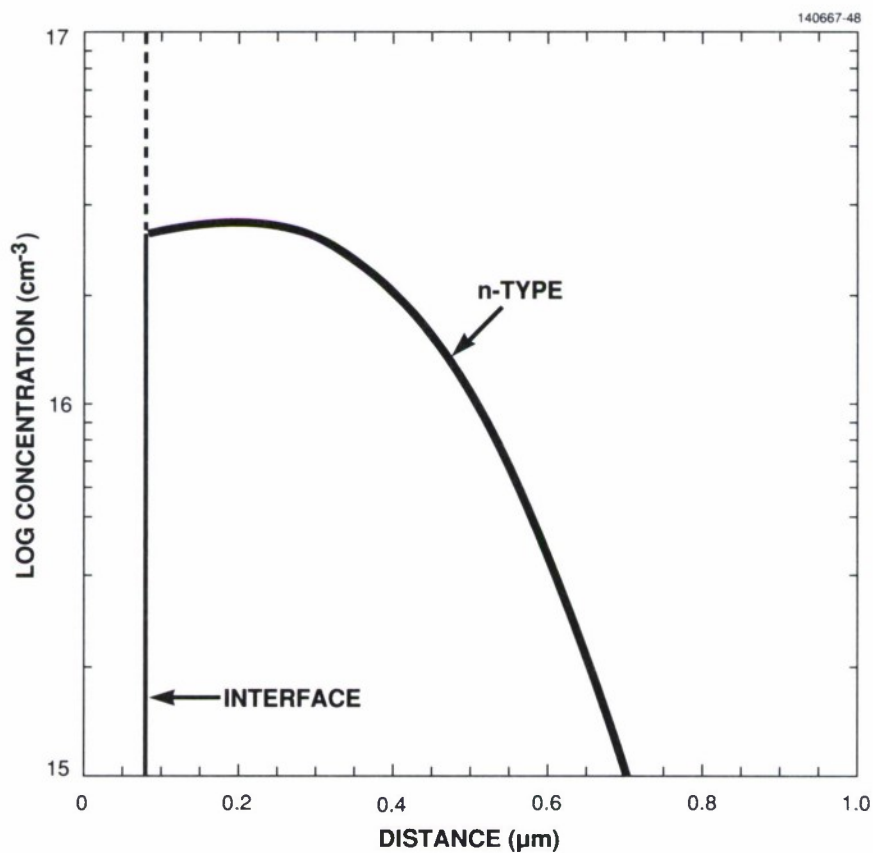


Figure 6-3. Concentration of the BC donor implant.



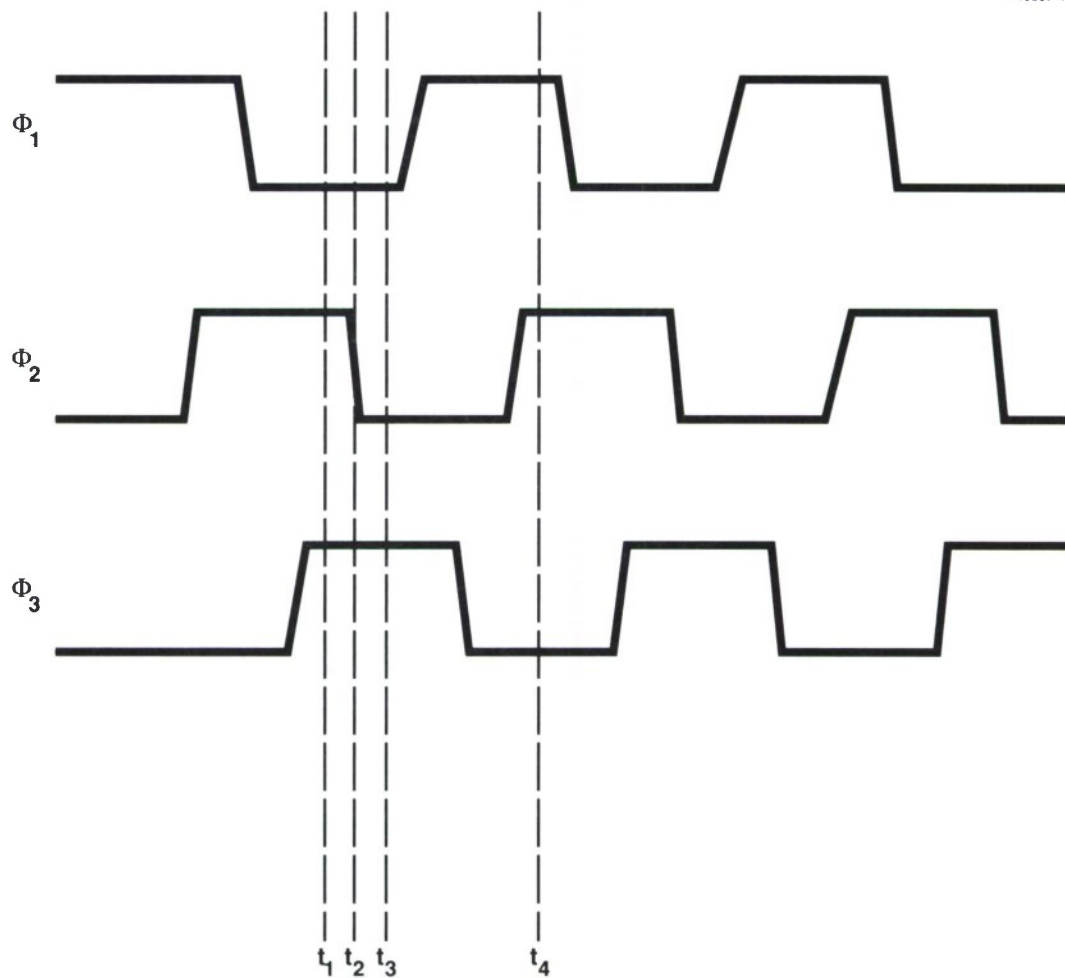


Figure 6-4. Timing diagram for three-phase CCD structure. High levels are attractive to electrons (more positive gate voltage).

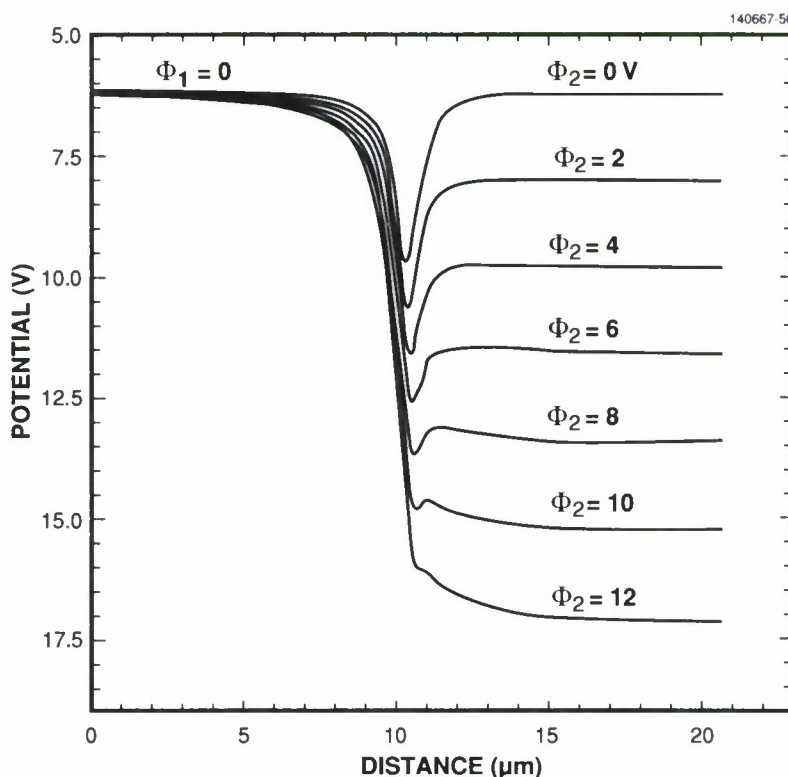


Figure 6-5. Calculated potential minimum (taken across depth) of empty wells as a function of lateral position for different gate voltages.

To improve the CTE in the single-poly-Si imagers we propose to implant the interelectrode region with a *p*-type implant (boron). This counterdoping will have two effects. First, by raising (making less negative) the threshold in the gap region, the potential trough will be reduced; second, if the counterdoping profile is chosen judiciously, it can create a barrier that will exist even as the surface floats and will confine the charge in the channel away from the interface.

Simulations confirm these assumptions and show that the exact boron profile and dose are not critical. Without attempting to optimize the boron implant, we have chosen a profile (Figure 6-10) that creates a shallow *p*-type layer at the surface in order to create a permanent barrier near the surface. Its dose is just large enough to reduce the potential trough, as too much boron could not only pin the surface to the substrate potential but also create potential “bumps.” The channel potential when the wells are empty is shown in Figure 6-11. The plot is identical to Figure 6-5 except in the gap region, where there

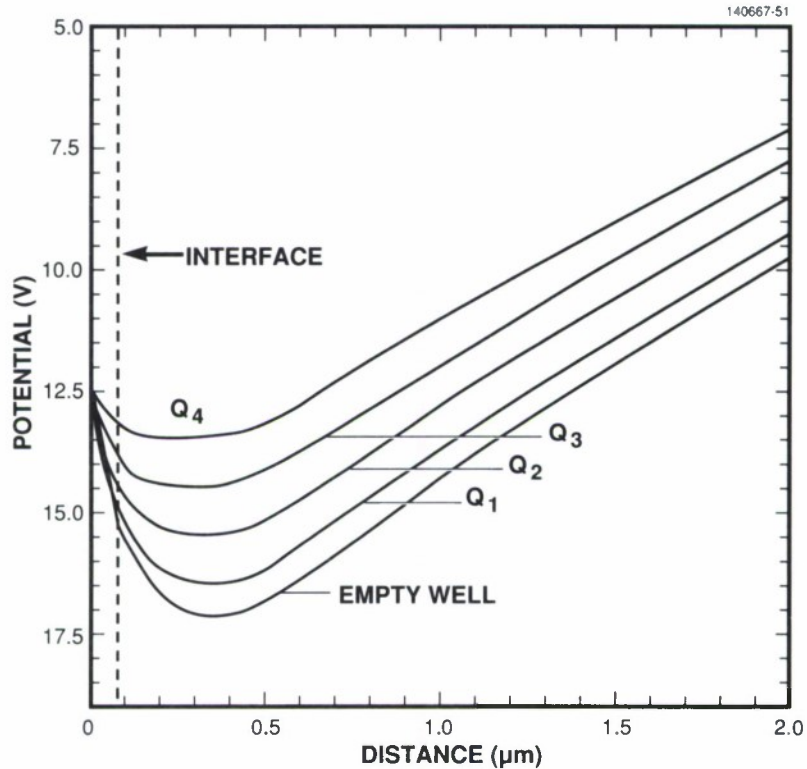


Figure 6-6. Calculated potential of the BC well as a function of depth in a cross section under an electrode with  $\Phi_2 = 12$  V for different charge packets  $Q_n$ .

is a significant reduction of the potential trough. A plot of the potential in the cross section of the gap (Figure 6-12) shows that, even if the surface floats down with the channel potential as the charge is increased, the curves are not completely flat and the bending keeps most, if not all, of the charge away from the interface (Figure 6-13).

These results are encouraging and show that the boron implant in the gap region can be used to improve the CTE in single-poly-Si CCDs. We are currently fabricating single-poly-Si imagers with different gap widths and with different boron profiles. We will then verify this analysis experimentally and determine the optimum interelectrode implant.

A.L. Lattes  
C.M. Huang

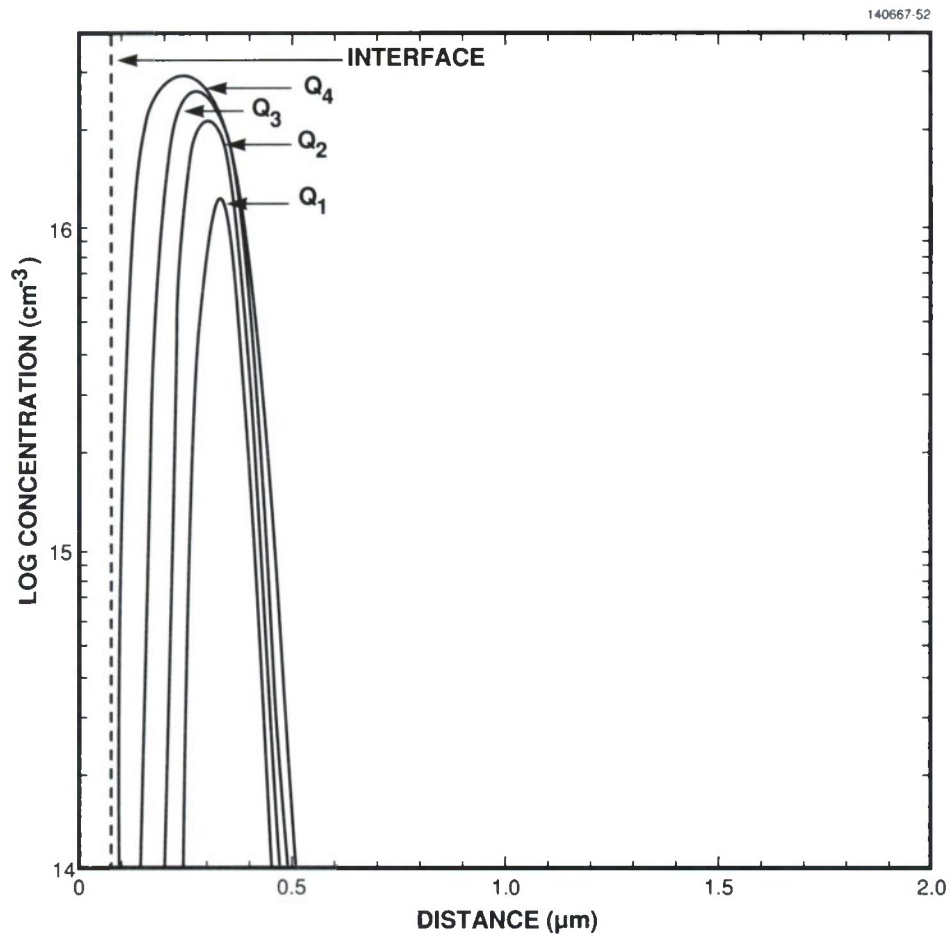


Figure 6-7. Spatial mobile charge distribution as a function of depth under a gate corresponding to the curves in Figure 6-6.



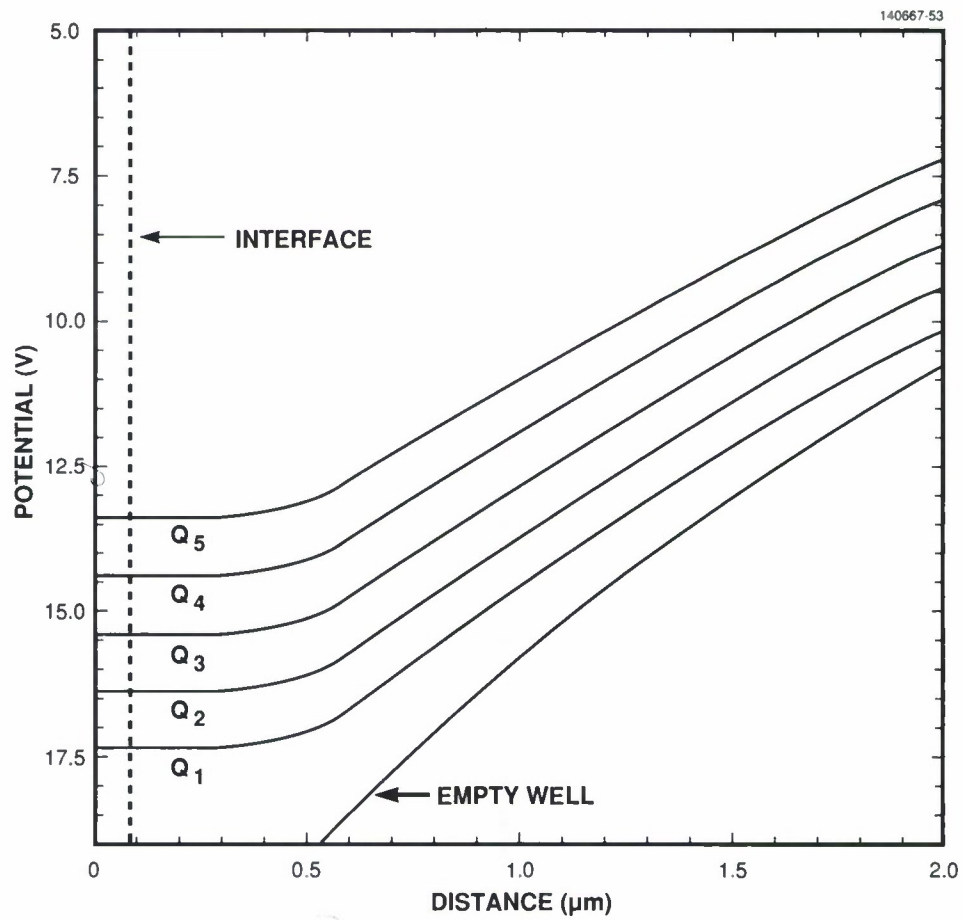


Figure 6-8. Calculated potential as a function of depth in a cross section in the gap region for different charge packets.

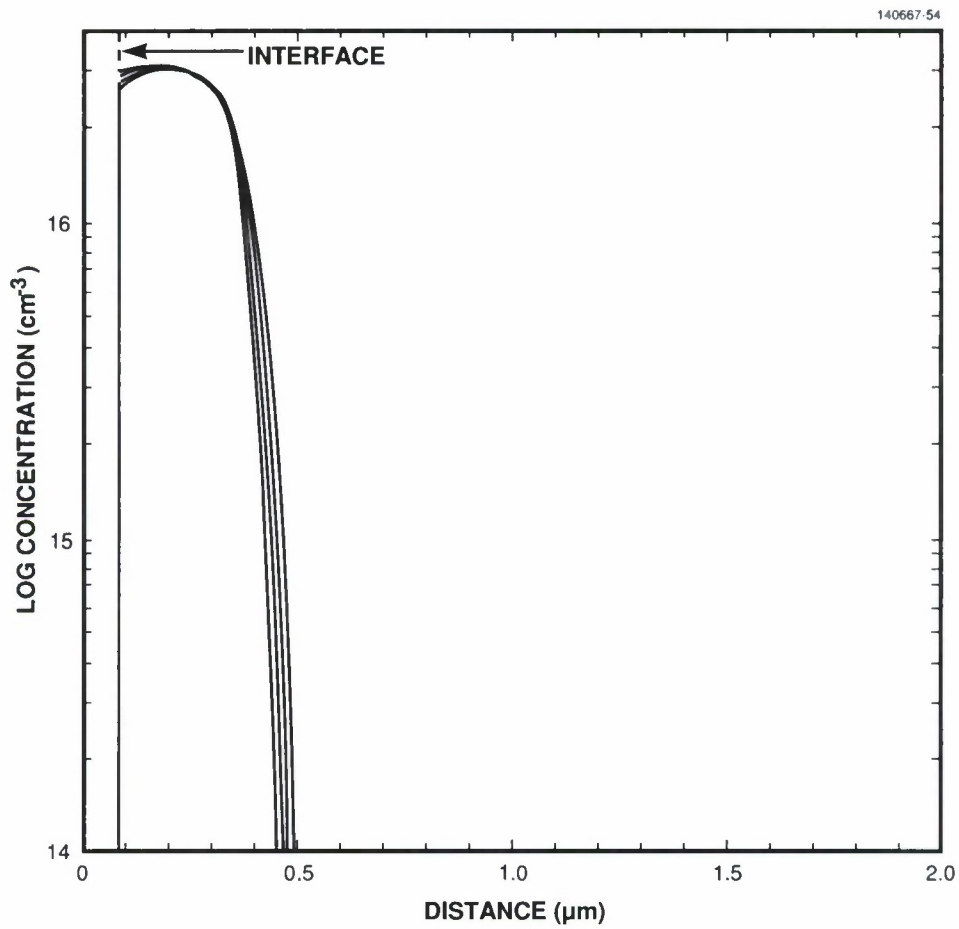


Figure 6-9. Spatial mobile charge distribution as a function of depth corresponding to the curves in Figure 6-8.

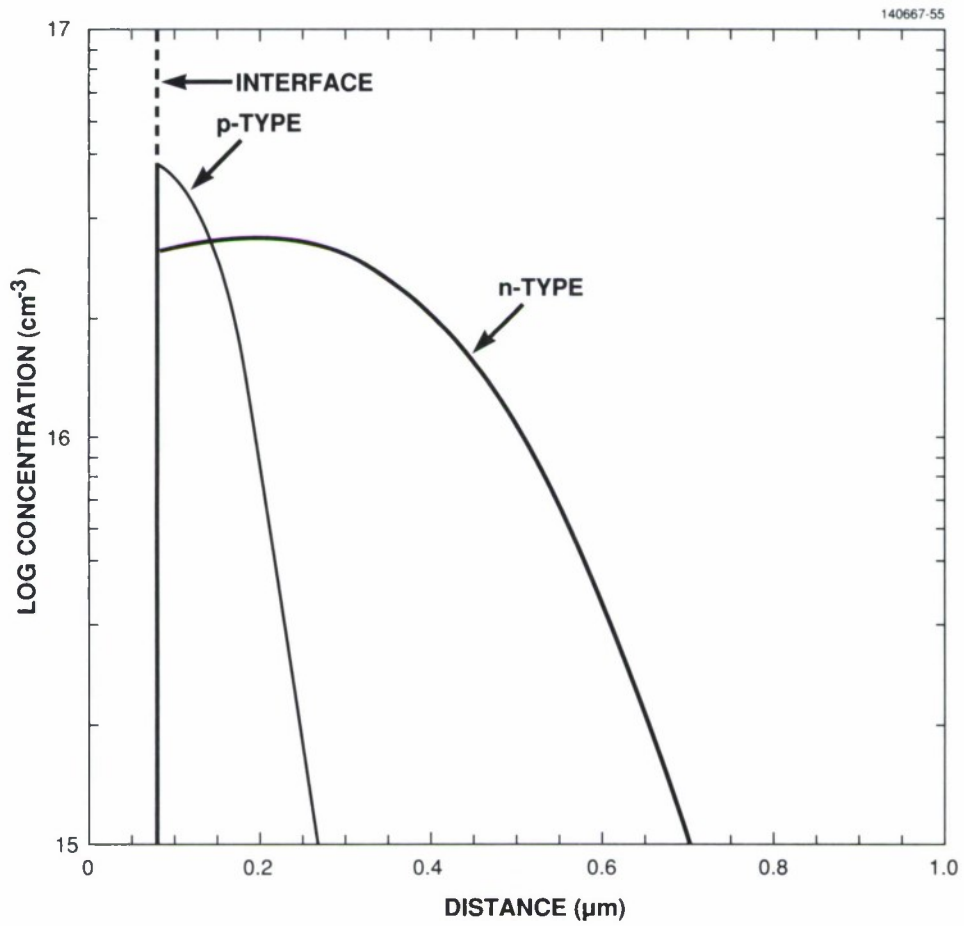


Figure 6-10. Channel doping profile to reduce the potential trough: n-type BC and p-type shallow counterdoping.

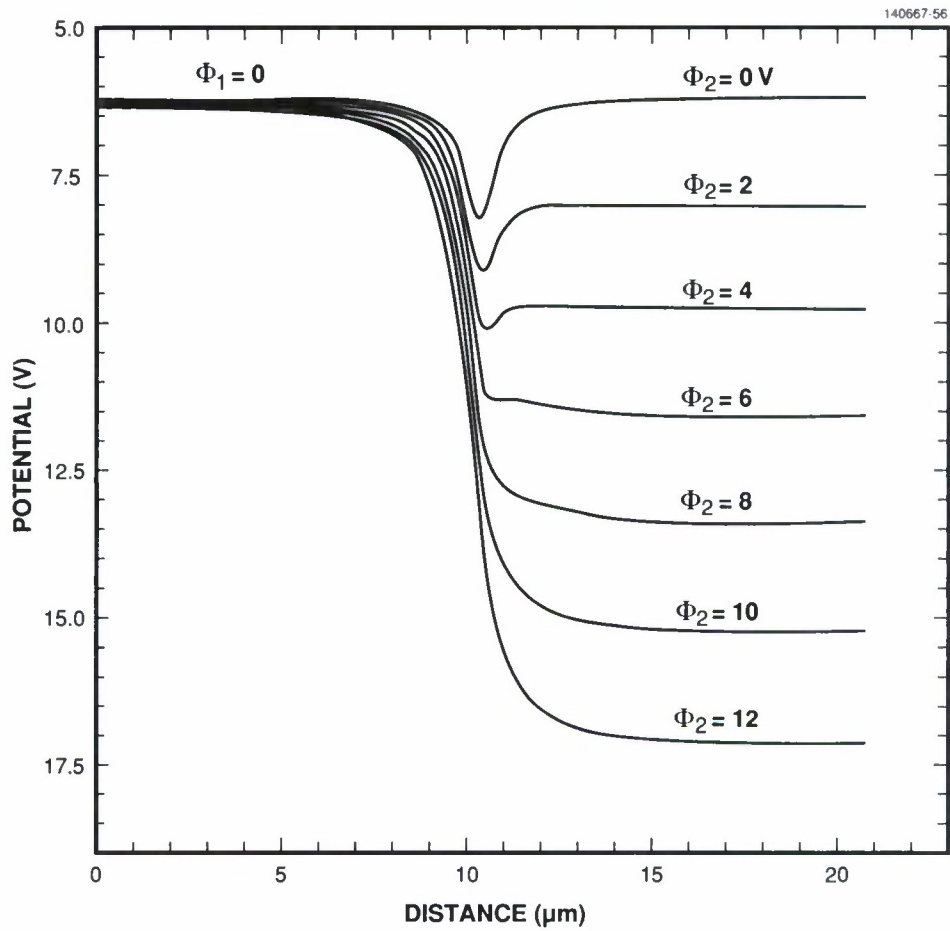


Figure 6-11. Calculated potential minimum (taken across depth) of empty wells as a function of lateral position for different gate voltages when the gap region has been implanted.



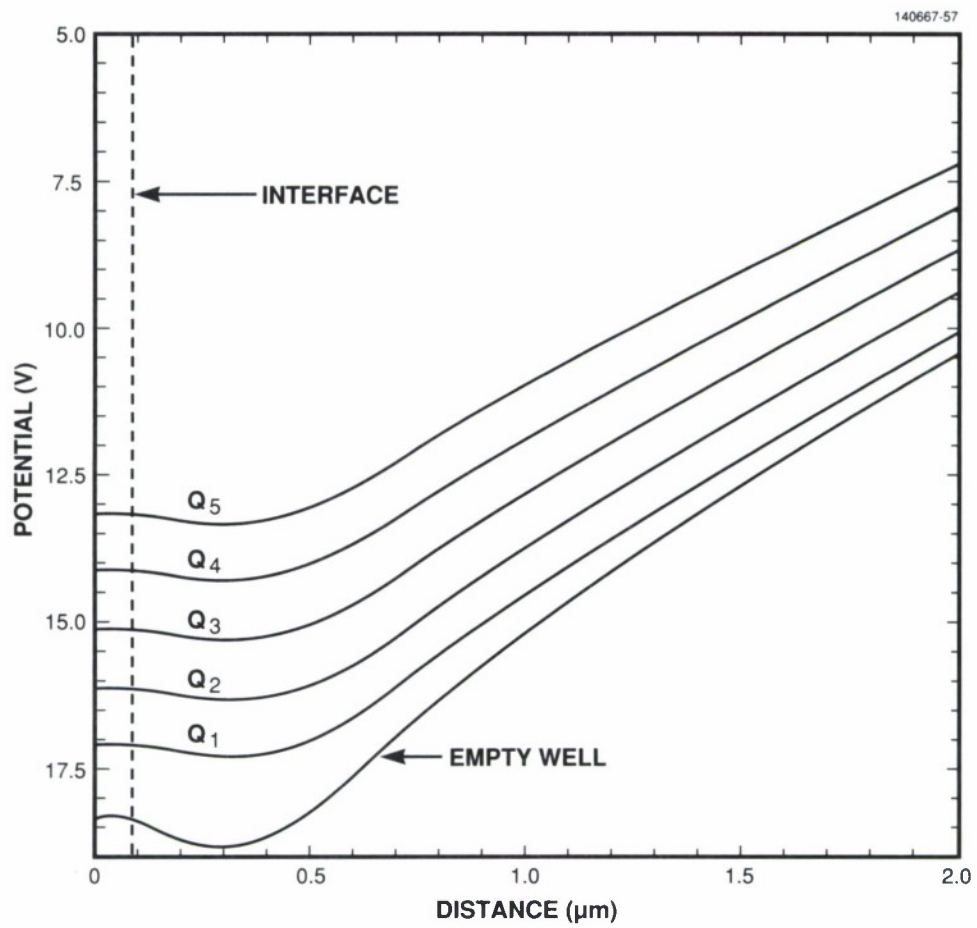


Figure 6-12. Calculated potential as a function of depth in a cross section in the counterdoped gap region for different charge packets.

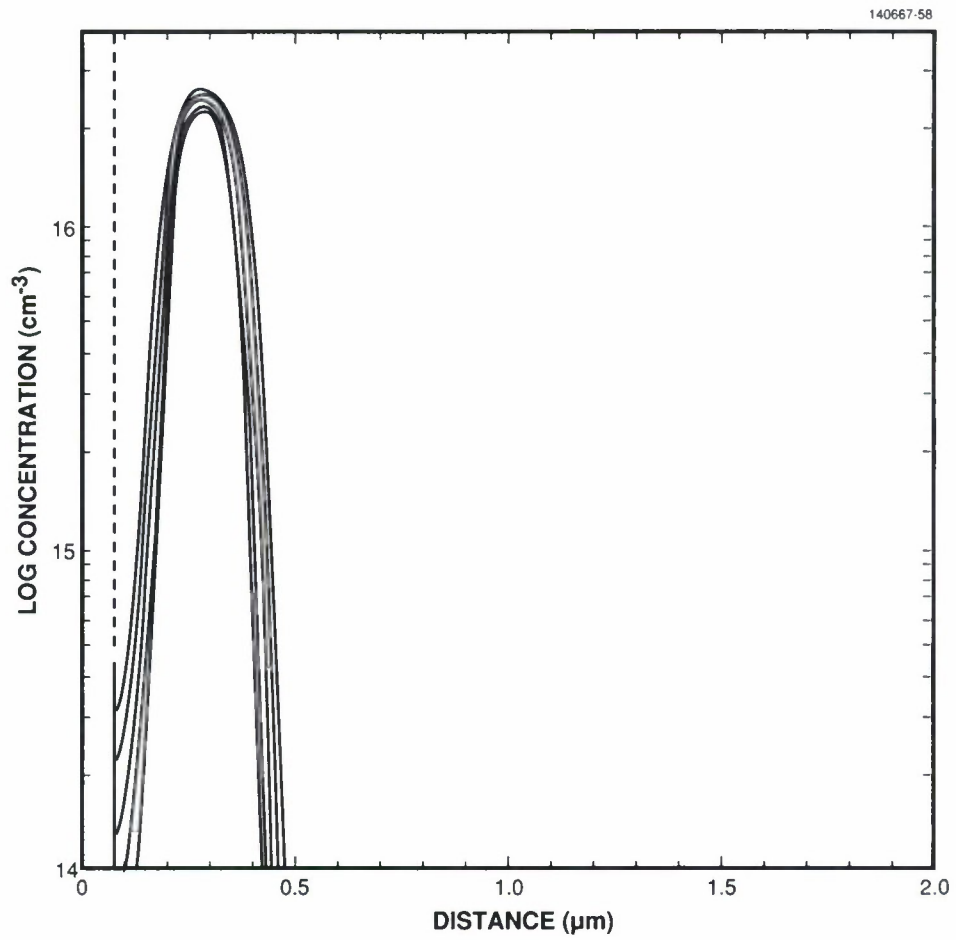


Figure 6-13. Spatial charge distribution corresponding to the curves in Figure 6-12.

## REFERENCES

1. J.B. Green, A.C. Anderson, and R.S. Withers, *Proc SPIE* **879**, 71 (1988).
2. H.K. Olsson, *IEEE Trans. Magn.* **25**, 1115 (1989).
3. C.K. Kim, *IEDM Tech. Dig.* (IEEE, New York, 1974).

